CHAPTER 7
TOMOGRAPHY DIAGNOSTICS: BOLOMETRY AND SOFT-X-RAY DETECTION

L. C. INGESSON* *EFDA Close Support Unit–Garching*
Boltzmannstr. 2, D-85748 Garching, Germany and FOM-Instituut voor Plasmafysica, Associatie Euratom-FOM
P.O. Box 1207, 3430 BE Nieuwegein, The Netherlands

B. ALPER *EURATOM-UKAEA Fusion Association*
Culham Science Centre, Abingdon, Oxon. OX14 3DB, United Kingdom

B. J. PETERSON *National Institute for Fusion Science, Toki-shi, Gifu-ken 509-5292, Japan*

J.-C. VALLET *Association Euratom-CEA sur la Fusion Contrôlée*
Centre d'Etudes de Cadarache, F-13108 Saint-Paul-lez-Durance Cedex, France

This chapter reviews multichannel broadband measurement of the soft-X-ray radiation and total radiation in magnetically confined fusion plasma experiments. Common detector types used (including bolometers), details of their application, and interpretation of their measurements are described. An introduction is given to the application of computed tomography methods in the mathematical reconstruction of emission profiles from multiple (approximately) line-integral measurements, taking into account the specific circumstances common in magnetically confined fusion plasma experiments. Although the emphasis is on two-dimensional tomography of poloidal cross sections, the applications of Abel inversion, three-dimensional tomography, vector tomography, and other specific methods are briefly discussed. Several examples of the application and the plasma parameters that can be derived are given.

KEYWORDS: *soft-X-ray detection, bolometer, tomography*

Note: Some figures in this paper are in color only in the electronic version.

Contents—Chapter 7

*E-mail: christian.ingesson@efda.org

I. INTRODUCTION

A plasma emits electromagnetic radiation from low energies up to an energy roughly equivalent to the temperature of the plasma—typically a few to several tens of keV—due to a variety of processes in the plasma of electrons and ions, and not-fully ionized atoms. In the visible to (soft) X-ray range, magnetically confined fusion (MFE) plasmas are generally optically thin. This means that the plasma is a volume emitter and a measurement along a certain view is an integral of the emissivity over the volume viewed. The characterization of plasmas from spectroscopically resolved measurements from single detectors is discussed in detail in Chapter 5, "Passive Spectroscopic Diagnostics for Magnetically Confined Fusion Plasmas," by B. C. Stratton et al., in this special issue of *Fusion Science and Technology*. Without having to resort to assumptions and modeling, the spatial distribution of the emission from the plasma can only be determined from measurements of multiple views of the plasma using mathematical techniques used in computed (or computerized) tomography similar to that used in medical computed tomography scans. This chapter deals with broadband multichannel measurements from the soft-X-ray (SXR) to infrared range and tomographic reconstruction of emission profiles, which

are useful tools for the analysis of various phenomena in MFE plasmas. The principles of these diagnostics, their implementation, and examples of results will be described.

Multichannel measurements, for example, in the X-ray and visible wavelength ranges, are an established diagnostic technique for MFE plasmas and other laboratory plasmas. If the plasma cross section that is probed by approximately line-integral measurements (i.e., narrow viewing cones for each channel) and the emissivity are circularly symmetric, a so-called Abel inversion can be used to mathematically reconstruct the local emissivity. Many plasma parameters are to first order constant on arbitrarily shaped magnetic flux surfaces in normal plasma conditions, and this symmetry can be incorporated in a straightforward way in mathematical inversion methods. These are often still referred to as "Abel inversions," although that is only strictly correct for circular symmetry. When such assumptions about symmetry are not possible, multichannel measurements from more than one angle are needed to be able to reconstruct the local emissivity by tomographic techniques.

In the visible range, Abel inversions have been applied to obtain line-radiation profiles[1] and to determine Z_{eff} (Refs. 2 and 3). Multidirection views made possible the tomographic reconstruction of the emission profiles with fewer assumptions.[4–7] Although there are many examples of visible-light tomography on MFE plasmas and interesting results have been obtained—the former references are pioneering examples—their use has not become as widespread as SXR and bolometer tomography, which are now in use on most major MFE experiments. More-difficult technical implementation and the limited amount of useful derived plasma parameters are probably the reason for the limited use of visible-light tomography. Visible-light tomography is outside the scope of this chapter and is discussed to some extent in Chapter 5. Spectrally resolved line-integral measurements in any wavelength range from the visible to X-rays requires special consideration in tomographic reconstruction if Doppler shift and Doppler broadening of spectral lines due to plasma rotation and temperature are appreciable, which will be briefly discussed in Sec. IV.I.4.

The first application of two-dimensional (2-D) tomography to SXR detection on MFE was with single cameras, i.e., a fan view from one direction, and made use of plasma rotation.[8–11] Full tomography with at least two cameras with a limited number of detectors was realized soon afterward.[12–14] Because of promising results in various areas, such as the analysis of sawteeth, magnetohydrodynamic (MHD) modes, and impurity transport, SXR diagnostic systems were extended to five or more independent views on many machines, for example on TdeV (Refs. 15 and 16), Alcator C-MOD (Ref. 17), RTP (Ref. 18), JET (Refs. 19 and 20), ASDEX Upgrade (Ref. 21), TCV (Refs. 22 and 23), and Wendelstein 7-AS (Ref. 24). At the present time, most major machines have

a multichannel, multiview SXR diagnostic, and such a diagnostic is also planned for new machines such as Wendelstein 7-X (Ref. 25), K-STAR (Ref. 26), and SST-1 (Ref. 27). A detailed account of the application of SXR arrays and X-ray crystal spectroscopic imaging systems for the diagnosis of MFE plasmas is given in Chapter 5 and will not be repeated here. The focus here is on detector types for broadband measurements, i.e., not spectroscopically resolved, and other relevant examples.

Wide-angle-viewing single bolometers were often applied on early MFE experiments to estimate the total radiated power,[28] which is an important quantity to understand the power balance in the plasma. The dependence of total radiated power on density and impurity injection has been studied in this way, as well as local effects due to, for example, a poloidal limiter. As will be described in Sec. III.C.2, a measurement from a single wide-angle bolometer is only adequate to estimate the total radiated power when the radial and poloidal emissivity distributions are known reasonably well. The high-Z impurities for machines with metal first walls and later divertors (TFR, PLT, ASDEX, DITE, etc.) could lead to localized peaks in the emission profiles, necessitating collimated bolometer measurements along several lines of sight. Originally, a single collimated bolometer was moved on a shot-to-shot basis, and Abel inversion could be used to deduce the radial emission profiles. Later, systems with multiple collimated channels were installed on many machines.[29–36] The characterization of the complicated features in the emission profile is particularly important for the understanding of divertor physics. More-extensive viewing systems are therefore needed[37] that make possible tomographic reconstructions of those features, such as implemented on, for example, ASDEX-Upgrade (Ref. 38), JET (Ref. 39), ALCATOR C-MOD (Ref. 40), DIII-D (Ref. 41), JT-60U (Ref. 42), and TCV (Ref. 43).

The tomographic reconstructions and Abel inversions are mathematical problems classified as so-called ill-posed problems. Well-developed mathematical techniques exist to deal with the ill-posedness. Over many years a large number of algorithms for computed tomography in MFE diagnostics have been developed, applied, and published. To the nonspecialist, it can be difficult to see clearly the basic assumptions in the various algorithms and how they are related. Furthermore, some of the published applications use the known mathematical techniques, some deal properly with the ill-posedness by physical intuition, and some solve the problem incorrectly and should therefore not be duplicated. Rather than giving a review of all algorithms applied, a practical introduction to the application of tomography in the field of MFE diagnostics is given that should enable the reader to understand where various algorithms fit in and to make a suitable choice for a particular application. Although the mathematics of actual implementations and many variations in algorithms are complex, the main concepts are simple, and robust tomographic inversion algorithms

can be very compact. Various important aspects to consider are highlighted, and references are given on numerical implementation.

Tomography techniques similar to those used for multichannel SXR and bolometer systems are also used for, for example, arrays of neutron or gamma detectors; see Chapter 9, "Fusion Product Diagnostics," by M. Sasao et al., in this special issue of *Fusion Science and Technology*. Related mathematical techniques are applied to interferometry, reflectometry, and for example the deconvolution of instrument functions.

The structure of this paper is as follows. Section II discusses some issues of plasma emissivity specific to the SXR and bolometer diagnostics and parameters that can be derived from measurement of the emissivity (a more comprehensive overview is given in Chapter 5). Various types of X-ray detectors and bolometer sensors and their use in tomography systems in MFE devices are described in Sec. III, while a comprehensive overview of the application of tomography methods is given in Sec. IV. Examples of applications of the diagnostics are given throughout this chapter to illustrate certain issues. These examples are summarized and placed into context in Sec. V. Although specific issues related to application of the diagnostics in burning plasma experiments (BPXs) are discussed in all sections where appropriate, Sec. VI summarizes the prospects for future development and applicability to BPXs and gives general conclusions. Generic considerations for BPX applications are covered in Chapter 12, "Generic Diagnostic Issues for a Burning Plasma Experiment," by G. Vayakis et al., in this special issue of *Fusion Science and Technology*, which provides the background against which the specific issues can be understood. The review in this chapter is not exhaustive but instead focuses on pioneering applications, the range of most-common approaches, and mainly recent examples of applications.

II. PLASMA EMISSIVITY FROM SXR TO INFRARED

II.A. Mechanisms of Plasma Emissivity

Electromagnetic radiation emitted by a plasma ranges from millimeter-waves to gamma radiation. The main contributors to the power loss by radiation are line radiation, in particular, in the vacuum ultraviolet range by impurities such as carbon and occasionally higher-Z metals, and bremsstrahlung. The maximum energies of these two types of radiation are related to the electron temperature of the plasma, which in MFE is typically of the order of several to tens of keV. Synchrotron radiation, or cyclotron radiation from electrons, has a negligible impact on the power loss in present machines. The radiated power of synchrotron radiation under reactor conditions, such as in ITER, is appreciable. However, because the plasma is optically thick to the radiation at

the fundamental frequency, this power is redistributed in the plasma. An appreciable fraction may be lost from the plasma edge and may have to be taken into account in the power balance by measurement or by modeling of the emission, reabsorption, and wall reflections of synchrotron radiation. The loss through harmonics at frequencies at which the plasma is less optically thick is estimated to be negligible, even under reactor conditions.[44]

To determine the total radiated power, in particular on present-day MFE devices, it is therefore sufficient to have bolometers with near 100% efficiency in the infrared range to a few or tens of keV, depending on the electron temperatures achieved in a given experiment. SXR detectors sample only a small part of the spectrum in the keV range.

Processes contributing to radiation can be classified by the state of the electron involved before and after the interaction. Line radiation is caused by a bound-bound transition in atoms and not-fully-ionized ions, in which electrons have been excited by collisional excitation, mainly by electron collisions. Radiation can also be emitted when an electron is accelerated in the field of a charged particle. This process is a free-free transition when the electron is free after the encounter (the resulting radiation is called bremsstrahlung) and is free-bound when the electron is captured (recombination radiation).

The modeling of line radiation and the recombination processes that are also of importance in a consistent analysis such as radiative recombination, dielectronic recombination, and charge-exchange (CX) recombination are described in some detail in Chapter 5. The dominant line radiation is by low-Z impurities such as carbon and oxygen. Hydrogen isotopes radiate appreciably from the visible wavelength range to shorter wavelength ranges. In clean plasmas, the contribution to the total radiated power from heavy impurities is small, although even in such cases the line-radiation contribution in the keV range can be very significant with respect to bremsstrahlung. In case of negligible particle transport, the radiated power density of a particular impurity is approximately proportional to the electron and impurity density and is a function of electron temperature.[44] Note however that plasma particle transport is not normally negligible. The typical timescales of the atomic processes involved in radiation are comparable with the transport timescales in relation to profile scale lengths, leading to a blurring of the emission profile dependence on local plasma parameters. Opacity may be a problem at high densities and low temperatures. Although opacity has been observed for hydrogen radiation in divertor plasma on present MFE experiments,[45,46] the implications for the interpretation of bolometer measurements are marginal. In a BPX, with a denser divertor plasma, it may be needed to take into account opacity effects in the interpretation of spatial bolometer measurements.

The free-free and free-bound transitions give rise to a continuum (in energy) of radiation, due to the free electron having a continuum of energy states. Together, radiation resulting from both transition types can be described consistently (see Chapter 5). When recombination can be neglected, the bremsstrahlung emissivity per unit volume per unit solid angle per unit frequency can be written as[47]

$$\varepsilon_\nu = 5.0 \times 10^{-54} \frac{n_e^2 Z_{eff} \bar{g}_{ff}}{\sqrt{T_e}} e^{-h\nu/T_e} \quad (\mathrm{W\ m^{-3}\ sr^{-1}\ Hz^{-1}}) \ ,$$

(1)

where

n_e = electron density $(\mathrm{m^{-3}})$

T_e = electron temperature (eV)

$h\nu$ = photon energy (eV)

Z_{eff} = effective charge of the plasma

$\bar{g}_{ff}$ = Maxwellian-averaged free-free Gaunt factor, which accounts for quantum-mechanical corrections to a classical treatment.

The total radiation, i.e., bremsstrahlung and recombination, can be expressed as Eq. (1) multiplied by an "X-ray enhancement factor." In the visible range the recombination is negligible. The Gaunt factor is typically ~1 in the SXR range, while it is 2 to 5 in the visible range.[2,3,48]

The plasma emissivity is usually expressed in W/m³ sr. Because the plasma radiation can generally be assumed to be isotropic, the emissivity is regularly multiplied by 4π sr. The integral over a viewing cone yields a measured power or intensity. This is often approximated by a line integral (see Sec. IV.D), and the resulting quantity is referred to as brightness, or irradiance, in W/m² or W/m² sr.

II.B. Plasma Parameters Obtained from SXR and Bolometer Measurements

Table I lists plasma parameters that are routinely diagnosed with multichannel bolometer and SXR systems. These are described briefly below, and some of the examples shown in this chapter demonstrate the use. The bolometer and SXR diagnostics have occasionally been used to derive further plasma parameters, some of which are mentioned in Sec. V.

From Eq. (1) it is clear the bremsstrahlung depends on n_e^2, T_e, and Z_{eff}. Spatial plasma perturbations that locally change T_e, or in particular n_e, such as sawteeth, MHD modes, snakes, cold and heat pulses, pellet tracks, and other phenomena, therefore cause a significant change in SXR emission. Examples of studies of these phenomena that depended on SXR tomography will be discussed in Sec. V.A. The SXR emissivity can be detected along lines of sight, and spatial information about the perturbations can be obtained by tomography if a sufficient number of lines of sight are available.

Because of the exponential dependence of bremsstrahlung emission on T_e, Eq. (1) makes it possible to

TABLE I

Parameter/Technique Matrix for Bolometers and Broadband SXR Plasma Diagnostics*

	Total Radiated Power	Localization of Total Radiation	Radiative Power Loading on the Wall	Fast Evolution and Fine Structure of Emission Profile	CX Neutral Loss	Impurity Localization	Impurity and Heat Transport	Plasma Position	Electron Temperature	MHD Modes and Events	Described in
Broadband SXR detector				●		●	●	◆	⊕	◆	Sec. III.A
Bolometer	●	●	●		⊕	◆	●				Sec. III.C
AXUVD		⊕	⊕		⊕	◆	◆			◆	Sec. III.B

*Only parameters routinely derived are given. Examples of the plasma parameters derived are given throughout the chapter and are summarized in Sec. V.

Note: ● = Primary technique is well suited to the measurement. ◆ = Backup technique, provides similar data to the primary but has some limitations. ⊕ = Supplementary technique, can provide data that can be used to improve or check aspects of the primary measurement but is not complete in itself.

estimate T_e the from spectrally resolved measurements. As described in detail in Chapter 5, a two-filter approach, i.e., two SXR detectors with different filters, has often been used to derive T_e in this way, also with spatial resolution. Recently, a 2-D T_e profile has been derived by tomography from two-filter measurements on MST (Ref. 49).

Heavy impurities will radiate significantly in the SXR range, through line radiation, recombination radiation, and the Z_{eff} dependence in the bremsstrahlung. SXR tomography is therefore suitable for localizing the radiation of heavy impurities and in case of impurity injection can also be used for particle transport analysis, given the dependence of the emission profile on particle transport parameters. Full collisional-radiative modeling is usually required for such analysis (see Sec. V.A for examples).

Bolometers are used to determine the total power radiated by the plasma integrated over the entire plasma volume, and the spatial localization of radiating features, such as in the divertor and MARFEs (a MARFE, sometimes said to stand for multifaceted asymmetric radiation from the edge, is a radiation instability that appears in tokamaks as a toroidally symmetric ring as the result of local cooling by radiation in circumstances where the cooling itself leads to increased radiation and hence further cooling[44]). The spatial localization of the radiating features makes possible detailed comparison with modeling codes, while at the same time a quantity such as the power radiated within the separatrix is an input parameter for some modeling codes. A 2-D emission profile of a poloidal cross section also makes it possible to calculate the heat load by electromagnetic radiation on the first wall. Charge-exchange neutral losses from the plasma can also be determined from bolometer measurements; see Sec. IV.I.5.

III. DETECTOR TECHNOLOGY

This section discusses in detail the principles of various types of detectors used for SXR and total-radiated power detection in tomography systems, in particular, surface barrier diodes (SBDs), photodiodes, Absolute X-ray UltraViolet Diodes (AXUVDs), and bolometers. In this section, their use is illustrated with a few examples of data interpretation without tomographic reconstruction. A detailed account of the application of SXR arrays for the diagnosis of MFE plasmas is covered in Chapter 5 and will not be repeated here. Two-dimensional SXR detectors, which are now in common use, are also discussed in Chapter 5.

III.A. Detectors for SXR

III.A.1. Detector Principles

Silicon diode solid-state detectors have been the first choice for SXR detector arrays for several years primarily because of their low cost and simplicity of operation.

Originally, SBDs were used. These evolved from nuclear physics applications as particle detectors. In an SBD, a thin gold layer is evaporated on an n-doped silicon crystal, a semiconductor diode. If a positive potential is applied to the gold layer, a leakage current will flow from the n-doped silicon, and a depleted region close to the gold layer is formed. The thickness of this region is dependent on the voltage applied. The energy that is lost in the depletion region by incoming X-rays results in the creation of electron-hole pairs. Although the forbidden band gap for silicon at room temperature is only 1.115 eV, the average energy for electron-hole creation is taken to be 3.62 eV (a slightly higher value of 3.66 ± 0.03 eV has also been proposed[50]). It is clear that some of the energy in breaking the covalent bonds must also be passed onto the lattice in the form of phonons. The electric field in the depletion region is sufficient to collect these liberated charge carriers and thus produce a signal. The observation that the electron-hole average energy is constant over a wide range of photon energy enhances the versatility and value of various types of semiconductors as radiation detectors.

Although SBDs are still used for SXR detection, p-n junction and PIN photodiodes are now more common. In a "P-I-N" photodiode a large, neutrally doped intrinsic (I) region is sandwiched between p-doped (P) and n-doped (N) semiconducting regions. The depletion region exists almost completely within the intrinsic region. One notable advantage of these photodiodes is in their flexibility for design and manufacture. Detectors can be constructed as single elements or in multiple-element arrays sharing a common cathode. Arrays consisting of 20 or 35 detectors on a single chip are typical. These detectors normally operate at room temperature. Although background noise doubles for every 10°C rise in detector temperature, noise levels at room temperature are usually low, so the performance gain in actively cooling the diodes further is not generally warranted.

Diodes are usually operated with a low reverse bias voltage up to ~15 V. They are operated in photoconductive or current mode where variations in detector current are measured. This gives far better time resolution than pulse mode in which single photons are counted but comes at the expense of loss of information on the photon energy spectrum. In current mode, diodes have a nominal efficiency in the SXR region of one electron-hole pair liberated for every ~3.6 eV of incident radiation (see discussion above). Response is linear, with currents ranging from a few nA to tens of μA. Bandwidths exceed 100 kHz. These diodes usually come with a SiO_2 passivating front surface and possibly a Si-N antireflective coating. These layers will absorb photons below ~300 eV. The effects of these coatings can usually be neglected in applications with beryllium filters of a few microns or more that are used as energy filters and often also as vacuum protection windows. Special AXUVDs have been developed for windowless applica-

tions where these absorbing surfaces have been kept to a minimum (see Sec. III.B).

SXR diodes have a typical thickness of silicon of 300 μm. The dependency with energy of their sensitivity to SXRs has received much study.[51,52] Based on experience with pulse-height systems that operate with bias voltages of ~200 V, it was originally thought that only the electrons released from the fully depleted region would contribute to signal current. However, full-depletion depths of <10 μm are formed for the low voltages applied to SXR arrays, yet SXRs with >10 keV are detected with reasonable efficiency. A model has been developed by Cho et al.[52] that has both the depletion region and the intrinsic (partially depleted) region contributing to the detector current. An effective diffusion length for electron-hole recombination is pictured for this partially depleted region that depends on semiconductor purity and lattice defects. This process enables the use of low voltages to be used for detection of thermal X-ray emission from MFE plasmas with reasonable efficiency and greatly simplifies the design of SXR diagnostic systems. SXR detectors have even been successfully operated with zero bias,[17] which simplifies further the design of the preamplifier electronics and minimizes detector noise. However, low-level radiation damage affects the diffusion process and reduces detection efficiency in the intrinsic region. This is found to be particularly noticeable when operated at zero bias. Increasing the reverse bias to only a few volts is found to significantly reduce the deterioration in performance from radiation damage,[53,54] so zero-bias operation is not generally used these days.

Unless the detectors are to be placed in the primary machine vacuum, an X-ray filter has to combine its role with that of a vacuum interface. Beryllium is particularly suitable, combining strength with good X-ray transmission, free from any absorption edges above a few hundred eV. Figures 1a and 1b illustrate how the diode sensitivity to the X-ray flux from bremsstrahlung varies with plasma electron temperature and with effective diffusion length for an SXR diode. A Be filter of thickness 250 μm, which has an X-ray threshold of ~2 keV, is also included. Figures 1a and 1b illustrate how flux in the energy range 3 to 8 keV dominates the diode current over a wide range of conditions. It also emphasizes how plasma emissions from metal K_α lines (e.g., Fe, Ni, Cr), which occur in this energy range, can dominate the SXR signal under some plasma conditions.

The actual functional sensitivity of plasma parameters to integrated SXR emission depends on the detailed nature of the plasmas being studied. For example, for so-called ELMy H-mode plasmas on JET, in which frequent edge-localized modes (ELMs) occur, the signals from SXR photodiode arrays were found to fit the form $n_e^{1.7} T_e^{1.6} P_p^{1.1}$, where P_p is a peaking factor.[55]

The choice of window and filter characteristics is discussed further in Chapter 5 and in particular the use of
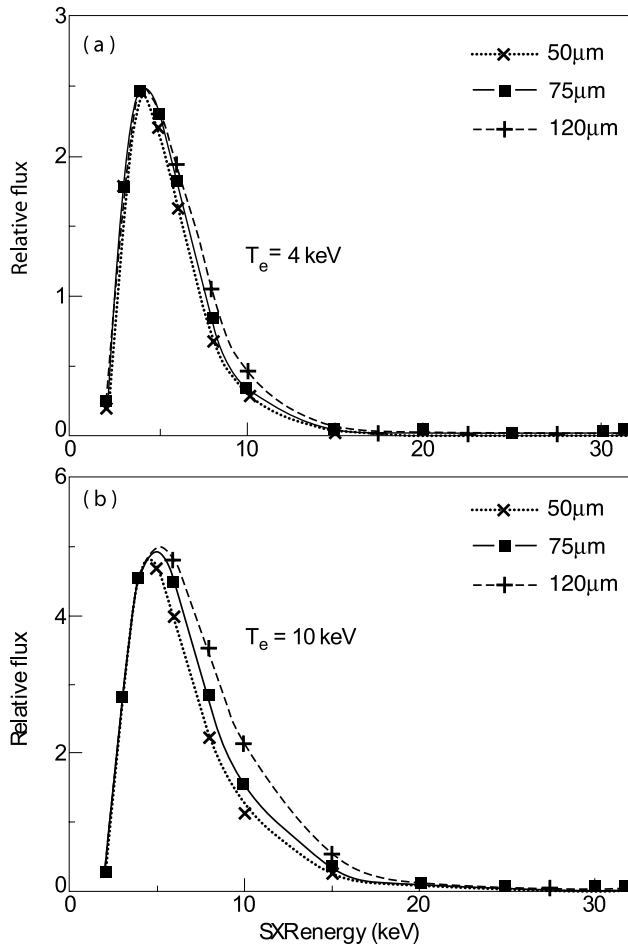
Fig. 1. The relative SXR flux contribution to the measured diode current from bremsstrahlung emission from a plasma with electron temperatures of (a) 4 keV and (b) 10 keV are plotted for various sensitive depths of silicon against photon energy. Account is taken of absorption in a 250-μm Be filter. The photon energy range 3 to 8 keV is seen to dominate the measured signal over a wide range of parameters.

multiple filters to select an energy pass-band window is of note.

Use of other nonsilicon-based SXR detectors has been considered to improve radiation hardness, for example, diamond or germanium. For applications in BPXs, line-of-sight detection of SXRs based on semiconductor technology is unlikely to ever be sufficiently radiation hard to operate during the D-T phase of ITER operation, although progress is being made in the development of reasonably radiation-hard semiconductor X-ray detector arrays (see Chapter 5) that may have an application for SXR tomography if they can be located in well-shielded locations. On large current MFE devices with deuterium plasmas, it may be needed to take into account a change in sensitivity as the result of neutron

damage,[56] and detectors have to be changed regularly. Other technologies that have been investigated include vacuum photodiode (VP) detectors.[57,58] The principle of VP detectors is based on the conversion of photon flux into electron flow as a result of differing efficiencies between anode and cathode photoconversion efficiencies. Good rejection of signals from gamma rays and neutrons is claimed. VP detector technology has yet to make a significant impact on SXR detection in MFE plasmas because of the relatively early stage of its technological development and the greater simplicity of silicon photodiode construction.

III.A.2. Electronics Issues

The electronics associated with SXR diode arrays often represent a major, if not dominant, component of the total system cost. The simultaneous requirements of low noise, high gain, high linearity, and high time resolution place strong demands on system design. Typical generic requirements are the following (see, for example, Ref. 59): (a) low-noise, screened twisted-pair cable to the front-end preamplifier, which should be located as closely as possible to the detectors; (b) high-gain, low-noise transimpedance amplifiers with gains in the range 10^4 to 10^8 V/A preferably with differential outputs for good common mode rejection; (c) compensation circuitry to offset drifts in electronics and dark current; (d) analog filtering using for example multipole Bessel filters to avoid aliasing with pass bands of $\sim$100 kHz; (e) avoidance of earth loops though channel-to-channel isolation if possible—isolated bias techniques using charged capacitors or in-line batteries have been successfully used; and (f) analog-to-digital conversion of typically 12-bits and 1-μs resolution.

In long-pulse machines the quantity of data to be stored and analyzed can become an issue. Event triggers, which record data at times of particular interest only, have been implemented on JET (Ref. 60). For ITER, real-time processing and data reduction will become essential. Real-time processing to obtain tomographic reconstructions from SXR data has been demonstrated to be possible.[61,62]

III.A.3. Examples of Applications of SXR Arrays

Useful results from plasma emission can in many cases be obtained with simple analysis techniques. Line-of-sight data from single diodes can provide valuable information on changes in sawtooth characteristics, for example. This is illustrated in Fig. 2 (Ref. 63), which shows the dependency of sawtooth characteristics on the relative amount of He^3 puffed into ion cyclotron range of frequencies–heated discharges on JET. The locations of peak SXR emission and sawtooth inversion radii can provide valuable supporting information on the position
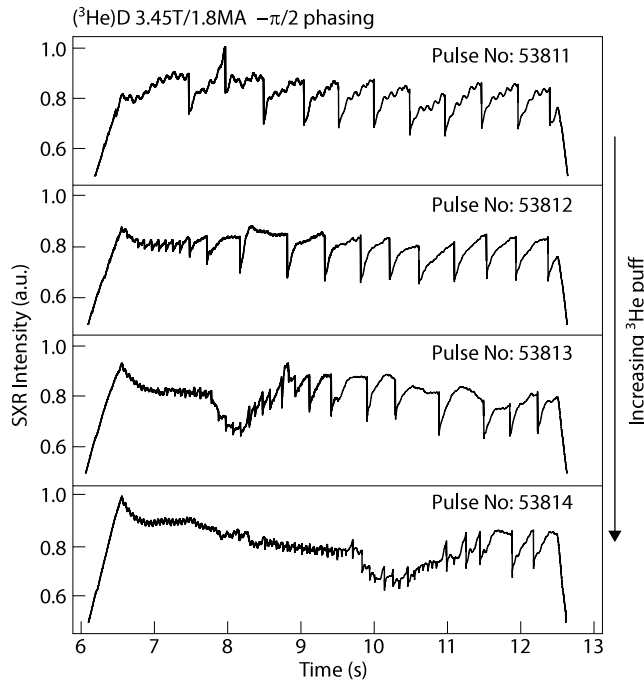
Fig. 2. Illustration of the usefulness of measuring SXR signals from a single diode. The change in nature of the sawtooth instability with increasing ^{3}He puff is seen in ion cyclotron resonance heating heated plasmas on JET (Ref. 63). (*Figure adapted from Ref. 63.*)

III.B. AXUVDs

Silicon p-n junction photodiodes are suitable not only for the SXR range. Special versions AXUVDs have been developed for a broad range of sensing applications in the vacuum ultraviolet, extreme ultraviolet, and the SXR spectral regions.[66] These diodes have an advantage of the absence of a surface dead region, which results in no recombination of photogenerated charge carriers and therefore 100% carrier collection efficiency and near theoretical quantum efficiency. As described in Sec. III.A.1, in addition, the diodes have an extremely thin (3 to 7 nm), radiation-hard, protective silicon dioxide window. These two properties result in a detector whose quantum efficiency can be predicted in most of the extreme ultraviolet region by the theoretical one electron-hole pair per 3.6 eV of incident radiation as mentioned above. However, the finite width of the silicon dioxide window results in oxide absorptions and reflections yielding quantum efficiency losses in the photon energy range of ~7 to 100 eV (Ref. 67). Because of the high quantum efficiency across a wide spectral range, AXUVDs can be regarded as bolometers provided the power emitted by the plasma in the spectral range where the quantum efficiency is reduced is negligible. In comparison with

of the magnetic axis and $q = 1$ surface. In some cases, the topology of MHD features can be simply extracted from SXR emission profiles, particularly when simple techniques such as average profile subtraction are used to enhance the SXR emission perturbation. An example of such an application is well illustrated in Fig. 3. This figure shows a snake on the $q = 2$ magnetic surface on JET. The snake clearly has a double helix topology pointing to an $(m, n) = (2,1)$ mode structure.[64]

Other techniques for applying data from SXR detector arrays have been developed. These include the application of cross-correlation techniques between a reference magnetic signal and data from the SXR detector array.[65] This can yield both the location of the MHD mode and phase change properties across the mode; it can for example distinguish island from kink structures. To a good approximation, the diode that is most sensitive to the perturbation from an MHD mode is the one where its line of sight intersects the tangent to the magnetic flux surface on which the mode is localized. Studies have also been carried out on JET to provide vertical control of plasma position based on real-time determination of the SXR emission centroid (see Sec. V.A). Chapter 5 discusses further applications of SXR data. The application of tomography and physics results that can be derived are discussed in Secs. IV and V of this chapter.

Fig. 3. A $q = 2$ snake is captured in the line-integral SXR emission profile plotted against time from a horizontally mounted 17-channel photodiode camera on JET (JET discharge #45922) (Ref. 64). The plasma height coordinate Z plotted for each channel is taken from the magnetic flux surface that is tangent to the line of sight of that diode. The time-averaged SXR signals have been subtracted to enhance the visibility of the $m = 2$, $n = 1$ double-helix perturbation.

standard resistive bolometers (Sec. III.C), these detectors are highly sensitive, have fast time response (approaching 1 μs), are very compact, are easy to use (requiring no calibration), and are inexpensive. In contrast to bolometers with a metal absorber, AXUVDs are also insensitive to low-energy particles, such as neutrals from CX reactions escaping the plasma.

These detectors have been applied to a wide range of measurements in MFE devices that can be classified as either bolometric (no filters attached) or filtered for various spectral regions ranging from vacuum ultraviolet to SXR. The first application to MFE research was on the LSX field-reversed-configuration experiment, which used two single-channel detectors whose signals were compared with a gold foil calorimeter.[68] Later measurements were made on the TEXT-U tokamak using a 16-channel array of AXUVDs that resulted in minor radial radiation profiles using a tomographic inversion. Also, a single-channel diode was compared with a platinum resistance bolometer having the same field of view.[69] On the Alcator C-Mod tokamak, radiation profiles from AXUVDs were compared with those from resistive bolometers to infer the neutral particle contribution to the bolometer signal (AXUVDs are insensitive to low-energy neutrals).[70] Many similar bolometric applications have been reported,[71–76] including 2-D tomographic reconstructions from multiple arrays.[77–80]

In addition to these bolometric applications, filtered AXUVDs have been used to measure various spectral lines to provide additional information about the plasma. In Alcator C-Mod, Lyman alpha filters were used on AXUVD arrays, and the data were used to infer the neutral density and ionization rate profiles.[81] This was extended to two dimensions on the TCV tokamak.[79] Measurements of profiles of impurity spectral lines in the vacuum ultraviolet region have also been undertaken using filtered AXUVD arrays.[72,76,82] Finally, thin metallic filters have been used with AXUVD arrays to provide SXR radiation profiles.[72,83,84]

While these detectors have been used successfully for various measurements as detailed above, when using them as a bolometer, care must be taken regarding the nonlinear region of quantum efficiency below 100 eV. That is why in most applications of this sort, the authors are careful to compare the results with those of resistive bolometers, and with spectroscopic measurements.[74] On JET, for example, it is typically found that deuterium radiates a nonnegligible fraction of the total power compared with carbon.[85]

Regarding BPXs, it is thought that because of the silicon substrate, these detectors will not be durable in a high neutron environment. Some tests of the effects of neutron radiation with fluences up to 10^{15} n/cm^2 on silicon detectors have been made showing changes in the calibration and diode performance.[54,86,87]

In order to reduce signal noise it is optimal to locate the preamplifiers in vacuum as close to the detectors as possible.[76] Also a two-dimensional array of photodiodes with a spectral response similar to the AXUVDs has been developed including in-vacuum preamplifiers and multiplexers to produce a 16×16 channel image with 1 μs time resolution.[88]

III.C. Bolometers

III.C.1. Introduction

Bolometers, from the Greek "$\beta o \lambda \varepsilon$," meaning line or arrow, and "$\mu \varepsilon \tau \rho o \nu$," meaning measure, also sometimes referred to as radiometers, are dedicated devices providing the measurement of the power flux transported by a radiated flux. Usually, the device combines an absorber and a thermometer. The thermometer monitors the temperature behavior of the absorber, which is designed to integrate the radiated flux in a given spectral domain. In most of the cases, the thermometers are either temperature-sensitive resistors or infrared detectors. When needed, to increase the detection limit or to subtract the background level (e.g., from nuclear heating), bolometers are coupled by pair, one of them being screened from the radiation flux. The arrangement in pairs also helps to set up a bridge configuration that is sensitive to small resistance changes (see below).

The first bolometer was constructed by Langley in 1878 for the purpose of measuring the averaged power density emitted by the sun and received on earth. This later led to the proposal by Bethe of thermonuclear fusion powering the sun, thus linking bolometers with thermonuclear fusion very early on. Langley's bolometer was composed of two blackened thin strips of platinum, having the same electrical resistance, assembled in a direct-current (dc) Wheatstone bridge. Various types of bolometers are extensively used in technological applications and modern physics, including for use in infrared imaging and laser light measurement.

Bolometers have been used in MFE experiments for energy balance analysis from the 1960s. Gorelnik et al.[28] used a "three-layer" germanium bolometer on the TM-2 tokamak, enabling the separation of the absorber and of the thermometer, thus allowing an independent optimization of the these two functions. In this case the absorber, a thin metal foil, is thermally linked to a germanium resistor, the thermometer, through a thin insulating layer, made of deposited magnesium oxide. Compared to platinum, germanium is a semiconductor, thus having a much higher electrical resistivity (up to 10^4 to 10^6) and a 12 times higher thermal resistance coefficient, allowing the design of very sensitive thermometers.

A decade later, efforts were made to make time-resolved measurements. Hsuan[89] developed a time-resolving bolometer for the ATC tokamak by connecting the absorber, a 25-μm-thick and 3-cm-diam nickel disk, to an annular copper heat sink. However, the large area of the absorber connected to the heat sink introduced two

problems. First, it leads to a large thermal capacity and thus a long cooling time (the time constant was 2 s, i.e., typically 50 times longer than the plasma pulse at the time). Second, the temperature decay and resulting gradients across the large surface depend on the combinations of several different cooling time constants.

In the 1980s, the large tokamaks, such as JET and TFTR, added the new constraint of radiation hardness on the bolometers. All the sensors using semiconductor resistors or alternative concepts that had previously competed with bolometers, such pyro-detectors and thermopiles, were found to be too sensitive to radiation damage. This led to a return to metal-resistor bolometers, which are now used on most MFE experiments. The resulting dramatic reduction of temperature sensitivity of metal resistors, compared with semiconductors, required optimization of the sensor geometry and the development of very efficient compensation and noise reduction techniques. Metal-resistor bolometers are described in Sec. III.C.4. Promising alternatives to the metal-resistor bolometers have been and are being developed: capacitive bolometers, in which the temperature of the absorber is measured by a change in capacitance instead of resistance, are described in Sec. III.C.5, and imaging bolometers, in which the temperature of the absorber is measured by an infrared camera, are discribed in Sec. III.C.6. Electronics issues for each of these are discussed together with the principles.

Before the principles of the bolometer types are discussed, it is relevant to consider the development of multichannel bolometer systems on MFE experiments from the single wide-angle measurements used at the beginning (Sec. III.C.2) and to summarize the effect of absorber characteristics on bolometer measurement, which is common for all bolometer types discussed (Sec. III.C.3).

III.C.2. Single Versus Multichannel Bolometer Measurements

In early MFE experiments,[28] single uncollimated bolometers were mounted on the first wall of the machine, thus measuring locally the energy flux falling on the wall. To be able to correctly infer the total radiated power from the measured power deposited on the wide-angle bolometer, the radial and poloidal emissivity distribution must be known reasonably well, and toroidal symmetry must be assumed; multiple toroidally distributed detectors are often used to verify this assumption. The derivation of the total radiated power can be significantly overestimated or underestimated if the spatial distribution of the radiation profile deviates significantly from the assumptions, such as in the case of a MARFE. Spatially resolved bolometer measurements have been used both to cross-check and complement spectroscopic evaluation of the radiation losses; an early example is, for instance, Ref. 90. For bolometers, spatial resolution has been obtained by the use of collimators and slit aper-

tures. Originally, measurements along several (approximate) lines of sight were obtained by moving a single collimated bolometer on a shot-to-shot basis, and later by the installation of multichannel systems. This is the norm on modern MFE experiments.

If the lines of sight are parallel, and cover an entire plasma cross section, the summing of the measurements multiplied by the distances between them gives a very good approximation of the total radiated power without any assumptions, provided toroidal symmetry can be assumed (this is usually the case, although for example gas injection may cause toroidal asymmetries). In practice, it is difficult to install truly parallel lines of sight covering the entire cross section, and one or more fans are normally used, which allows reasonable approximations.[91] Such a fan of lines of sight can also give a certain amount of information on the spatial distribution of the radiation, e.g., by Abel inversion if the emissivity is constant on flux surfaces. For more detailed information, especially to characterize the spatial profiles of the emissivity, elaborate systems with many channels (typically of the order 100) viewing at several angles are used, and tomographic reconstructions are used to derive the emission profiles.

III.C.3. Absorption Layer

The absorber of the bolometer determines its spectral response. For MFE plasmas, it would be preferable to have a 100% sensitivity to incident radiation from the infrared to the SXR range. Metals such as gold have been used for this; see Fig. 4 (Ref. 92). A layer of 4 μm gives a good response up to several keV, whereas for a BPX and in principle also JET a thickness of $\sim$10 μm is required. Gold cannot be used in a BPX because of its high-neutron-capture cross section and subsequent transmutation to mercury. Platinum has much the same optical properties (Fig. 4) and has a much lower neutron cross section. However, the deposition of the required thick layers required is not trivial. Other potential metals are explored in Ref. 93, with emphasis on the application for imaging bolometry in BPX.

At the long wavelength end of the spectrum, the sensitivity also decreases. Blackening has been used to increase the sensitivity in at least the visible range.[39,94] There is debate over the benefits and drawbacks of blackening. In some experiments it has been found that blackening also increases the sensitivity to the neutral background pressure, which is an unwanted effect. The reduced sensitivity in this part of the spectrum must be taken into account in the analysis. General experience indicates that the reduced sensitivity does not have a severe effect, as consistent power balances are usually obtained. The effect of the background neutral gas pressure, which may influence the calibration factors of bolometers during a plasma discharge, may also need to be considered.

The metal layer also absorbs part of the power of particles impinging on it.[95,96] Neutrals, produced in CX
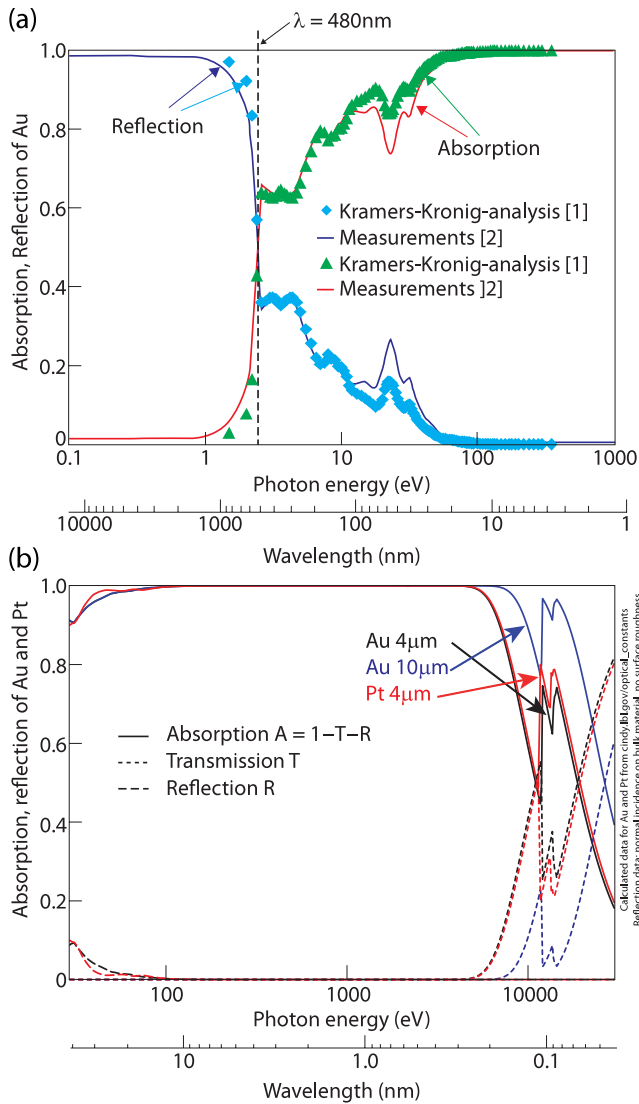
Fig. 4. (a) Absorption coefficient of gold in the spectral range relevant for bolometry on MFE plasmas and in (b) for comparison including platinum.[92] (*Figure reprinted with permission from Ref. 92; Copyright 2007, Elsevier.*)

reactions in the plasma (in particular, the cold edge and divertor), carry an appreciable energy (of the order of eV), which can give an appreciable bolometer signal additional to that of electromagnetic radiation. This is a drawback if the radiated power is required, but the measurement can also provide information on the total power loss (radiation and particles); this is discussed in more detail in Sec. IV.I.5.

III.C.4. Metal-Resistor Bolometers

The modern use of metal-resistor bolometers started on TFTR, where Schivell[94] used a concept very close to the original Langley differential bolometer, based on a combination of two almost free-standing 3.5-μm-thick 50-Ω platinum resistors, strengthened by means of a 7.5-μm-thick Kapton® foil.

For JET, Müller and Mast[97] proposed a concept of a three-layer bolometer developed for ASDEX. With a sensor size of 1.2 cm^2, it is still too large to fully cope with the problem of temperature distribution exposed by Hsuan. A blind reference bolometer, added at the rear side of the measuring bolometer, was used to compensate for thermal drift and and for nuclear heating. The detection was based on dc Wheatstone bridge fed with dc, allowing differential measurement.

For Tore Supra and ASDEX-Upgrade, Mast et al.[98] developed an improved miniaturized version of the JET bolometers (Fig 5a). The active area of the sensor was reduced to 6 mm^2, the time response of which became very close to an exponential shape. The time response is selectable by the thickness of a heat-resistive layer connecting the absorber to the thermal heat sink of the

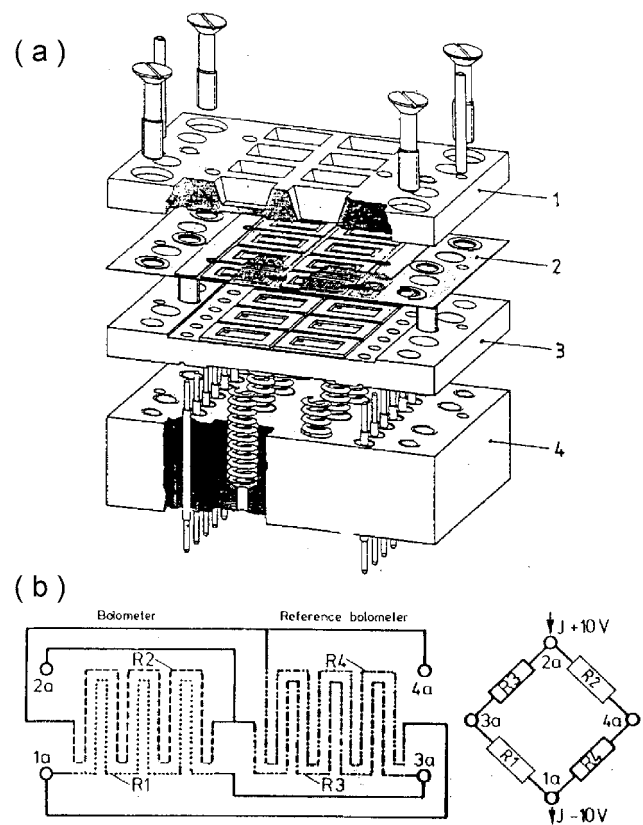Fig. 5. (a) Exploded view of a four-channel miniature bolometer[98]: 1, front cooling plate; 2, bolometer foil; 3, back cooling plate; 4, support plate and spring contacts. (b) Resistor meander layout behind signal and reference absorber foil to form a Wheatstone bridge; left: actual layout and right: schematic. (*Figures reprinted with permission from Ref. 98; Copyright 1991, American Institute of Physics.*)

bolometers and is typically chosen to be of the order of 0.2 s. The reference bolometer was built as a front bolometer on the same insulating substrate, a 7.5-μm-thick Kapton® foil, to further reduce the thermal drift and the pickup noise. For very fast measurements, the time constant of the thin insulating substrate may also need to be taken into account. Two resistors of 1.2 kΩ were deposited in a meander pattern (Fig. 5b) on the back of each absorber, and together with the resistors of the reference absorber (not seeing plasma light) were arranged as a Wheatstone bridge. The equation that very well approximates the response of the bolometer is[98]

$$P_{rad} = C\left(\frac{d\Delta T}{dt} + \frac{\Delta T}{\tau}\right) , \qquad (2)$$

where

P_{rad} = incident power

ΔT = measured temperature change proportional to the measured output voltage of the Wheatstone bridge

C = heat capacity

τ = time constant.

To obtain adequate detection and noise rejection, an alternating current (ac) electrical power is applied—typically at 50 kHz, which is far from the electromagnetic noise band of MFE experiments—and heterodyne detection is used. With such bolometers and heterodyne detection the noise-equivalent power during tokamak operation went down to the range of a few μW/cm^2. These bolometers are commonly produced in modules of four channels, each consisting of a measuring and a reference bolometer, and are available commercially. A typical measurement and the incident power derived from Eq. (2) are shown in Fig. 6. Because of the derivative in Eq. (2), when it is used to derive the power, it is important to be careful not to amplify noise in the measurement and to adequately process fast events, such as ELMs (Refs. 98 and 99). The bolometer signal is proportional to the absorbed radiative energy, and without using a derivative such as in Eq. (2), it has been possible to derive the total radiated energy and total energy radiation pattern over events much faster than the time response of the bolometer, such as ELMs and disruptions (see Sec. V.B).

The use of organic foils and of spring-based electrical contact as used in Ref. 98 restricts the application of this first version of the miniaturized bolometers below 150°C. In 1995, for JET in-vessel application, a high-temperature version was developed.[39] Mineral mica foils of 20-μm thickness substituted the organic substrate, and crimped connections were used instead of springs. To withstand the higher temperature, the gold resistor meanders had to be thicker (200 Ω), which unfortunately
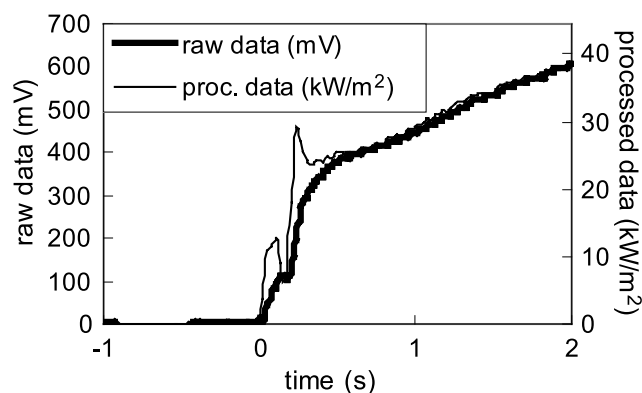

Fig. 6. Example of a bolometer measurement during the first 2 s in Tore Supra plasma pulse #37304: raw bolometer measurement (in volts output by the amplifier) and the derived line-integral power (in W/cm^2) using Eq. (2) and scaling by the étendue. On the timescale of the bolometer time constant (150 ms), the difference between raw and processed signals is apparent. The time resolution of the processed signals is ~30 ms.

reduced the sensitivity. The crimped connections have a high failure rate when the temperature is cycled, and alternative bonding techniques, such as ultrasound welding, are being tested.

In recent years, significant steps have been taken toward radiation-hard bolometer sensors. The JET type of high-temperature bolometer is seen as the reference for BPX (Ref. 100), although neutron irradiation tests of such a bolometer have shown several problems, including a weakening of the gold grids, possibly due to partial transmutation to mercury.[101,102] With the mica bolometer as the starting point, radiation-hard substrates, such as ceramics, of appropriate thickness as well as appropriate deposition techniques for platinum are being developed. The choice of substrate and its thickness is also an opportunity to optimize the sensitivity and time response of the bolometer. A prototype silicon-nitride substrate (4 μm) with platinum absorber and resistors has been demonstrated to have improved sensitivity with respect to mica bolometers[103] and is expected to be sufficiently radiation hard for application in ITER.

Dedicated electronics, with a lock-in amplifier for the heterodyne detection, have been developed.[98] The wiring and earthing concept implemented in the system is important for the performance of the system, in particular, dealing with four wires for each bolometer channel. The scheme chosen (or imposed by the policy on the experiment) determines whether each channel requires individual isolation, or common power supplies can be used. Typically two twisted-pair cables are used, one pair for the input voltage and one pair for the output voltage, which are sometimes combined into a quad cable. If possible, it is relevant to use special low-noise cables, for

example, with a PTFE or PEEK antimicrophonicity coating; the use of such low-noise cables is however limited by their maximum operating temperature. It is important that the driving ac power be synchronized for all nearby channels, as otherwise interference between neighboring channels can occur. Ideally, the resistors of the Wheatstone bridge should be perfectly balanced. Despite careful manufacturing, resistors in one bridge typically vary by a few percent (variation is a rejection criterion), which leads to an imbalance of the bridge and an offset voltage, which in its turn affects the performance of the system, such as the achievable amplification of the signals. Changes over time in the resistors and their contacts due to the environment to which they are exposed also affect the imbalance. The electronics therefore must be capable of balancing the bridge. Developments in electronics and processing have been reported in Refs. 35, 104, 105, and 106. The need for four wires for each bolometer channel, and the failure of one wire resulting in failure of the channel, is a significant concern for present-day experiments with of the order of 100 bolometer channels.

Because of the changes that can take place over time in the bolometers (as described above), it is important to regularly calibrate the bolometers. The bolometers can conveniently be calibrated in situ by means of a change in the driving voltage, which changes the self-heating of the resistors: This allows the derivation of the sensitivity and time constant.[98,106] Hardware for calibration can be integrated with the electronics.

Drift of the signal can occur during a plasma discharge, for example, due to an imbalanced bridge, gas pressure, or other reasons for changing calibration factors, which makes interpretation of the measurement difficult as the reference level at the beginning of the discharge is lost. Attempts are being made to improve the balance of the bridge, which is particularly important for measuring long plasma pulses with high sensitivity. This can be done either during manufacture, for example, by special provisions of the resistors that allow them to be changed (e.g., by laser trimming) or during operation by changing the temperature, and hence resistance value. The latter has been achieved by implementing an additional resistor behind both the reference and signal absorber, which makes it possible to balance the bridge by resistively heating the signal or reference bolometer in a feedback loop on the bridge imbalance. This can be taken one step further, by also introducing a feedback on the measured temperature, i.e., heating the signal branch of the Wheatstone bridge to keep the output voltage constant, in which case the feedback signal is directly proportional to the incident radiative power.[94,107,108] This has the potential of yielding a much more sensitive and faster measurement of the incident power than possible with the derivation from Eq. (2). Although these techniques have partly been demonstrated, they are not yet in routine use. Significant disadvantages of the active techniques are the more-complex electronics needed for each

channel, and the additional wires needed to the extra resistors, bringing the total to eight wires per bolometer channel.

III.C.5. Capacitive Bolometers

Capacitive bolometers have been proposed because of the potentially high sensitivity and possible operation with fewer wires.[100,109,110] The principle is based on a thin-film ferroelectric capacitor, which exhibits large capacitance changes as a function of temperature. The capacitor can either be put in a capacitive bridge in a similar way as the resistive bolometers (thus not giving any reduction in wires), or in an *LC* resonance circuit, thus making it possible to measure a number of channels, with different resonance frequencies, with just two wires. The ferroelectric materials, in particular, $PbZrO_3$, may be sufficiently radiation hard for a BPX environment.[111,112] Despite the promise of capacitive bolometers and significant development efforts, technical problems, such as unexpected difficulties in etching a structure adequate for a bolometer behind the ferroelectric film and problems in making adequate electrical contacts, have so far plagued the actual demonstration of a functioning capacitive bolometer.

III.C.6. Imaging Bolometers

Like the metal-resistor bolometers described above, imaging bolometers are conceptually based on a radiation-absorbing thin metal foil. However, in this case the resulting change in temperature is measured by an infrared camera placed outside the vacuum vessel.[113–115] The first time infrared measurements were used to monitor the temperature of a (preheated) tantalum foil used as absorber was on TFR (Ref. 116). Two types of metal foil imaging bolometers have been proposed. Initially, individual detector channels were defined and thermally isolated from each other by sandwiching the thin foil between two masks having identical 2-D hole patterns.[113] Later, a concept known as the infrared imaging video bolometer (IRVB), which exposes one large thin foil in a frame, was introduced.[114,115] The advantage of the prior concept would be increased durability due to the foil support by the mask, while the later concept is more sensitive due to the improved utilization of the infrared camera pixels and reduction of edge cooling of the foil and provides more flexibility in making trade-offs between sensitivity and the number of channels.

In order to determine the radiated power density S_{rad} at each IRVB channel, the 2-D heat diffusion equation for the foil[115]

$$\frac{\partial^2 T}{\partial x^2} + \frac{\partial^2 T}{\partial y^2} = \frac{1}{\kappa}\frac{\partial T}{\partial t} - \frac{S_{rad}}{kt_f} + \frac{\varepsilon\sigma_{S\text{-}B}(T^4 - T_0^4)}{kt_f} \quad (3)$$

must be solved from the infrared camera measurements of the foil temperature T, taking into account the

Stefan-Boltzmann constant σ_{S-B} and the thermal properties of the foil: thermal conductivity k, and thermal diffusivity κ, the thickness t_f, and the blackbody emissivity of the foil ε, which is maximized by blackening with graphite. While ideal numbers for the last four quantities are known, the actual values should be determined through a foil calibration process.[115,117] The heat diffusion equation Eq. (3) can be solved using a Crank-Nicholson numerical technique, and the noise level is reduced at the expense of fewer bolometer channels by averaging over multiple (N) infrared camera channels for each bolometer pixel.[115] In Fig. 7 images from various steps in the analysis process are shown.[118] The noise equivalent power η_{IRVB} for the IRVB is given as[115]

$$
\eta_{\text{IRVB}} = \frac{\sqrt{10}kt_f\sigma_{IR}}{\sqrt{mN}}\sqrt{1 + \frac{l^4 f_{IR}^2}{5\kappa^2 m^2} + \frac{4l^4\varepsilon^2\sigma_{S-B}^2 T^6}{5k^2 t_f^2}} \quad ,
$$

(4)

where

l = linear dimension of the bolometer pixel

m = number of time frames averaged over

σ_{IR} = infrared camera sensitivity

f_{IR} = frame rate of the infrared camera.

From Eq. (4) it can be seen that the sensitivity can be increased (η_{IRVB} decreased) by averaging over frames,

averaging over more infrared camera pixels, and improving the infrared camera sensitivity. This indicates that the bolometer sensitivity will improve with continued advances in infrared camera technology. Sensitivity can also be improved by proper choice of the foil material[93] and by making the foil thinner; however, the latter is done at the expense of a decreasing ability to stop high-energy photons and absorb their power.

Infrared cameras typically acquire data with 14 bits of dynamic range. The time resolution is ultimately limited by the readout time of the array and the number of pixels. For a 256×320 pixel InSb array, frame rates of up to 420 frames/s are available. The time resolution is also limited by the IRVB diffusive time constant or l^2/κ as can be seen from Eq. (4).

Imaging bolometers have been applied to three different devices. Imaging bolometers using a segmented mask were tested on the Compact Helical System[119] and the Large Helical Device[120] (LHD). IRVBs have been installed on LHD (Ref. 121) and JT-60U (Refs. 93 and 122) and used in studies of the three-dimensional (3-D) structure of radiative phenomena.[120–126] Figure 8 shows the radiation images from two imaging bolometers—one with a top view and one with a tangential view—during the steady-state (radially hollow and toroidally and poloidally asymmetric) and radiative collapse (poloidally asymmetric) stages of a discharge in LHD as compared with radiation models. The comparison of the image data with the models suggests that the poloidal asymmetry at the collapse is toroidally symmetric.[123]
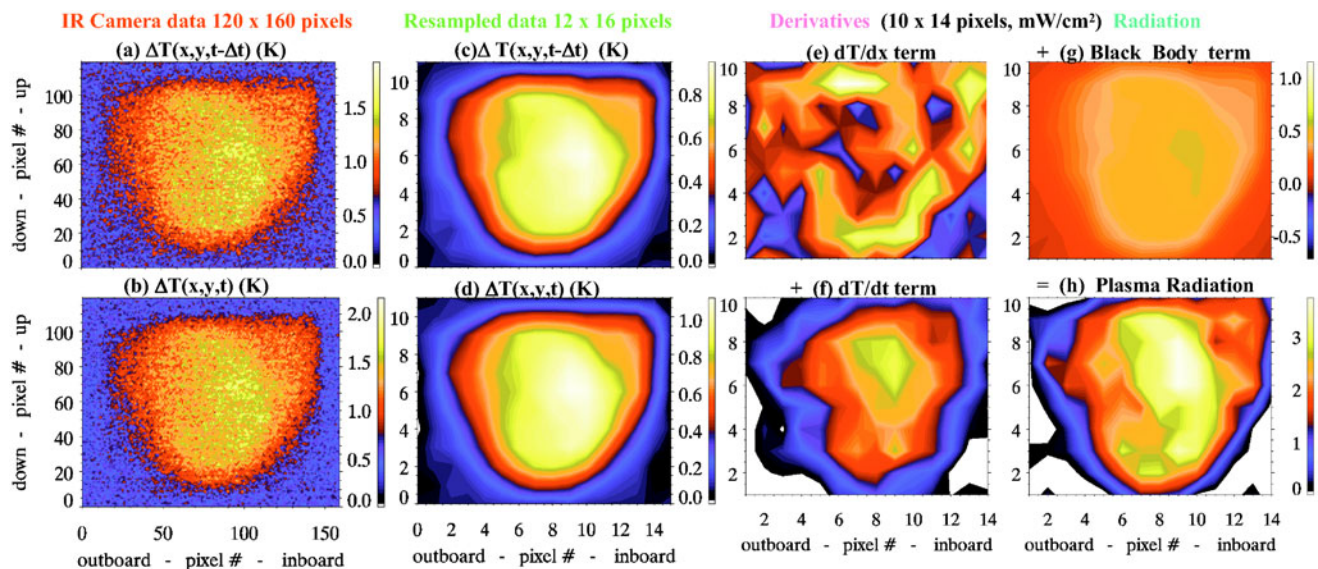
Fig. 7. Sequence of images showing data analysis technique of the IRVB for data taken from LHD during an experiment using the inboard wall as a toroidally periodic limiter.[118] (a) and (b) Two consecutive infrared camera temperature images. (c) and (d) Images (a) and (b) after resampling. The contributions to (h) radiated power density calculation S_{radp} in Eq. (3) are (e) spatial derivative term, (f) time derivative term, and (g) blackbody radiation term. (*Figure reprinted with permission from Ref. 118.*)
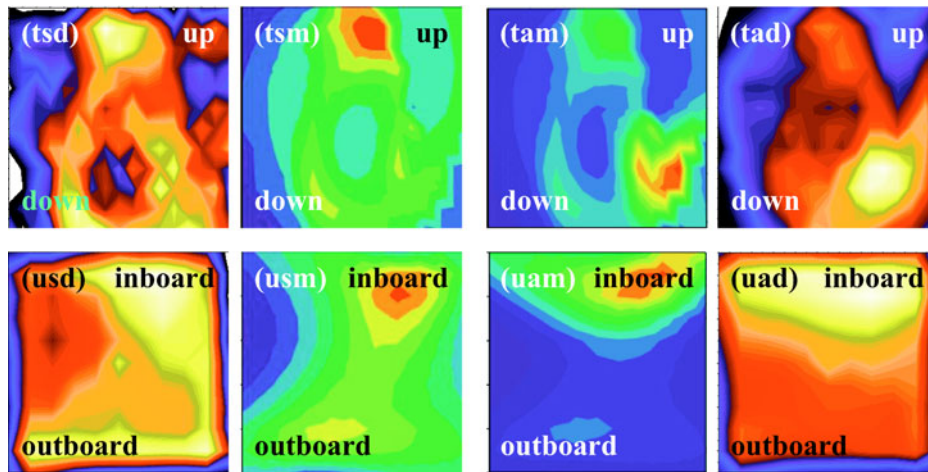
Fig. 8. IRVB radiation brightness image (d) data from (u) upper and (t) tangential ports in LHD during the (s) steady state and (a) asymmetric phases of the discharge compared with reconstructions from (m) model profiles.[123] (*Figure reprinted with permission from Ref. 123; Copyright 2006, The Japanese Society for Plasma Science and Nuclear Fusion Research.*)

The imaging bolometer is well suited to the nuclear environment of a BPX since it uses only metallic components and has no electrical contacts or feedthroughs. The durability of a thin metal foil exposed to disruptions has been partly demonstrated by the IRVB on JT-60U (Ref. 123), but further tests should be made at the acceleration levels expected in ITER. Another concern regarding the large free-standing foil of the IRVB might be its stability in the presence of gas puffing and forces induced in the foil resulting from induced currents and the magnetic field, and durability during large vacuum vessel pressure excursions, for example, during massive gas injection as a disruption-mitigation scheme. The current IRVB design incorporates blind vents in the foil frame and in the infrared radiation transmission tube, to maintain equal pressure on both sides of the foil and avoid its destruction during such an event. IRVBs with such vents using relatively thin (1 to 2.5 μm) and weak (gold) foils have not had any problems during standard pumpdown and venting events, and also during catastrophic vacuum accidents. Therefore, problems are not expected on a reactor using a thicker (10 μm or more) foil and stronger foil material (for example, tantalum), although their survivability under the extreme conditions that may occur in a BPX should be further tested. A concern in the nuclear environment is the accuracy of the infrared measurement through a mirror labyrinth system, in which efforts must be made to be able to adequately control or compensate for the mirror temperature. In addition to the intrinsic radiation hardness, the primary advantages of the IRVB compared to the standard resistive bolometer are the imaging capabilities. This may be useful in a reactor for real-time monitoring of the radiation from the plasma, but it also presents a disadvantage in that all of the detecting channels are concentrated behind one pinhole whereas for tomography purposes the optimal arrangement would be a poloidal distribution of detectors around the plasma as is possible with resistive bolometers. It would be difficult to implement imaging bolometers in such a poloidal distribution because of the necessity of an optical path from the foil to the infrared camera. This disadvantage can be somewhat reduced by implementing the imaging bolometer with a tangential view, which provides a greater angular distribution of sight lines through the plasma than a radial view, as long as toroidal symmetry can be assumed.[93] Tomographic reconstruction of a semitangentially viewing imaging bolometer has recently been demonstrated.[126] In terms of sensitivity, it is expected that imaging bolometers may surpass resistive bolometers as infrared technology increases.[93]

IV. TOMOGRAPHY

IV.A. Introduction

Methods for computed tomography are used in many fields, in particular, in medicine (X-ray absorption, positron emission, single-photon emission, and in some cases in magnetic resonance imaging), but also in many other areas such as nondestructive materials testing, geophysics, and atmospheric research. The common characteristic is that many nonlocal measurements, such as line integrals, are processed mathematically to estimate local physical quantities, such as emissivity or absorption. The integral equation is a so-called Fredholm integral equation of the first kind. Inversion of such an integral equation is often classified as an ill-posed problem,[127,128] for which there is no unique solution because of the

finite sampling, and a differential operator in the inverse amplifies noise present in the input data. Well-established mathematical methods have been developed to be able to invert this type of integral equation, which is achieved by regularization. Similar mathematical techniques for inversion, e.g., deconvolution, are used in remote sensing, astrophysics, and image processing.

Much of the basic theory on regularization of ill-posed problems and tomography is also valid for application in MFE diagnostics. There are, however, some general characteristics of MFE diagnostics that distinguish the field from other applications of tomography and affect which mathematical methods can be applied: (a) limited number of lines of sight and viewing directions, (b) irregular spatial sampling, (c) finite viewing beam widths, and (d) noisy measurements. The first two characteristics are mainly because of the difficult access to the plasma through the vacuum vessel and the fact that temporally resolved measurements are required. For temporally resolved measurements, typically on the millisecond or microsecond timescale, with adequate spatial resolution, many (hundreds) of separate detectors and electronics channels are required, and cost often limits the number. This is in contrast to various other tomography applications, such as medical tomography, in which no or very low time resolution is required and the detectors can be moved to measure at various angles. The other characteristics are related to compromises between temporal resolution, spatial resolution, and signal-to-noise ratio. An additional complexity, in particular, in bolometer tomography of divertor plasmas, is that the local emissivities can locally vary over more than an order of magnitude.

This section gives a short overview of the mathematical background of tomography in as far as is relevant for MFE diagnostics given the characteristics mentioned above and discusses methods to cope with them. Although there is some mathematical complexity, especially for obtaining a deeper insight into the problem, most tomography methods are very straightforward to implement. This section focuses on emission tomography of optically thin plasmas with negligible refraction. The emphasis is on bolometer and SXR tomography, but the description is also valid for other applications, such as visible, neutron, or gamma-ray tomography (with appropriate allowance for effects disregarded here, such as scattered neutrons). Mathematically, inversion of interferometer and reflectometer data is very similar (see Chapter 3, "Microwave Diagnostics," by N. C. Luhmann, Jr., et al., and Chapter 4, "Laser-Aided Plasma Diagnostics," by A. J. H. Donné, C. J. Barth, and H. Weisen, in this special issue of *Fusion Science and Technology*). If the plasma is optically thick, the mathematical description of the problem changes from the very first equation, and this is outside the scope of this chapter. Mathematical techniques to deal with optical thickness exist from other tomography applications than plasma physics, in princi-

ple similar to those described below with an additional term; see, for example, Ref. 129.

After a brief historical overview of tomography in MFE diagnostics (Sec. IV.B), first some mathematical concepts will be introduced (Sec. IV.C). The level of mathematical detail is limited and sufficient to provide the main insights in the tomography problem; appropriate references are given for more details. The discussion in Sec. IV.D of line-of-sight coverage, spatial sampling, optimization of lines of sight, and how finite beam widths can be taken into account in this context is particularly important for MFE applications, as these principles guide the design of the line-of-sight distribution. There are two basic approaches in tomography algorithms: discretization after mathematical inversion, which is discussed to some extent in Sec. IV.C, or numerical inversion after discretization. The latter is most appropriate for MFE application. Issues related to the discretization are reviewed in Sec. IV.E, while a practical approach to the key topic of regularized solution of the ill-posed problem is presented in Sec. IV.F. These key ingredients are placed into context in Sec. IV.G, which provides a practical guide on how the most widely applied tomography methods in MFE diagnostics can be implemented numerically. For the physicist it is important to understand what information can objectively be obtained from tomographic reconstructions (Sec. IV.H). This section concludes with a discussion of miscellaneous topics, such as Abel inversion, vector tomography, tangential and 3-D tomography, and special considerations for bolometer tomography (Sec. IV.I), and a summary of the main aspects relevant to plasma diagnostics (Sec. IV.J).

A number of classic textbooks exist on computed tomography, for example, ranging from mathematically oriented to practical application: Natterer,[130] Helgason,[131] Deans,[132] Herman,[133] and Kak and Slaney.[134] Although these books are mainly oriented toward medical tomography, a solid understanding of the tomography problem can be obtained. There are also a number of very useful review papers that can be recommended: Bertero et al.,[135,136] Lewitt,[137] and Hansen.[138] It is also interesting to note that in contrast with computed tomography, in some applications, e.g., in optics, it is possible to apply analog tomography.[139]

A note on terminology may be appropriate. Below, the terms "reconstruction," "inversion," and "solution" are largely used as synonyms. In the tomography field, a phantom is a mathematical or numerical model of the object to be measured (such as a plasma emission profile), which is often used for testing and understanding the capabilities of tomography algorithms by "phantom simulations." Artifacts are nonphysical and unwanted structures that appear in the reconstructions as the result of implementation errors, limitations of the tomography algorithm, numerical noise, errors in the interpretation of measurements, or noise in the measurements (in case of insufficient regularization).

IV.B. Overview of Application of Tomography Algorithms to MFE Diagnostics

The Cormack method[14,140–142] is one of the first to be applied to SXR tomography in MFE experiments. The maximum entropy method[5,143,144] was also investigated at an early time. Other classic methods from the wider tomography field include the algebraic reconstruction technique[133,145–147] (ART), and Phillips-Tikhonov regularization.[147,148] A special case of Phillips-Tikhonov regularization, which will be referred to as "constrained optimization" in this chapter, has found wide application,[23,38,42,56,149–151] after having been proposed for MFE diagnostics as early as 1982 (Ref. 152). These have found applicability to SXR, bolometer, and other tomography diagnostics in MFE. Basis functions with varying shapes have been used, such as matching the flux-surface geometry[35,151] and functional forms on the flux surfaces,[10,149] but the norm is to use a square regular grid. Computation time was a major obstacle in early applications. Advances in computing power have improved the prospects of methods such as maximum entropy and constrained optimization. Of the classic tomography methods, only filtered backprojection (FBP) has hardly been used at all in MFE applications.[153] The similarities and differences between these various tomography methods will become clear from the discussion in this section. In addition, purpose-made tomography methods have been developed that do not have an equivalent outside MFE, for example, using parameterization and geometries suitable for the expected emission profiles.[10] In particular, methods have been developed to extract information about MHD modes.[154,155] Such specific methods are outside the scope of this chapter. Variants of what here is called the constrained optimization method are the presently most widely applied tomography method, the practical implementation of which is described in Sec. IV.G, and the considerations leading to the choice between variants summarized in Sec. IV.J.

It is worthwhile to point out that in inertial confinement fusion[156,157] and low-temperature plasma physics,[158–160] tomography has also been applied for a long time but that the characteristics often are quite different from those in MFE diagnostics and that therefore other tomography methods may be preferred. It may also be possible to use neural networks to achieve tomographic reconstructions from a limited number of measurements (as is usually the case in MFE applications),[161,162] but this is not addressed further in this chapter.

IV.C. The Radon Transform and Some of Its Properties

For a 2-D emission profile $g(x, y)$, the i'th nonlocal measurement f_i can be described by

$$f_i = \iint K_i(x, y) g(x, y) \, dx \, dy \; , \tag{5}$$

where $K_i(x, y)$ describes the geometry. Tomographic reconstruction is the solving of $g(x, y)$ from Eq. (5), given many known measurements f_i. A straight line of sight can be parameterized by the (signed) distance p to a chosen origin (x_0, y_0) and an angle ξ with the x-axis (see Fig. 9a), in which case $K_i(x, y) = \delta(p_i + (x - x_0)\sin\xi_i - (y - y_0)\sin\xi_i)$. In this case, Eq. (5) is called the 2-D Radon transform. In 1917 Radon[163] derived an inversion formula; subsequently, many more-accessible derivations of this formula have been found, and all tomography textbooks give a derivation; see, for example, Ref. 133. The direct numerical implementation of the Radon inversion formula is of limited applicability, however, because it contains both a singularity and a derivative. Many interesting relationships exist between the Radon and Fourier transforms.[132] Numerous tomographic inversion methods exploit these relationships,[137] but most are mainly of academic interest as practical implementation problems limit their applicability. The relationship between the Fourier and Radon transforms allows one to demonstrate in a straightforward way[132,137] that
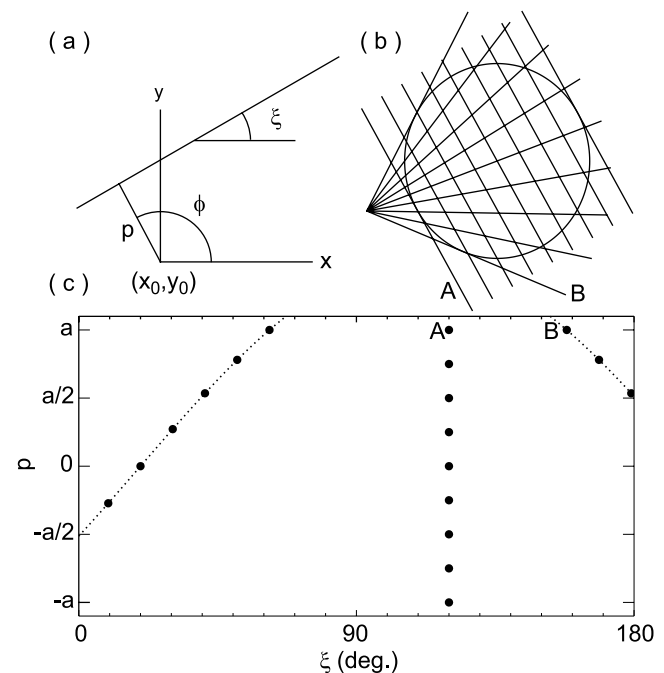
Fig. 9. (a) Definition of signed-distance $p = -(x - x_0)\sin\xi + (y - y_0)\cos\xi$ and angle ξ that parameterize a line of sight with respect to an origin (x_0, y_0) and equivalently projection angle ϕ. (b) Parallel-beam view, often referred to as a full projection, and a fan-beam view in xy space and a circle with radius a. (c) Equivalent projection-space points of the views of (b). A and B identify two particular lines of sight. The dotted curve corresponds to $p = -(x_{ap} - x_0)\sin\xi + (y_{ap} - y_0)\cos\xi$, where (x_{ap}, y_{ap}) are the coordinates of the fan focus.

the inversion of the function $f(p, \xi)$ can be obtained by two steps, filtering followed by so-called backprojection:

filtering:

$$h(p, \xi) = \mathcal{F}_1^{-1}\{|P|H(P)F(P, \xi)\}$$

$$= \int_{-\infty}^{\infty} f(p', \xi)\eta(p - p')\, \mathrm{d}p' \qquad (6)$$

and

backprojection:

$$g(x, y) = \int_0^{\pi} h(-(x - x_0)\sin\xi + (y - y_0)\cos\xi, \xi)\, \mathrm{d}\xi \quad ,$$

$$(7)$$

where

$\mathcal{F}_1$ = one-dimensional (1-D) Fourier transform with respect to p

P = Fourier variable of p

$F(P, \xi)$ = Fourier transform of $f(p, \xi)$

$\eta(p)$ = inverse Fourier transform of $|P|H(P)$.

With $H(P) = 1$, Eqs. (6) and (7) are a direct translation of the Radon inversion formula into the Fourier domain, with $|P|$ corresponding to the differential operator. It is clear that for large P, i.e., high spatial frequencies, the inversion is not well behaved. An artificial filter function $H(P)$ is therefore introduced as regularization, whose function is to reduce $|P|H(P)$ to zero at high P. This method of solution, the FBP method, can be implemented numerically very easily, is very efficient, and is therefore the most generally applied tomography algorithm in medical tomography and other fields. Equation (6) can be implemented in the P Fourier domain, with the filter function $|P|H(P)$, or in the p domain by means of the convolution and the equivalent filter function $\eta(p)$. Commonly used filter functions for regularization are described in Refs. 133 and 137. In mathematical terms, the backprojection operator of Eq. (7) is the adjoint of the Radon transform.[130,132]

Unfortunately, the FBP method is only effective for regularly sampled measurements from many directions; algorithms exist for parallel and fan-beam projections[134] illustrated in Fig. 9. The application within plasma physics is therefore limited, although it is possible to apply FBP and similar methods after appropriate interpolation to a regular grid in p and ξ (Ref. 153), usually with disappointing results. However, Eq. (6) illustrates a very important aspect that must be realized when applying tomography. Unless temporal information from signals is taken into account in the tomographic reconstructions (see Sec. IV.I.3 for ways in which this could be done), uncertainties in the measurement, such as statistical noise

in the measurement and systematic errors in the measurement (such as calibration errors, misalignments, and drifts), cannot be distinguished by the tomography algorithm. All uncertainties will therefore be referred to as noise in this context. Regularization is very effective in limiting adverse effects of noise at high spatial frequencies, such as random noise without correlation between neighboring channels. Of course, it is beneficial for the quality of reconstruction to minimize noise at high P, but if this is not possible, meaningful tomographic reconstructions can still be obtained with appropriate regularization. The result will merely contain a less detailed structure. However, the effects of low-P errors, for example, correlated noise between channels, calibration errors across a view, and spatial uncertainties and misalignments, cannot be reduced by mathematical means. Consequently, errors at low P can cause severe artifacts in the reconstructed $g(x, y)$, and it can be very difficult to assess the meaningfulness. Care must therefore be taken in the design of tomography systems to reduce low-P errors, for example, by determining the actual geometry with high accuracy.

IV.D. Coverage, Beam Widths, and Line-of-Sight Optimization

IV.D.1. Projection Space

The coordinates p and ξ of the parameterization of lines of sight introduced in Eq. (5) constitute a space often referred to as the projection space, i.e., the space of line integrals, or projections (each line of sight is represented by a point); see Fig. 9. The term "projection" typically refers to $f(p, \xi)$ for given ξ, i.e., the collection of measurements by parallel lines of sight covering a cross section in one particular direction. The spatial sampling of projection space by lines of sight is a convenient way to investigate and optimize line-of-sight distributions for a tomography system. An example is given in Fig. 10a (Ref. 164), where the range of p is $[-a, a]$, with a the maximum radius of the reconstruction region and that of ξ [0, 180 deg]. It is also common to use coordinates (p, ϕ), where $\phi = \xi + 90$ deg [note that this leads to changes in signs and sines and cosines in the definition of $p(\xi)$ in Fig. 9, $K(x, y)$ for line integrals, and Eq. (7)] in the ranges $[-a, a]$ and [0, 180 deg], or $(|p|, \phi)$ in the ranges $[0, a]$ and [0, 360 deg]. With the latter choice, the continuity at $p = 0$ is not clear. For a function $f(p, \xi)$, the following "Möbius periodicity" holds: $f(p, \xi + 180\ \mathrm{deg}) = f(-p, \xi)$. It is straightforward to show that the zeroth and higher moments of $f(p, \xi)$ in p and $g(x, y)$ in x and y are closely related, sometimes referred to as the consistency theorem:[131,165] The zeroth moment gives the total emissivity, and the projection of the 2-D center of mass of $g(x, y)$ in direction ξ corresponds to the 1-D center of mass in p of projection $f(p, \xi)$. Typically, the quantity measured, such as plasma emissivity, goes
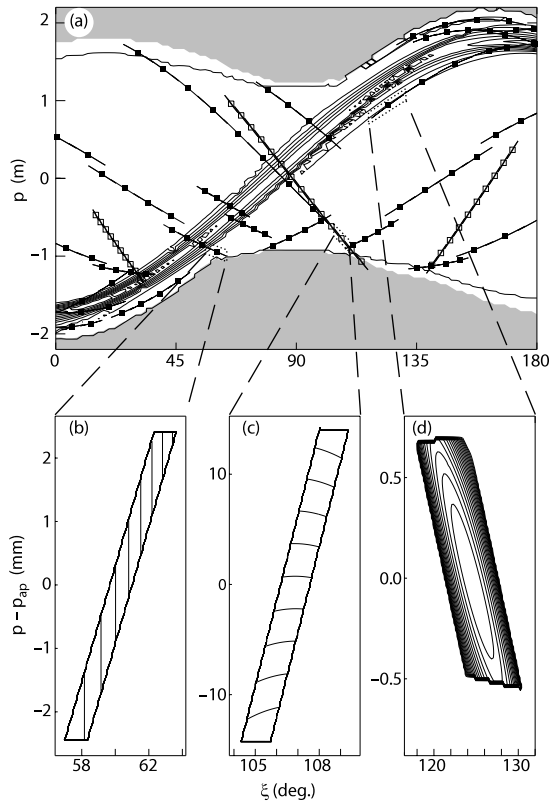
Fig. 10. Coverage in projection space and typical geometric functions in projection space for the JET bolometer system in 1996 (Ref. 164). (a) Contour plot of the sinogram of a typical total emission profile in the JET tokamak (calculated from a phantom similar to the emission profile in Fig. 16d). The origin was chosen on the magnetic axis of the tokamak cross section. The shaded area indicates where lines of sight pass outside the first wall of the tokamak. The points (solid and open squares) mark the (p, ξ) coordinates of the average lines of sight of the JET bolometer system. The outline of the regions in which $k_i(p, \xi)$ is nonzero is shown for each detector (visible only as thin lines). (b), (c), and (d) Blowup of three regions covered by three different bolometer geometries, where the contours indicate $k_i(p, \xi)$: (b) a rectangular pinhole system with parallel detector and aperture; (c) a rectangular pinhole system with nonparallel detector and aperture; (d) a system with a rectangular detector, a round collimator, and several other bounding apertures [contours in (b) and (c) are for a small variation from the maximum value]. In (b), (c), and (d), the p-axis has been stretched by subtracting $p_{ap}(\xi)$ values that correspond to the center of the front aperture as a function of ξ. (Figure reprinted with permission from Ref. 164.)

to zero on the boundary of a convex region. In the mathematical literature this is often referred to as the tomography problem having compact support. For MFE diagnostics, the region is not always convex, for example, for bolometer tomography in a divertor with a dome, in which case special provisions are needed in the projection-space description.[166]

IV.D.2. Coverage, Spatial Sampling, and Line-of-Sight Optimization

Projection space should be sampled as completely and regularly as possible. In medical tomography, this can mean a completely equidistant sampling (projections, i.e., parallel lines of sight, at many angles ξ) or regular fan-beam sampling; see Fig 9. This can hardly ever be achieved on MFE devices because of the constraints on access outlined in Sec. IV.A. Figures 10a and 11b show examples of typical coverage of bolometer and SXR systems on JET. Instead of complete projections or fans covering an entire cross section, a camera or view often only covers partial areas. It is important to take into account two aspects when designing a tomography system. First, for a given number of channels, it may be better to sample at more angles (views) each with fewer lines of sight than at fewer angles each with more lines of sight. This is because in the latter case the high resolution in p is partly annulled by a lack of information on the angular distribution. The information content in the measurement and reliable information that can be derived by tomographic reconstructions can be described; see, for instance, Refs. 167 and 168. For example, a rule of thumb has been derived for the useful number of projections (views) for a given number of lines of sight per view.[169] Note that the numbers found—typically the number of views should be larger than the number of channels per view—are normally impractical or impossible for MFE diagnostics, which illustrates the need to take a priori information into account in tomographic reconstructions by methods such as those discussed in Sec. IV.F. Second, it is important that every part of the emitting plasma be covered by two or more views. If there is only one view in some areas, tomography algorithms cannot derive a quantitative spatial distribution, unless a priori information about the emissivity in that area is provided to the algorithm. It may also be possible to extract qualitative rather than quantitative information about the emission profile, for example, by a specialist technique such as region-of-interest tomography, which has been applied in low-temperature plasma diagnostics.[170] The two requirements discussed above lead to the requirement of many views with many lines of sight each.

The sampling does not need to be regular, and it can be optimized given the constraints and the requirements. For this purpose it is useful to consider the function $f(p, \xi)$—often referred to as "sinogram" because of the characteristic shape of $f(p, \xi)$ for point sources in $g(x, y)$—for a number of representative emission profiles $g(x, y)$. This is illustrated for a particular generation of JET bolometers in Fig. 10, for which a reasonably optimized line-of-sight distribution was obtained within
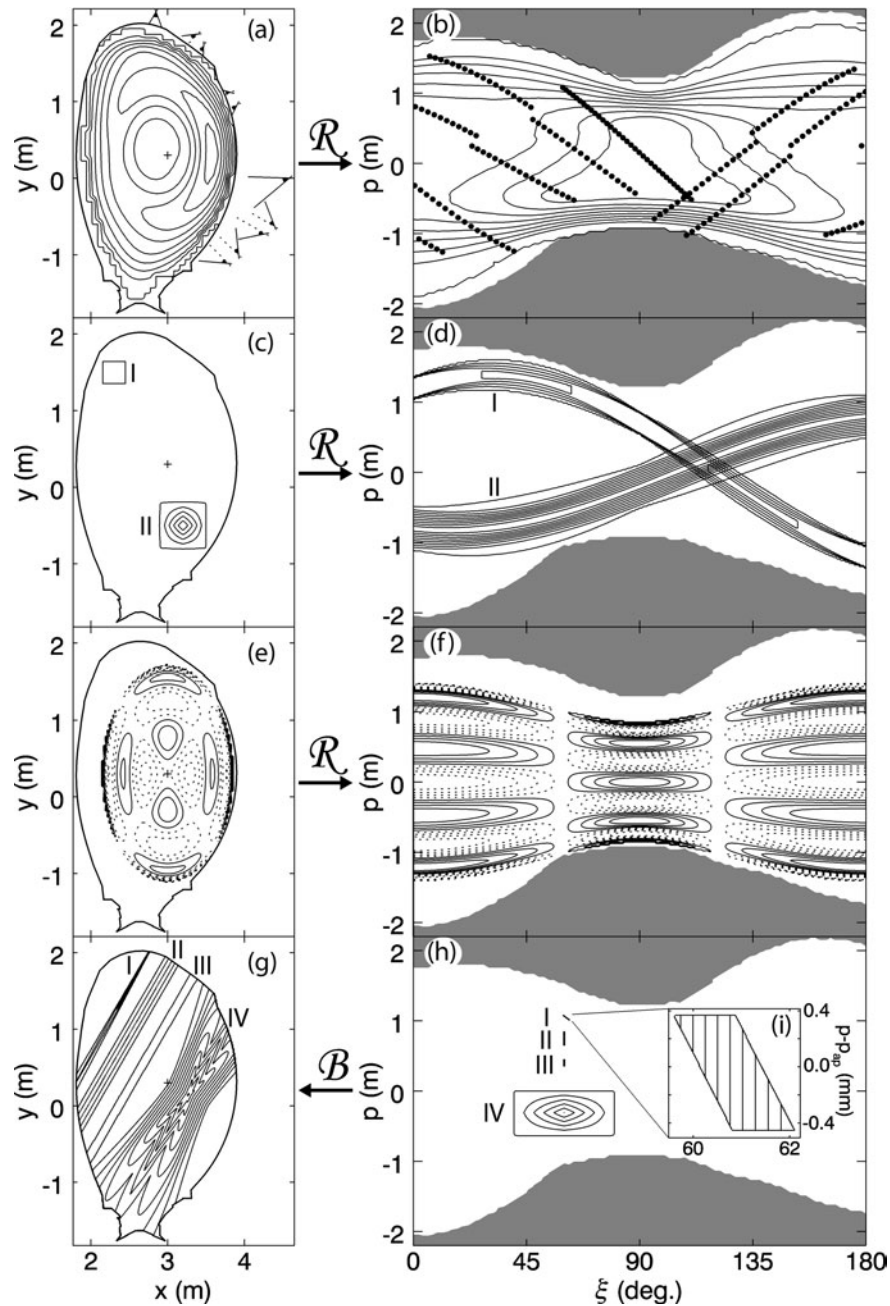
Fig. 11.   Illustration of various types of basis functions in xy space [(a), (c), (e), and (g)] and projection space [(b), (d), (f), and (h)] as contour plots. (a) and (b) SXR emission profile used as phantom (identical to Fig. 18a) and its sinogram. The fans in (a) indicate the extent of the viewing fans of the JET SXR imaging system (each with 18 channels, except the top one, which has 35 channels); the average lines of sight are indicated by points in (b). (c) and (d) Local basis functions (exaggerated size); I: square pixel; II: "pyramid" (linear interpolation between grid points). (e) and (f) One Cormack global basis function (cosine component with parameters $n = 2$, $m = 3$) (Ref. 182). Normally, the Cormack basis functions are given in polar coordinates; here, these coordinates have been transformed to elliptical coordinates by a linear stretching transformation (thus keeping straight lines straight) of (x, y) and (p, ξ) in the y direction. Negative values are indicated by dotted contours. (g) and (h) NBFs; I: geometric function of one SXR detector [blowup of projection-space coverage in (i); see Ref. 164 for details; $p_{ap}(\xi)$ is the p value that corresponds to lines through the center of the aperture]; II: triangular strip; III: constant strip; IV: basis functions corresponding to bilinear interpolation in projection space (exaggerated size). The relationship between xy space and projection-space quantities is indicated by the Radon $\mathcal{R}$ and backprojection $\mathcal{B}$ operators. The origin for projection space is indicated by a cross in (a), (c), (e), and (g). The boundary of the reconstruction region (the first-wall structures of the tokamak vacuum vessel) is given by a thick line; lines of sight passing outside the boundary are in the dark region indicated in projection space.

the technical constraints. The peaked emissivity in the divertor leads to a band in $f(p, \xi)$. The line-of-sight distribution has been optimized on the basis of this. The divertor radiation is sampled by four-channel views at regular angles, and the edge plasma, where there are steep gradients in emissivity, is also sampled at several angles, whereas the rest of projection space is covered more sparsely (irregularly because of the constraints). Every p value is sampled at several angles; thus, both aspects mentioned above have been satisfied. During an optimization like this, it may be beneficial to look in detail at particular regions of projection space, for example, by a change of origin (x_0, y_0) to another relevant location (e.g., the highly radiating divertor in the case of bolometry).[166] It may be useful to assess the appropriateness of the selected coverage by means of phantom simulations, as discussed in Sec. IV.H.1. A quantitative way to assess the "usefulness" of individual lines of sight as a means of optimizing the line-of-sight distribution was proposed and applied in Ref. 152.

It is generally a good idea to include a few overlapping lines of sight in opposite directions for cross-checking purposes. This way, measurements can be validated, and discrepancies can lead to important insights (see, e.g., Sec. IV.I.5). Uncommon algorithms[171] exist that experience singularities if the two measurements from opposite directions are not identical, which will always be in the presence of noise and systematic errors.

By considering the Fourier transform of a regularly sampled projection space, it can be theoretically demonstrated that the information content of interlaced sampling with half the number of lines of sight, i.e., alternating only even and odd points in neighboring projections, is almost the same as full sampling.[172] Although this insight is mainly of academic interest for most present-day MFE tomography systems, it may become relevant in future systems if significantly more views and lines of sight become available.

IV.D.3. Taking into Account Beam Widths, and the Line-Integral Approximation

In many applications, the measurements are assumed to be approximated by line integrals. All real measurement systems, however, measure along strips with a finite width. There are two reasons to optimize these beam widths: signal level and minimization of spatial aliasing. Spatial aliasing can occur if emitting structures are present in the plasma that are smaller than the distance between neighboring lines of sight. This effect is illustrated in Fig. 12 for the JET bolometer system. Finite beam widths will have a smoothing effect that has a similar effect to filtering above half the Nyquist frequency in data-acquisition systems for temporal sampling. It may therefore be of benefit to enlarge the beam widths so that the viewing beams of neighboring channels touch or even overlap, which also increases the sig-
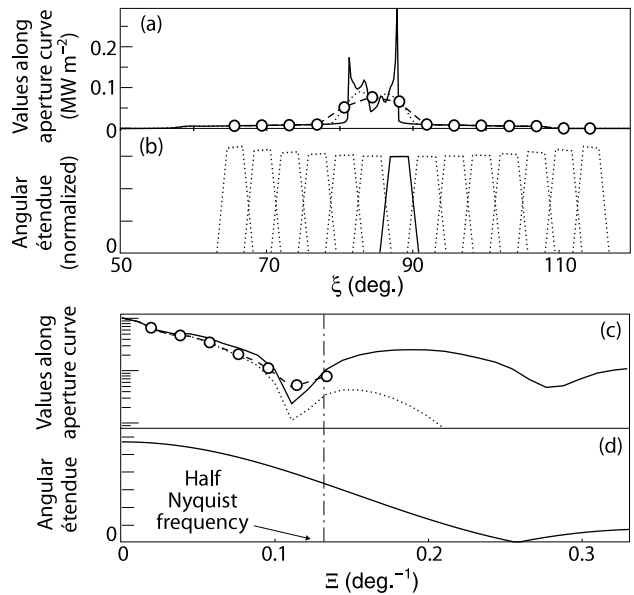
Fig. 12. Illustration of the antialiasing effect of finite beam widths.[173] Quantities along a curve $p(\xi)$ of all lines of sight through the center of an aperture for an array of bolometers viewing down into the divertor on JET, for a certain assumed emission profile similar to that of the phantom in Fig. 16a, as a function of the angle ξ [(a) and (b)] and its Fourier counterpart Ξ [(c) and (d)]. (a) Solid line: line-integral values; dotted line: values blurred by the "angular étendue," i.e., the integral of $k(p, \xi)$ over p; circles: points where the blurred values are sampled (corresponding to the detectors); dashed curve: piecewise-linear fit to sampled points. (b) Angular étendue normalized to the étendue for the 14-channel vertical bolometer camera; the one used in the investigation is given by the solid line. (c) and (d) Fourier transforms of (a) and (b), respectively, with equivalent line types and symbols. Note that (c) is on a logarithmic scale and (d) is on a linear scale. The dashed curve in (c) indicates the blurred function aliased with values higher than half the Nyquist frequency $[(2\Delta\xi)^{-1}$, where $\Delta\xi$ is the sampling rate; vertical dot-dashed line at $\Xi = 0.13$ deg^{-1}]; the circles indicate the sampling points on the dashed curve, which clearly show an aliasing effect even with relatively large beam widths [i.e., in (c) the dashed curve is higher than the unaliased dotted curve]. (*Figure reprinted with permission from Ref. 173; Copyright 2002, American Institute of Physics.*)

nal level. This has the added benefit that small structures in the emission profile cannot be overlooked, as otherwise they could be seen by narrow viewing beams from one direction but fall between two viewing beams from another direction. Optimization techniques to achieve adequate beam widths are described in Ref. 173, which shows that individual collimators for each channel (on an array or individually) offer more flexibility to optimize beam widths and signal levels than pinhole cameras for

detector arrays. Truly overlapping beam widths, which could be needed to avoid any spatial aliasing, can be difficult to achieve with the detector arrays often employed in tomography systems, unless they are displaced in the toroidal direction. Clearly, in the design of the collimator or pinhole cameras of tomography systems, compromises need to be made between allowable spatial aliasing, signal levels, and loss of too much spatial detail. It is important to realize that unlike what is sometimes thought, finite beam widths have several benefits and few drawbacks. Unless high-resolution views are available from many directions, it will be impossible anyway to resolve structures smaller than a few channel-to-channel distances by tomographic techniques. For tomography systems measuring in poloidal cross sections, the viewing extent in the toroidal direction is usually also maximized, in the interest of signal level, to the limit below which toroidal bending and toroidal asymmetries can be neglected.

It is important to adequately take into account the viewing geometry in the tomography algorithm, by means of the geometric function $K_i(x, y)$ in Eq. (5). In many cases approximations of $K_i(x, y)$, such as the line-integral approximation, are adequate, as is discussed below. For an exactly known geometry, $K_i(x, y)$ can be calculated analytically, taking into account properly the solid angle spanned by the detector seen through the aperture or collimator from each point (x, y, z) and integrated over z (assuming emissivity in the toroidal z direction is constant over the beam width in that direction). This is a cumbersome integral over several dimensions, and it can be shown[164] that calculation can be more effective through a geometric function in projection space $k_i(p, \xi)$, which is related by

$$K_i(x, y) = \iint k_i(p, \xi)$$
$$\times \delta(p + (x - x_0)$$
$$\times \sin \xi - (y - y_0)\cos \xi) \, \mathrm{d}p \, \mathrm{d}\xi \ , \qquad (8)$$

and $k_i(p, \xi)$ can be fully determined by the lines going through the detector and aperture or collimator (making allowance for the z dimension). Interestingly, Eq. (8) is equivalent to backprojection Eq. (7). Examples of $k_i(p, \xi)$ are shown for three bolometer detectors at JET in Figs. 10b, 10c, and 10d. The most straightforward way is to approximate the views with finite beam widths by line integrals. In this case the geometry is taken into account by the so-called étendue of the optical system[164]

$$E_i = \iint \frac{k_i(p, \xi)}{\cos(\xi - \bar{\xi}_i)} \, \mathrm{d}p \, \mathrm{d}\xi \ , \qquad (9)$$

where $\bar{\xi}_i$ is the angle of the central approximating line of sight. For simple pinhole systems the approximation of the étendue by the solid angle spanned by the aperture as

seen by the detector, multiplied by the detector area, may be adequate.[14,23,164,173,174] For more-complicated collimator systems, Eq. (9) can be used. The requirement for the line-of-sight approximation to be applicable is that emission does not vary in cross sections of the beam width or, equivalently, that the sinogram does not vary over the area where $k_i(p, \xi)$ is nonzero. In reality it is found, however, that the line-integral approximation can also be adequate when the emission profile is varying smoothly over the beam width. Only when the beam widths are wide with respect to the radiating structures that are observed is it necessary to use the full geometric information in $K_i(x, y)$. This may be the case, for example, in bolometer tomography of divertor plasmas. Even in this case, it is common to scale bolometer signals by the étendue to obtain signals in $W \, m^{-2} \, sr^{-1}$ or $W \, m^{-2}$ (in the latter case isotropic emission has been assumed), as in Fig. 6, so that signals from channels with quite different étendues can be compared more easily [obviously, this scaling must be undone before the full $K_i(x, y)$ is taken into account in the tomographic reconstruction]. Note that the line integral in $W \, m^{-2}$ is a very different quantity than the radiative power load onto the wall, which has the same dimension.

The viewing geometry after installation is not always adequately known, and $K_i(x, y)$ cannot be calculated. In such a case it may be possible to determine $K_i(x, y)$ or $k_i(p, \xi)$ by measurement.[174,175] When designing tomography systems, it is important that provisions be made for adequate determination of the geometry of the system as installed; otherwise, artifacts will appear in reconstructions, as pointed out in Sec. IV.C. In the series-expansion tomography methods with local basis functions as described in Sec. IV.E, which are most commonly applied to MFE diagnostic data, $K_i(x, y)$ will be used, and $k_i(p, \xi)$ is at most a useful intermediary, for example, for experimental or numerical determination of $K_i(x, y)$. For tomography methods that operate in projection space, it is often difficult to implement exact geometric information unless it is shift invariant. Exceptions are the Cormack method and the method described in Ref. 153, in which $k_i(p, \xi)$ can be fully taken into account.[176] In other fields of tomography, either beam widths are negligible, or the correction is usually done very differently by methods not applicable to the MFE diagnostic. In those cases, $k_i(p, \xi)$ is usually shift-invariant for all channels because of symmetry in views, and therefore, beam widths can be taken into account in Fourier space, e.g., Refs. 177 and 178 and references in Ref. 164.

IV.E. Series Expansion

IV.E.1. Introduction to Series Expansion onto Basis Functions

Basically, there are two approaches to the inversion of Eq. (5): analytical inversion and subsequent numerical

implementation (digitization), or digitization of Eq. (5) followed by numerical inversion.[137] The former are sometimes referred to as "transform methods," and the FBP and many Fourier methods are examples. These can be very efficient. However, often the sampling must be regular, and there are limited possibilities to take into account a priori information. The second approach to inversion is often referred to as series expansion, as the function $g(x, y)$ is approximated by an expansion on a suitable set of basis functions $b_j(x, y)$:

$$g(x, y) \approx \sum_j g_j b_j(x, y) \ , \tag{10}$$

with expansion coefficients g_j. Substitution of Eq. (10) into Eq. (5) yields the system of equations

$$f_i = \sum_j K_{ij} g_j \ , \tag{11}$$

(or equivalently the matrix equation $f = Kg$), where

$$K_{ij} = \iint K_i(x, y) b_j(x, y) \, \mathrm{d}x \, \mathrm{d}y \ . \tag{12}$$

The solution $g(x, y)$ can be obtained by solving Eq. (11) and subsequent application of Eq. (10); this will be discussed in Sec. IV.F.

There are essentially three different types of basis functions applied in tomography algorithms: local basis functions, global basis functions, and natural basis functions (NBFs). These are illustrated in Figs. 11c, 11e, and 11g, and the corresponding projection space shapes in Figs. 11d, 11f, and 11h. These three types will be described in detail below.

IV.E.2. Local Basis Functions

Local basis functions include square pixels (I in Fig. 11c) and other localized functions.[179] An attractive local basis function is shaped like a pyramid with rounded corners (II in Fig. 11c) and overlaps halfway with the neighboring basis functions. This ensures continuity of the function $g(x, y)$ in the grid points and therefore is a much more accurate representation of functions than pixels, at minimal additional computational cost.[179,180] Other shapes of pixels that have been applied are sections of rings that match the flux surfaces.[35,151] Sometimes, tomography algorithms using pixels have been referred to as finite element methods in the literature, which is confusing, as the algorithms only make use of a scalar value of each pixel (the emissivity), rather than quantities flowing between finite elements. Local basis functions on a regular grid ensure a great deal of flexibility for the adequate description of $g(x, y)$, without imposing any particular functional shape on the solution.

IV.E.3. Global Basis Functions

The best known type of global basis function is used in the Cormack tomography method. This method was proposed by Cormack in 1963 (Refs. 181 and 182); he is one of the inventors of computed tomography for medical applications. In this method, $g(x, y)$ is expanded into circular harmonics (i.e., sin and cos in poloidal angle) and Zernike polynomials in the radial direction (see Fig. 11e). The Radon transform of this expansion can be obtained analytically, expressed[182] in circular harmonics in ξ and Chebyshev functions of the second kind in p (see Fig. 11f). The inversion is obtained by fitting the measurements f_i to the expansion on an orthogonal basis in projection space. This gives the coefficients to be inserted in Eq. (10). Because the Radon inverse of the fitting basis functions in projection space is known analytically, the Cormack method can also be regarded as a transform method. Several variations to the Cormack method exist, for example, replacing the Zernike polynomials by Bessel function,[141,183,184] which are better suited to describe SXR emission in tokamaks, or other "circular harmonic" methods.[137,185] The Cormack method was not very suited for medical tomography, but it was a good choice for two-camera SXR tomography in the early days of its application on MFE devices, especially on circular tokamaks with a small Shafranov shift, as the functional structure is well adapted to MHD modes occurring. It therefore found wide and very successful application in SXR tomography in MFE devices with circular cross section.[13,14,18,141,186,187] For other plasma shapes (such as the elongated D-shaped plasma illustrated in Fig. 11a) and multicamera systems, the usefulness of the Cormack method is limited as higher harmonics in the expansion are wasted on describing the inadequacies of the basis functions to describe the basis emission profile shape, rather than on representing information on the fine structure of the emission profile. Some adaptations of the Cormack method to cope with the actual geometry of flux surfaces[188,189] have found only limited applicability. On the present-day SXR tomography systems and with fast computers available, other reconstruction methods often perform better; see Secs. IV.F and Sec. IV.G.

IV.E.4. Natural Basis Functions

The third type of basis function, NBFs or natural pixels,[169,190,191] is based on the functional shape of $K_i(x, y)$, i.e., the viewing geometry (see Fig. 11g for some examples). NBFs have been applied successfully in single positron emission computed medical tomography,[192] which has some similarities with MFE tomography systems. It is claimed that this choice of basis function is particularly good for small numbers of measurements, if the coverage is regular, as the solution is described by the information about the measurement (geometry and measured values).[179,190] However, the basis functions are not orthogonal, and the implementation in the case of irregular coverage is not trivial.[191] Nevertheless, because of their properties to optimally represent the measurements and requiring a minimal

amount of a priori information, it has found some use in MFE tomography to ascertain that features observed are not artifacts induced by other regularization methods (Fig. 13) (the use of a priori information is discussed in more detail in Sec. IV.F.2) (Ref. 191). Because of the nature of NBFs, Eq. (10) actually corresponds to the backprojection operator of Eq. (7) (Refs. 191 and 192).

IV.E.5. Considerations on Choice of Basis Functions, Number of Basis Functions, and Numerical Implementation

Series-expansion methods using a large number of basis functions (such as pixels or grid points) are computationally much more involved than transform methods. When symmetric views are present, this leads to symmetries in K that can be exploited.[193] With some of the linear methods described in Sec. IV.F, computation time is not an issue any more on modern computers.

The computation and solution are affected by the chosen number of basis functions (such as the number of grid points). It is sometimes not realized that the number of basis functions is not necessarily bound by the number of measurements, as the regularization methods described in Sec. IV.F can deal with Eq. (11) if it is underdetermined. For local basis functions it is our preference that the solution be determined by only the a priori information (such as the objective functionals described in Sec. IV.F) and the measurements, and not by the choice of type or number of basis functions. As the computational efficiency depends strongly on the number J of basis functions (roughly as J^2 to J^3, depending on the solution method), there is an incentive to minimize J. Because the distance between neighboring lines of sight determines the minimum size of features of the emission profile that could possibly be distinguished in the measurements, as a rule of thumb one can therefore choose the size of the basis functions similar to the average distance between lines of sight (at the expense of programming complexity, one could also choose varying sizes over the reconstruction region; see Sec. IV.G). By repeating tomographic reconstructions with different grid sizes, one can easily establish a limiting size below which the solution does not depend on the choice. Note that this may lead to thousands of grid points (i.e., unknowns), while only having of the order of 100 measurements; this is not a major problem. With NBFs, the number of basis functions is naturally limited to (about) the number of measurements. Because it is difficult to use a priori information in the Cormack method, the number of expansion coefficients is limited to avoid spatial aliasing (for optimization, see Ref. 141 and Sec. IV.I.3). In particular, the number of angular harmonics is limited by the number of full views of the plasma.

To minimize the amount of a priori information needed, some researchers decide to limit the number of basis functions to ensure that Eq. (11) is overdetermined. This indeed regularizes the reconstruction (i.e., ensuring a unique well-behaved solution), but it is rather arbitrary because the solution may depend sensitively on the exact number of basis functions (i.e., the solution may change significantly if one more or less basis function is used). Great care is therefore needed if this approach is adopted. The Akaike Information Criterion provides a means to optimize the number of free parameters, such as the number of local basis functions[147] or the number of Cormack expansion coefficients[141] in dependence on the measurements and geometry [in fact in dependence on the residual $\|f - Kg\|$ in Eq. (13)]. This may be the information theory equivalent of the approach above that the number of basis functions should be such that all detail available in the measurements can be expressed in the reconstructed emission profile.

Because of the flexibility of using arbitrary line-of-sight distributions and a wide range of a priori information (to complement a lack of information in the measurements, see Sec. IV.F), the use of series-expansion methods, in particular, with local basis functions, is often the preferred approach for tomography on MFE devices, given the boundary conditions discussed in Sec. IV.A.

IV.E.6. Parametric Models

There are alternatives to approximation of $g(x, y)$ by a linear series expansion in orthogonal or nonorthogonal basis functions as in Eq. (10), such as a parameterized nonlinear function that is expected to describe the emission profile well. A tomographic reconstruction can be obtained by least-squares fitting to such a parametric model. Although this can be adequate provided the parametric model provides a satisfactory description of the emission profile, one should remember that the nature of ill-posed problems typically makes parameters very insensitively dependent on line-integral measurements and furthermore that several parameters are correlated. The choice of method depends on the flexibility required and how much knowledge is available about the expected emission profiles.

IV.F. Regularization

In this section and in Sec. VI.G, it will be assumed that a series expansion has been made on local basis functions and that thus to obtain the tomographic inversion, Eq. (11) needs to be solved, taking into account its ill-posed nature. The ill-posedness typically manifests itself in the matrix K (or $K^{\mathrm{T}}K$) having many small eigenvalues or singular values,[138] which makes it necessary to regularize the problem to be able to obtain a well-behaved solution. Although an eigenanalysis of the matrix K gives useful insight into its characteristics, for example, the range and null-space,[194] the singular value

decomposition (SVD) is a superior analysis tool for ill-posed problems.[138,195] A "condition number," typically the ratio of the largest and smallest singular values, quantifies the ill-posedness.

IV.F.1. Truncated SVD and Iterative Approaches Without Specific A Priori Information

A very straightforward and robust method to solve Eq. (11) is by truncated SVD (TSVD) (Refs. 138 and 195); algorithms are available in many mathematical packages. The truncation effectively removes the small singular values, which are related to the eigenvalues of K^TK and KK^T, below a level set by the user, thus regularizing the problem. The truncation level to be chosen depends on the range of singular values and the noise level of the measurement. There are also iterative ways to solve Eq. (11), for example, by the Kaczmarz method. This was implemented in ART in the early days of computed tomography, as the iterative method could be implemented relatively efficiently and make efficient use of computer memory. Many variations of ART exist.[133] Regularization is achieved by breaking the iterations at a suitable point[130] and introducing relaxation parameters. Both TSVD and ART can be shown to give the least-squares solution if Eq. (11) is overdetermined, and the minimum-norm solution if Eq. (11) is underdetermined.[133,138,195] These methods use a minimum amount of a priori information: essentially only the choice of truncation level. If the matrix K and measurements f contain insufficient information to be able to provide a physically meaningful reconstruction, as is often the case in MFE diagnostics, this may be a disadvantage, in which case the following methods should be considered.

IV.F.2. Constrained Optimization, Phillips-Tikhonov Regularization, and the Use of A Priori Information

The second way to deal with the small eigenvalues or singular values of the matrix K is to transform Eq. (11) into a different system of equations that does not have small eigenvalues or singular values. This can be done effectively by adding a priori information about the expected emission profile. The requirement is that this a priori information adds information about the subspace of solution space that goes unnoticed by the measurements (i.e., the null-space of K) (Refs. 136, 179, and 194). This requirement is easily satisfied; e.g., the knowledge that the solution should be zero outside the vacuum vessel already adds to the regularization. However, the degree to which the a priori information adds to the measurement is the key to successful tomographic reconstruction. This is most relevant if Eq. (11) is underdetermined, which generally is the case in MFE applications (see the discussion in Sec. IV.E on choosing a sufficient number of basis functions). Tomography with a coverage with only a few views at restricted angles, as is usually the case in MFE diagnostics, is often referred to as "missing angle tomography" or "limited angle tomography." A priori information plays a very important role to fill the gap in information of the "missing" angles. The effect of a priori information on the quality of the reconstruction is illustrated by Fig. 13. Application of TSVD with different basis functions (Figs. 13b and 13c) leads to features in the reconstruction that are rather erratic, while if a priori information about the smoothness of the solution on flux surfaces is assumed (see below for a description of how this is achieved), the reconstruction is closer to what would be expected from plasma physics considerations (Fig. 13a) (Ref. 191).

A convenient way to introduce a priori information is by describing a desired or expected property of the emission profile $g(x, y)$ (vector g in discretized form) by an objective (or penalty) functional $O(g)$. The measurements can be considered as constraint:

$$C(g) = \|f - Kg\|^2 - \|\varepsilon\|^2 \ , \tag{13}$$

where ε is the estimated noise level. Alternatively, it is often useful to weight the contribution of each measurement by its estimated error, which leads to a slight modification of $C(g)$ and Eq. (15) (Refs. 56 and 180). Assuming minimization of $O(g)$ is desirable, the solution g can be found by the constrained optimization problem

$$\min\{O(g)|C(g) \leq 0\} \ . \tag{14}$$

If the objective functional is quadratic, e.g., $O(g) = \langle g|\Omega|g\rangle$ using Dirac notation of the scalar product with matrix Ω, the Lagrange multiplier method applied to Eq. (14) gives[180]

$$(\lambda K^TK + \Omega)g = \lambda K^Tf \ , \tag{15}$$

where $\Omega^T = \Omega$ has been assumed. For a given Lagrange multiplier λ, which acts as the regularization parameter, inversion of Eq. (15) gives the solution g. The required λ can be found by requiring the constraint Eq. (13), often referred to as the discrepancy principle,[136] to be satisfied. Figure 14 shows for a practical case the functional dependence of O and C on λ, illustrating that there is a unique solution for $C(g) = 0$ (Ref. 136), i.e., with an equal sign rather than $C(g) \leq 0$. In fact it can be proven that a solution exists and is unique on the condition that the measurements exceed the noise.[136] Because the functional behavior is monotonic, it is straightforward to find λ iteratively by solving Eq. (15) for different values of λ, e.g., Ref. 149. Although solving Eq. (15) is time consuming (especially when many grid points are used), in practice only of the order of ten iterations are required to find λ. There are also ways to express the solution of Eq. (15) analytically in terms of λ and thus requiring only one inversion of a matrix equation, for example, by expressing the solution in
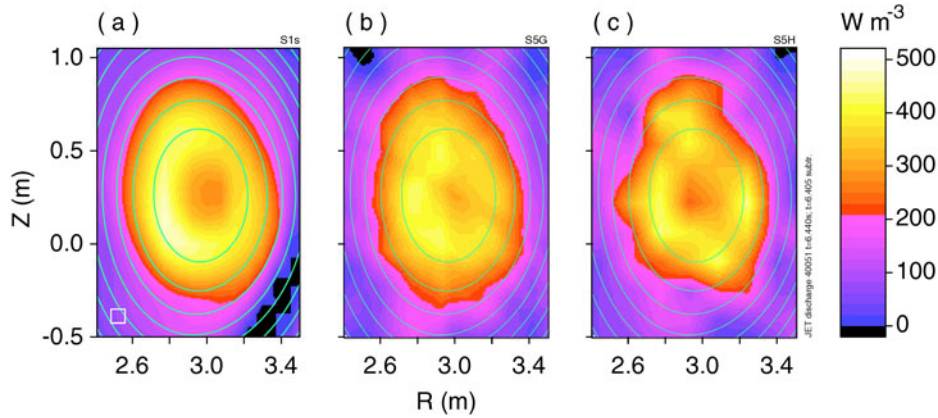
Fig. 13. Illustration of the effect of a priori information on the tomographic reconstruction with the JET SXR diagnostic (JET discharge #40051; background subtracted).[191] (a) Reconstruction by constrained optimization with an objective functional that penalizes solutions that are not smooth on flux surfaces (Sec. IV.F.3) ensures the smoothest solution within the measurement errors, which is closest to the expectations from plasma physics knowledge. The grid size is indicated in the lower left corner. However, to ascertain that the features deviating from constant values on flux surfaces were not artifacts of the assumptions and reconstruction method, the result was compared with reconstruction with a minimum of a priori information imposed, by application of TSVD on natural (b) and local (c) basis functions (Sec. IV.E). In this case, with more than 200 lines of sight, reconstructions with TSVD did give adequate reconstructions, but this is unlikely to be the case for sparser coverage. Generally, in the application of tomography to MFE diagnostics, a priori information plays a key role for obtaining adequate and meaningful results. (*Figure reprinted with permission from Ref. 191.*)
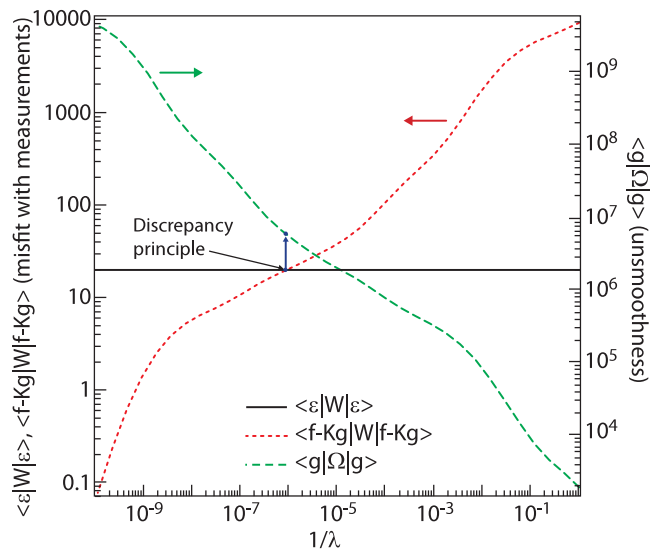

Fig. 14. Typical example of the competing functions in constrained optimization as a function of the inverse of the Lagrange multiplier $1/\lambda$ (the regularization parameter): the misfit $\langle f - Kg | W | f - Kg \rangle$ weighted by the estimated errors $W_i = 1/\varepsilon_i$ (dotted line) and the unsmoothness $O(g) = \langle g | \Omega | g \rangle$ (dashed line), where Dirac notation has been used for inner products. The solid circles show the optimized Lagrange multiplier according to the discrepancy principle, i.e., where the misfit equals the estimated errors $\langle \varepsilon | W | \varepsilon \rangle = M$ (solid line) (in the weighted case this is the number of channels M).

terms of the eigenvalues and eigenvectors of a generalized eigenvalue problem,[194] or in terms of singular values and vectors of the SVD or QR decomposition.[196]

Although Eq. (15) was the result of constrained optimization, it corresponds to the well-known Phillips-Tikhonov regularization proposed for regularizing the solving of the matrix equation Eq. (11) (in general with regularization parameter $\alpha = 1/\lambda$) (Refs. 127, 128, 136, and 138). However, Phillips-Tikhonov regularization does not necessarily use the discrepancy principle Eq. (13) to optimize λ, but other methods. Very extensive literature exists on methods to determine an adequate regularization parameter; see, for instance, Refs. 136 and 138. It is clear that for large λ the information from the measurement and measurement geometry will have the dominant influence on the solution, whereas for small λ the information in the objective functional will dominate. A plot of $O(g)$ against $\| f - Kg \|^2$ will typically have the shape of an L, and a good balance between $O(g)$ and $\| f - Kg \|^2$ is found by choosing λ at the "corner" of the L-curve.[138] Also, statistical considerations, such as generalized cross validation, can be used to select an optimum λ (Refs. 148 and 196). For physicists, however, the discrepancy principle Eq. (13) is very attractive as usually insight on the noise level is available and should be taken into account, while for mathematicians other choices may be preferable. It is common, also when using simulated data, that slightly underestimating the noise in the discrepancy principle Eq. (13) leads to more accurate reconstructions compared with using the upper limit of the expected noise or

even the actual noise level.[144,194] It is therefore useful to use rather low estimated noise levels for which no apparent artifacts occur in the reconstruction. However, if the noise level is significantly underestimated, severe artifacts related to the measurement noise will appear in the reconstructions.

IV.F.3. Objective Functionals

The next step is the choice of appropriate objective functional $O(g)$. In Phillips-Tikhonov regularization often the simple choice $O(\boldsymbol{g}) = \|\boldsymbol{g}\|^2$ (minimum norm) is used, which in principle corresponds to solutions found by TSVD and ART (Ref. 138). Another choice is maximum entropy[5,143,144,168,197,198]: $O(\boldsymbol{g}) = \sum_j g_j \ln g_j$, or the closely related minimum cross entropy.[199] This objective functional can be derived from Bayesian statistics considerations and probabilistic inference, and the result is the most probable and least biased solution consistent with the available noisy data.[144] As the choice of maximum entropy objective functional is nonlinear, Eq. (14) has to be solved by other numerical means than explained above and is typically time consuming.

For applications to MFE diagnostics, however, it may be beneficial to take into account further a priori knowledge about the expected solution. A wide class of quadratic objective functionals can be defined in Cartesian coordinates by

$$O(\boldsymbol{g}) = \langle \boldsymbol{g} | \Omega | \boldsymbol{g} \rangle$$

$$= \iint \left[c_0 g^2 + c_x \left(\frac{\partial g}{\partial x} \right)^2 + c_y \left(\frac{\partial g}{\partial y} \right)^2 + c_{xx} \left(\frac{\partial^2 g}{\partial x^2} \right)^2 \right.$$

$$\left. + 2c_{xy} \left(\frac{\partial^2 g}{\partial x \partial y} \right)^2 + c_{yy} \left(\frac{\partial^2 g}{\partial y^2} \right)^2 \right] dx \, dy \ , \quad (16)$$

where all coefficients c can be chosen to suit a particular emission profile and can depend on x and y. If c_0 is set to a large value outside the nominal plasma and zero inside, minimization of the objective functional will favor solutions with small values outside the plasma. The first-derivative terms will favor small gradients in the locations where $c_{x,y}$ is set nonzero. Finally, the second derivatives will favor solutions that are smooth. The Laplacian terms, i.e., second-derivative terms with $c_{xx} = c_{yy}$, are a very common choice in Phillips-Tiknonov regularization.[128,148,196] Smoothness is a very general and important property of emission profiles and a powerful way to regularize the solution. Even if the emission profile is known not to be smooth, it usually will be on the spatial scale that can be resolved by the lines of sight available, and therefore, a smooth profile will be a fair representation given the available measurements. As the emission profile in MFE devices, in

first approximation, usually is expected to be smoother on flux surfaces than radially, an objective functional similar to smoothness in Cartesian coordinates was introduced by Fuchs,[38,56,180] which has proven very powerful in tomographic reconstructions on MFE devices, in particular, in bolometer tomography and tomography with a limited number of views. This is achieved by differentiating between diffusion coefficients—diffusion of the mathematical values of the emissivity, without a direct link to plasma transport—parallel and perpendicular to the magnetic flux surfaces. For bolometer tomography of a divertor plasma, the diffusion coefficients must be suitably adapted in the X-point and divertor region to allow for appropriate gradients in emissivity along the nonclosed flux surfaces.

Tomographic reconstructions using objective functionals such as Eq. (16) will often oversmooth the peaks in the emission profile, especially at high noise levels. Anton et al.[23] proposed to use a linearized version of the minimum Fisher information criterion in the objective functional. Effectively, this weights the coefficients of Eq. (16)—typically the Laplacian terms only are used—in each grid point by the emissivity value g in that grid point (obviously, g is not known beforehand, and therefore the method has to be implemented iteratively; usually one or two iterations suffice). The result is that smoothness is reduced in locations where $g(x, y)$ peaks, thus reducing oversmoothing. Although this may be effective in bringing out details of the reconstruction, it also has some drawbacks, discussed in Sec. IV.H.3. The problem of oversmoothing originates from the noise level not being taken into account individually (see also Sec. IV.I.5) but is summed over all channels (weighting the measurements by noise level reduces the problem but does not eliminate it). Other approaches, which may solve some of the problems of the global nature, have been proposed in the literature, for example, in Ref. 200.

IV.F.4. Further Considerations on Regularization and the Choice of Objective Functionals

Regularized solutions with quadratic objective functionals can lead to unphysical negative emissivities, especially in the case of the emission profile having small peaked structures and steep gradients, which are often encountered in bolometer tomography of the divertor plasma (see Sec. IV.I.5). Such negative overshoots are related to overshoots appearing in the Fourier expansion of steep gradients with a limited number of terms. The negative spikes cannot be ignored, as the position and magnitude of the positive spikes may otherwise be incorrectly interpreted. It is therefore often necessary to impose a positive solution. Nonnegativity constraints can be implemented in various ways. Some standard algorithms used for the optimization of Eq. (14) or Eq. (15) allow the addition of constraints on $\boldsymbol{g}$ in every location. This can computationally be very heavy, and it may be

more effective to use a method developed by Fehmers et al.[194] or other iterative methods that set constraints only on locations that have been negative in earlier reconstructions.

For a sufficiently large set of basis functions, the choice of a priori information only has a weak influence on the solution. The objective functional will only bias the solution in a direction and not show the expected property unless the input data, i.e., measurements and noise level, support it. This is unlike parametric fitting or some choices of restrictive basis functions (e.g., the Cormack method or pixels shaped after the flux surfaces), in which case a solution may be found that is not supported well by the measurements. It is therefore important to cross-check the values of Kg, i.e., the "backcalculated solution" where g is the solution found, with f.

It can be difficult to select the optimum regularization parameter among the many different objective functionals and criteria that have been proposed in the literature. The choice is often based on personal preference, such as being mathematically oriented or satisfying the intuition of the experimental physicist. Although a functional like Eq. (16) generally gives very good results and many of the choices made for the coefficients can be justified from physics considerations, it contains several rather arbitrary choices, such as the weight of nonzero values with respect to unflatness and unsmoothness, that affect the solution obtained. As long as the objective functional chosen provides adequate regularization, the choice may actually not be very important, provided the user is well aware of the limitations. In general, a physicist is not interested in one unique "best" solution but rather in the range of solutions that is reasonable within the experimental errors and experimental assumptions. As discussed in Sec. IV.H, it may therefore be important to compare several methods and variation of reconstruction parameters within reasonable ranges.

In phantom simulations, synthetic measurements for the given phantom are calculated with Eq. (5) or Eq. (11), a realistic level of random noise is added, and a reconstruction is made using the synthetic measurements. Figure 15 shows a typical example of the use of phantom simulations to compare different objective functionals and regularization methods. Phantom simulations are an essential standard tool to understand the reliability of the results obtained (see Sec. IV.H).
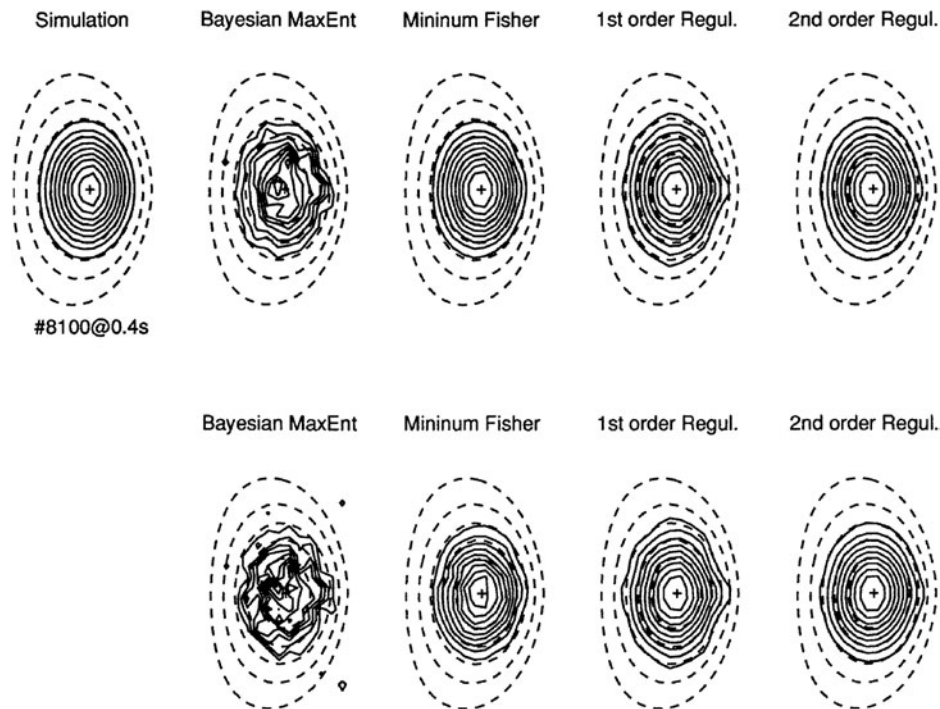
Fig. 15. Example of a comparison of different regularization methods in phantom simulations (phantom in top-left corner) for two noise levels: no added noise (i.e., only numerical errors) in the top row, and 2.5% relative noise in the bottom row.[23] The regularization methods compared are maximum entropy, linearized minimum Fisher, first derivatives (flatness), and second derivatives, as described in Sec. IV.F. The minimum Fisher and second derivatives seem comparable and to be the preferred methods. However, phantom simulations with more complex structures (MHD island structures) showed that the second derivatives oversmooth the result and that minimum Fisher is preferred, and even the maximum entropy method gave more accurate results, except for a high noise level. (*Figure reprinted with permission from Ref. 23.*)

It is possible to apply a constrained optimization with second-derivative terms as in Eq. (16) to an NBF expansion in projection space. As was pointed out in Sec. IV.E, with NBFs, Eq. (10) corresponds to the back-projection, and therefore, the constrained optimization in projection space corresponds to the FBP filtering of Eq. (6). Such an implementation of NBFs can therefore be seen as a discrete implementation of FBP, bringing transform and series-expansion methods together. Requiring smoothness of the solution by the objective functional—in particular in projection space, but a smooth function in projection space will also be smooth in xy space—can therefore be considered equivalent to filtering out high spatial frequency components with FBP.

IV.G. Numerical Implementation

For tomography methods based on constrained optimization using local basis functions, the practical implementation of a tomography program typically consists of the following steps:

Step 1: preprocessing of the experimental data, such as selecting a time slice and dealing with unreliable channels

Step 2: defining the reconstruction grid and basis functions

Step 3: defining the geometry matrix K

Step 4: calculating the matrix Ω for the chosen quadratic objective functional

Step 5: inversion

Step 6: postprocessing, such as graphical display of the reconstruction and backcalculated signals and processing of objective information (Sec. IV.H.2).

The development of tools for phantom simulations is also required. Some notes on several of these steps are given next. Further details for practical implementation can be found in Ref. 180.

After the grid and basis functions have been chosen (step 2), the geometric matrix K is calculated from Eq. (12) (step 3). This is straightforward when the line-integral approximation can be used as described in Sec. IV.D.3. In case beam widths are important, calculation of the geometry with equations such as $k_i(p, \xi)$ and Eq. (8), and the discretization of Eq. (12), can be time consuming but generally only needs to be done once.

Step 4 is the calculation of the matrix Ω related to the objective functionals such as Eq. (16). In discrete form, Ω can conveniently be written in terms of derivative matrices.[56,133,180,201] Generally, these are very large matrices, and straightforward multiplication can be very time consuming and require much computer memory. This is also the case for the matrix operations needed in prepa-ration of the inversion step 5, such as the term $\lambda K^T K + \Omega$ in Eq. (15). As most matrices have very many zero elements, techniques for sparse-matrix storage and operations on these matrices may be of great benefit to speed up the calculations. Although it is likely to add considerably to the complexity of implementation and is not needed for stability in well-regularized algorithms, it may also be of benefit to use different grid sizes in different regions in the plasma, such as a fine grid where needed (e.g., in the divertor to be able to resolve details in the expected radiating features) and a coarser grid everywhere else,[180] as the calculation time depends strongly on the total number of grid points.

The numerical implementation of the algorithms in step 5, the inversion, is generally straightforward, as for the most complex operations, such as constrained optimization Eq. (14) for nonlinear problems, solving the matrix equation Eq. (15) for linear constrained optimization, or performing TSVD on Eq. (11), use can be made of appropriate standard mathematical packages (such as NAG, MATLAB, and LAPACK). Because the sparseness of the matrices is usually not regular as the result of the typically irregular coverage in MFE diagnostics, it is generally not possible to take advantage of sparse-matrix versions of the inversion routines or fast algorithms for matrices with regular structure, unlike the application of tomography in other fields. The optimization of the regularization parameter in constrained optimization is achieved by the methods described in Sec. IV.F.2.

When developing tomography codes, often the largest effort is not with the algorithm for tomographic reconstruction itself, but in integration of diagnostic details (such as taking into account all relevant information: noise level, beam widths, and perturbing effects), in the preprocessing (such as for the graphical display of signals and deselection of unreliable channels) and in postprocessing (i.e., steps 1 and 6 described above), in the testing with phantom simulations (see Sec. IV.H), and in gaining the required experience to derive reliable physical quantities by the mathematical techniques.

IV.H. Objective Information

For the physicist it is very important to know how reliable specific features of the tomographically reconstructed emission profiles are. Phantom simulations are one of the tools to assess the capabilities and reliability of the diagnostic technique, but they also serve other purposes discussed below. In diagnostic practice it is often valuable to consider quantities derived from the reconstructed 2-D emission profiles rather than the profiles themselves. Some such derived quantities and their role in objective information are discussed.

IV.H.1. Phantom Simulations

Phantom simulations with a realistic noise level are a very important tool for establishing the reliability of

reconstructed emission profiles with respect to typical emission profiles expected, e.g., from plasma modeling codes. Additionally, they are important to ensure the algorithm is working properly, to select appropriate algorithms (Fig. 15), and to optimize parameters in the algorithm for the expected emission profiles. Furthermore, they can help in designing the layout of tomography diagnostics.

In Sec. IV.D.2, approaches were described for the optimization of lines of sight based on experience. It is worthwhile to verify the optimization with phantom simulations with realistic phantoms (showing the features one would like to be able to resolve), noise levels, perturbations, and uncertainties in alignment and geometry. A quantitative analysis could include the verification of derived quantities described below. Some fine-tuning of lines of sight may be the result of such an analysis. Phantom simulations can give a good insight into what the diagnostic is capable of and help in selecting appropriate tomography methods and parameters. The finding in Fig. 15 that the choice of best-performing depends on the phantom illustrates the importance of carrying out phantom simulations. Given the generally sparse coverage of tomography systems on MFE devices, the spatial resolution obtained is often lower than expected for a large number of lines of sight; see, for example, the limited detail reconstructed in Fig. 16 (Ref. 202). However, one has to realize that to improve spatial resolution by a factor of 2, the number of lines of sight should roughly be quadrupled, for example, by doubling the number of viewing directions and doubling the number of channels of

each viewing direction. Furthermore, increasing the number of lines of sight is only meaningful for measurements with very low noise, as the high noise level often encountered in a tokamak environment may be the limiting factor. However, as long as one is well aware of these limitations, tomography can still provide a wealth of quantitative information about emission profiles.

IV.H.2. Derived Quantities

Figure 17 shows an example of bolometer tomography on ASDEX-Upgrade in which more detail could be achieved than in an equivalent example on JET (Fig. 16) by artificially increasing the number of lines of sight by moving the plasma rigidly and using several time slices in the same reconstruction (see also Sec. IV.I.3). This experimental result resolved the same detailed structures as predicted by modeling[203–205] and illustrates the practice of comparing 2-D reconstructed profiles and code modeling results. However, it is not trivial to compare a 2-D profile quantitatively with other cases and with modeling results. In bolometry there is some use in direct comparison of 2-D emission profiles in the divertor with modeling results (as illustrated with Figs. 16 and 17) and in SXR with MHD modeling. Spatial resolution is not well defined for 2-D emission profiles and is not necessarily related to the distance between lines of sight.[206]

For quantitative comparison it is often of benefit to calculate certain derived quantities. Examples of such derived quantities that have proven useful in practice for SXR profiles are cross sections and the flux-surface
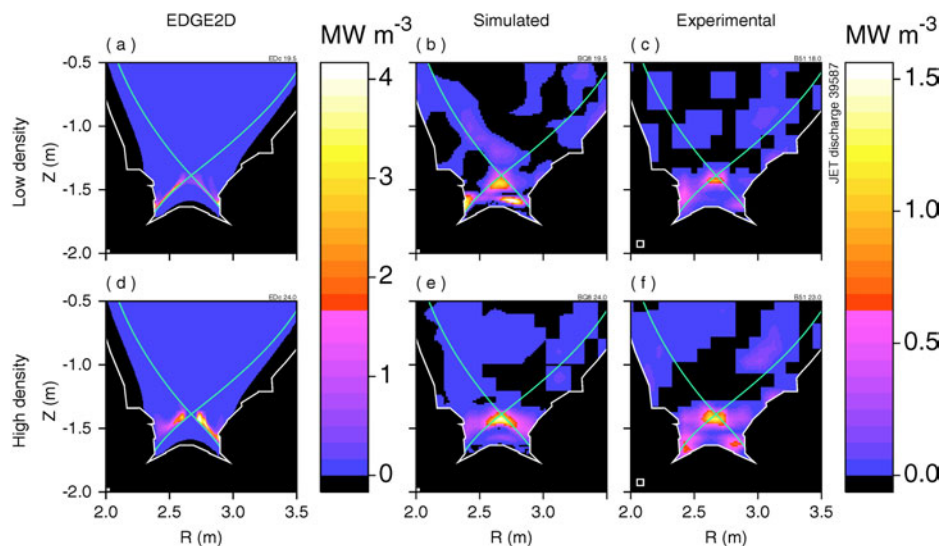
Fig. 16.   Total radiation profile in the JET MkIIA divertor at a low density (attached plasma; upper row) and high density (detached plasma; lower row) during a density ramp in the same discharge (JET discharge #39587) (Ref. 202). (a) and (e) Modeling prediction (EDGE2D-NIMBUS code). (b) and (d) Phantom simulation using the modeling prediction as input. (c) and (f) Tomographic reconstruction of the experimental bolometer data (taking into account a CX-neutral contribution; see Fig. 22). Note that even with more than 100 lines of sight, the spatial resolution that can be reconstructed is very limited.
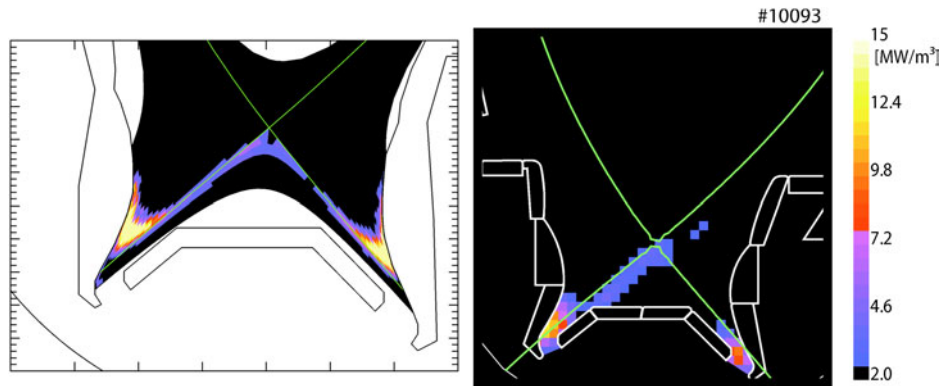
Fig. 17. Comparison of the emission profile in the ASDEX-Upgrade divertor modeled (left) and obtained by tomographic reconstruction (right), making use of a rigid movement of the divertor plasma.[203–205] (*Adapted figure reprinted with permission from Ref. 204, and from Ref. 205; Copyright 2001, Elsevier.*)

averaged emissivity.[56] For bolometry, scalar quantities are, for example, the total radiated power, the power radiated within the separatrix, and the power radiated below the X-point. Useful 1-D quantities include cross sections, flux-surface averages, and the wall-loading profile.[91,207] Projection moments, as introduced in Sec. IV.D.1, may also be useful derived quantities. Gradients make some quantities unreliable in certain areas, in particular, in the edge of plasma and the X-point. Such quantities provide physically meaningful information that allows a direct comparison with modeling or are even used as input in modeling codes. Special derived quantities from SXR tomographic reconstruction have been used to differentiate between sawtooth models.[187] An example of derived quantities is given in Fig. 19a.

IV.H.3. Toward Objective Information

The finding in Fig. 15 that the conclusions on performance of tomography methods depend on the details of the phantom suggests that regularization methods should not be compared in phantom simulations to select a single "best" method,[23,27,186] but this information should rather be used to establish how reliable the information on features of the reconstructed emission profiles is. Different methods may yield different reliable information.[150,191] Similarly, varying reconstruction parameters within a tomography method, rather than selecting a "best" set of parameters, may also yield useful information. It should therefore be encouraged to use different tomography methods and variation of the input parameters.

The zero and 1-D derived quantities introduced above also make it possible to establish error bars that indicate the certainty of the tomographic reconstructions. Error bars can be derived by comparing different suitable tomography methods and using reconstruction parameters within reasonable ranges. This provides objective infor-

mation and can give certainty on the reliability of the reconstructed emission profiles, avoiding the often heard criticism that tomography is not objective because it depends on arbitrary choices and personal preferences.

Figures 18 and 19 illustrate the use of SXR tomography for impurity-transport analysis on JET (Ref. 56). The background-subtracted tomographic reconstructions for some time slices after injection of a trace impurity (nickel) by laser ablation are shown in Fig. 18. The relevant derived quantity that can be compared with transport modeling in this case is the flux-surface averaged emission (Fig. 19), for which error bars have been established by the method described above. The 2-D reconstructions shown (Fig. 18) are the ones that seem most likely with rather subjective criteria (such as the expectation of smoothness on flux surfaces and low level of artifacts), whereas the 1-D profiles with error bars provide quantitative objective information. The use of SXR tomography for plasma transport analysis is placed into context in Sec. V.A.

The above method is rather ad hoc in how the error bars are derived. Statistical and information theoretical methods exist to derive the reliability in a more developed mathematical formalism,[144,148,167,168] for example, in the case of the maximum entropy method or with Bayesian approaches. This area is, however, not well developed in the field of MFE diagnostics and would benefit from further exploration.

The use of linearized minimum Fisher information in the objective functional as described in Sec. IV.F.3 will enhance the peaks in the emission profile in a mathematically robust way, without certainty, however, whether the peaks in the solution are overestimated or underestimated. Phantom simulations show that with Fisher information the peaks in the emission profile may actually be overestimated (i.e., higher in the reconstruction than in the phantom). This means that the objectivity of the information is lost. With the other regularization one can at
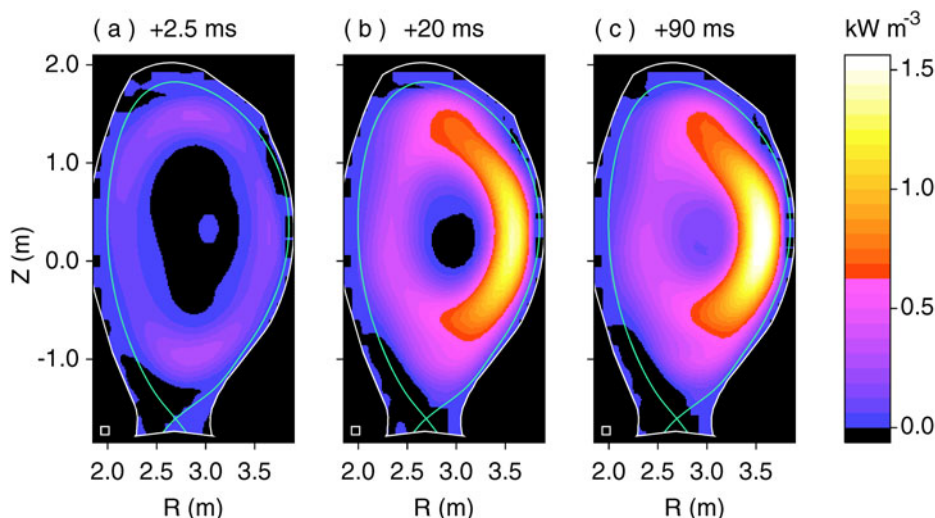
Fig. 18. Background-subtracted SXR emission in a poloidal cross section of JET for three time slices after injection of a trace impurity (nickel) into an ELM-free hot-ion H-mode (JET discharge #34476) (Ref. 56). The square in the lower-left corner indicates the grid size, and the curve indicates the separatrix. (*Figure reprinted with permission from Ref. 56.*)

least be certain that the reconstruction will be over-smoothed and, therefore, set a reliable lower limit to the peak in the emission profile. One may therefore prefer certainty that the peaks have been smoothed (by not applying linearized minimum Fisher information) than uncertainty over something that may be closer to reality (as could be the case when applying linearized minimum Fisher information).

IV.I. Miscellaneous Topics

There are several variations and extensions to the purely 2-D tomography described above that are useful for application in MFE diagnostics. The miscellaneous topics discussed next are Abel inversion, 3-D tomography and tomography of a tangential view, using temporal information in 2-D reconstructions, using vector tomography for MFE diagnostics, and specific topics related to bolometer tomography.

IV.I.1. Abel Inversion

In some cases only one view with multiple lines of sight is available. When symmetry is present in the emission profile, the 1-D profile can be reconstructed. In circular symmetry (such as a cross section of a cylinder or torus), the measurement along lines of sight is described by the so-called Abel transform. Similar to the Radon inversion formula mentioned in Sec. IV.C, an analytical inversion formula is known,[47,208] but because of a singularity and derivative, direct numerical implementation is difficult. The application of the FBP method [Eqs. (6) and (7)], taking into account symmetry in $f(p)$ (additionally, the origin must be chosen such that this is an even

function), is numerically robust and reasonably efficient (although despite the symmetry double integrals are still needed). In another robust method, a fit (i.e., series expansion) is made to the function $f(p)$ by, for example, a polynomial, for which the exact Abel inverse is known (see Ref. 209 for Abel transform pairs).

In the case of symmetry other than circular, for example, when it is expected that the emissivity is constant on noncircular flux surfaces, the problem is similar in character to that of the Abel inverse and is often referred to as Abel inversion. For general flux surfaces, it is possible to discretize the problem by series expansion similar to Eq. (10), in which beam widths can also be taken into account. If the number of basis functions is chosen to equal the number of measurements, the resulting Eq. (11) contains a matrix K that typically is triangular. Mathematically, this could be inverted analytically (this corresponds to a method that is also referred to as "onion peeling"), which seems the most straightforward solution technique. Although this method may give adequate reconstructions of the edge, in unaltered form it is not regularized, and noise on the measurements will amplify reconstruction errors toward the center of the plasma. Although this method has often been applied, and a large variety of ways have been implemented to cope with the intrinsic instability, it is not a recommended method given the many excellent alternatives. Most of the regularization techniques described in Sec. IV.F can easily be adapted to the 1-D case.

There are two aspects of Abel inversion that make it more problematic than 2-D reconstruction. First, any reconstructed profile from Abel inversion depends critically on the radius at which the measurement is assumed
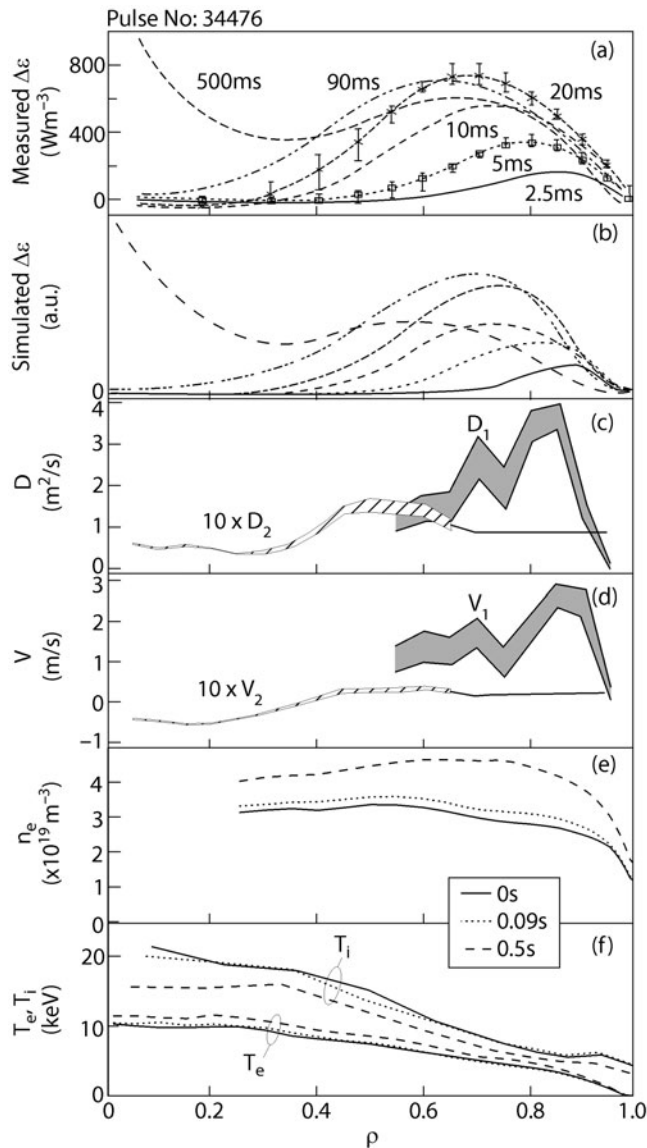
Fig. 19. (a) Background-subtracted flux-surface averaged emissivity $\Delta\varepsilon$ from the tomographic reconstructions of Fig. 18 and other time slices as a function of normalized minor radius ρ. (b) The simulated emissivity for the same plasma using a transport code that includes a collisional-radiative model.[56] (c) and (d) The derived radial profile of the diffusion coefficient D and convection velocity V. The hatched and gray areas indicate the region og uncertainty from the assessment. (e) and (f) Electron density and electron and ion temperature profiles. Times are given with respect to the time of nickel injection. (*Figure reprinted with permission from Ref. 56.*)

to go to zero. In 2-D tomography, the possible emission profiles are constrained by measurements at different angles. With line-of-sight measurements from only one direction, the constraint has to be supplied, for example, by

zero measurements (i.e., lines of sight measuring outside the plasma) or in the form of a priori information, with the reconstruction quality depending on the accuracy of the a priori information. In general, it is therefore sensible to include a few lines of sight viewing outside the emitting part of the plasma in the design of Abel systems, as these may provide more crucial information than a measurement inside the plasma. Second, Abel inversion will generally give emission profiles that look reasonable, even if the assumption about constant emissivity on flux surfaces is violated (only if it is violated significantly, it may be obvious from unphysical reconstructed profiles, such as negative emissivity in regions of the plasma). Unless there is a view of the plasma at a different angle to compare with, it may be impossible to ascertain whether the assumption of emissivity constant on flux surfaces is valid. This uncertainty clearly reduces the value of the diagnostic data and is a strong argument for measurements at several angles and 2-D tomography. Despite these arguments against Abel inversion, it should be realized that Abel inversion of the emissivity of the edge plasma may provide more accurate results (locally) than possible with 2-D tomography (because of too few views). However, it is always useful, and often essential, to have an additional view of the plasma to verify that the assumptions made are valid.

IV.I.2. Three-Dimensional Tomography and Two-Dimensional Tomography of a Tangential View

With the start of the use of 2-D detector arrays as MFE diagnostics, such as charge-coupled-device (CCD) cameras in the visible and ultraviolet range, various 2-D X-ray detector types, and imaging bolometers, a large number of line-integral measurements become available. With several such cameras, it would in principle become possible to make 3-D tomographic reconstructions. Three-dimensional tomography is a straightforward extension of the 2-D Radon transform, with similar reconstruction algorithms, although technically 3-D tomography of line-integral measurements is called the X-ray transform rather than 3-D Radon transform (n-dimensional Radon transform is for measurements over a dimension $n-1$, i.e., planes in the case of $n=3$) (Refs. 130 and 132). Truly 3-D tomography has hardly been applied to MFE diagnostics because as for 2-D tomography discussed in Sec. IV.D, it is very important that multiple views (i.e., lines of sight from several directions) cover every part of the reconstruction volume and that there are no emitting plasma regions seen by the views that are outside the reconstruction volume. To obtain sufficient experimental data to be able to make reconstructions with limited a priori information, very many views are needed (possibly from tens of directions or more around the entire MFE device, not just two cameras). This is very difficult to fulfill on most MFE devices because access is usually

restricted to a few ports. If assumptions can be made about toroidal symmetry of plasma emission, it is possible to relax the requirement of full multiple coverage and on the number of views dramatically: One view may be sufficient. The local basis functions and regularization methods of Secs. IV.E and IV.F can easily be adapted for 3-D tomography, and assumptions about symmetry and other a priori information can be included in the objective functionals. However, as the computation time depends strongly on the number of basis functions or grid points, it is generally more effective to use the 2-D tomography methods for tangential views.

If it is known that the emissivity of the plasma is symmetric in the toroidal direction, the 3-D nature of lines of sight of toroidally (also referred to as tangentially) viewing 2-D cameras can be reduced to a 2-D tomography problem, and the same methods as described in Secs. IV.E and IV.F can be used, with the geometric matrix properly describing the line integrals. Projection of the lines of sight on the poloidal cross section is a convenient way to assess the coverage. Note however that in the geometric matrix, the actual length of the lines of sight in three dimensions is used, not the length of the projected line of sight on a poloidal cross section. Typical coverages obtainable in a tokamak, when the emissivity can be assumed not to change in the toroidal direction, are illustrated in Fig. 20. Reasonable coverage can be obtained in many locations, albeit the coverage is irregular and in some regions lines of sight from certain local directions may be missing (which may lead to artifacts in the reconstructions unless appropriate a priori information is taken into account). The symmetry conditions that allow tangential tomography may be that every poloidal cross section of the plasma emissivity is identical (e.g., visible and ultraviolet regions) or, for example, helical symmetry along field lines (e.g., structures related to MHD events). After early successful applications of visible CCD cameras,[210–213] usually with filters to measure line radiation from deuterium and particular ionization stages of impurities, the diagnostic technique is now in common use on MFE experiments and has been extended to the vacuum ultraviolet range.[214] The reconstructed emission profiles are usually compared with the predicted profiles from 2-D modeling of the divertor plasma.[215] Tangential tomography has also been proposed for 2-D X-ray measurements (e.g., Refs. 145, 216, and 217 and other MFE devices), especially for MHD analysis.

The standard series-expansion tomography methods, usually on a regular grid, can be applied to tangential tomography. Methods that have been applied are TSVD (Ref. 213) without a priori information (apart from truncation level), other standard inversion algorithms,[218] and ART (Ref. 145). Also, the other regularization methods of Sec IV.F can be used,[126] and the associated a priori information may have benefits in avoiding artifacts due
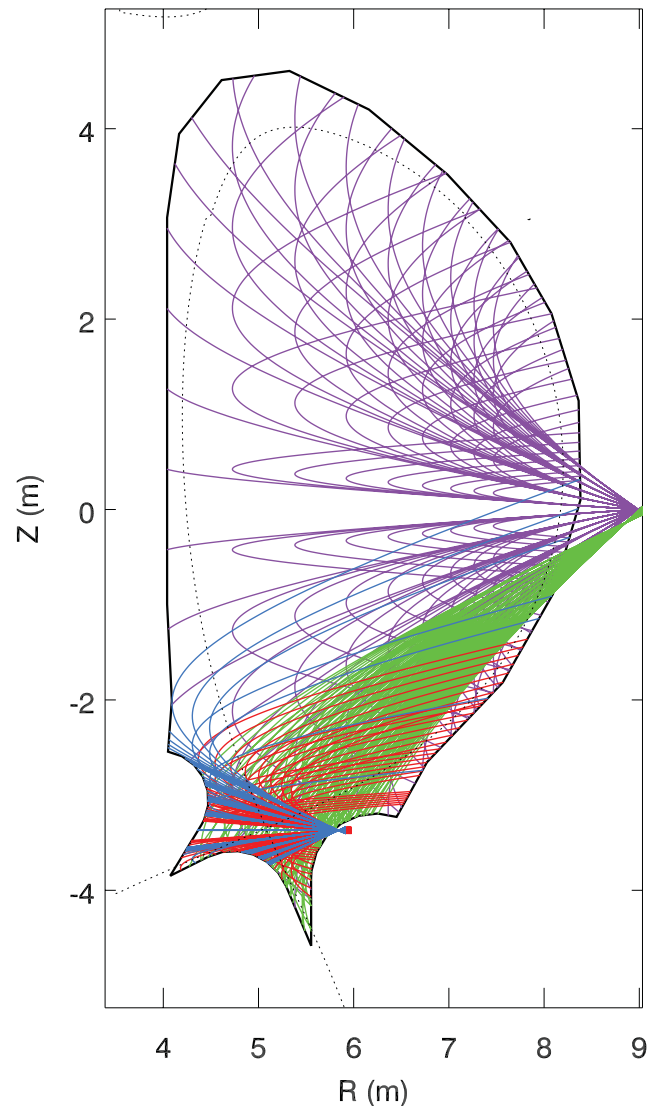
Fig. 20. Illustration of the projections on a poloidal cross section, assuming toroidal symmetry, of four different tangential views with a 2-D camera (equatorial port horizontal, equatorial port toward divertor, and two horizontal views from the divertor) in a study of the implementation of an imaging bolometer camera on ITER (Ref. 93).

to the incomplete coverage (i.e., each point is usually not covered from all angles, as is evident from Fig. 20). Although the numerical implementation is not difficult, there are some aspects that make tangential tomography far more difficult in practice than ordinary 2-D tomography. The geometry is far more sensitive to misalignments (i.e., that the geometry used in the reconstructions does not correspond to reality) than 2-D tomography, and the assumptions on toroidal symmetry often break down. In most applications of tangential tomography, a significant effort is put into determining the actual

viewing geometry after installation of the camera, both determining the hardware alignment, and subsequently by software tools.[218] Even an uncertainty in camera location of only one camera pixel in one direction can create large artifacts in the reconstructions because the assumed projected line of sight on the poloidal cross section is already significantly different from reality (see Fig. 20). Toroidal asymmetries also often occur in reality, which are difficult to handle and will degrade the tomographic reconstructions. These difficulties can often be overcome, and tangential tomography in the visible and ultraviolet range has become a powerful routine diagnostic. Tomographic reconstruction of a semitangentially viewing imaging bolometer has also been obtained.[126] To study MHD activity with 2-D X-ray cameras is more ambitious than the applications with toroidal symmetry, however, as the helical structure of the field lines must be taken into account in the tomographic reconstructions, which may require more accurate equilibrium reconstructions than are usually available, and also knowledge of field ripples and other perturbing effects. These difficulties can be overcome, however.[217] They result from the need to use the symmetry assumptions in the geometric function of the lines of sight and may, despite lengthy computation times, justify a reconsideration of 3-D tomography with the symmetry assumptions implemented as a priori information in the objective functional since this would give more flexibility to cope with violations of the assumptions.

IV.I.3. Using Temporal Information to Improve the Output from Tomographic Reconstructions

In the 2-D tomography discussed so far, data are processed only from individual time slices. Especially when only views from one or two directions were available in SXR tomography systems on MFE devices, attempts were made to increase the achievable resolution, e.g., the angular harmonics in the Cormack method, by taking into account temporal information. Subsequent time slices of a circular plasma (or an approximately elliptical plasma transformed to circular) in which features can be assumed to rotate rigidly poloidally, for example, due to actual toroidal rotation of the plasma, can be interpreted as additional views at different angles. This has been exploited to study MHD phenomena,[188] such as islands[11] and snakes.[219]

In a similar way, the number of lines of sight can be increased artificially in bolometer tomography by rigidly moving the plasma vertically. As shown in Fig. 17, this has allowed the resolution of radiative features similar to those predicted by modeling,[204] which could not be resolved when considering single time slices because of the limited number of lines of sight.[203,205,220]

Although very interesting results have been obtained by artificially increasing the number of views by taking into account several time slices, the application of the method requires the assumption of rigid movement, which is often violated. It is therefore not a technique used routinely.

Artificially increasing the number of views is not the only way to take into account temporal information in the tomographic reconstructions. At great computational expense, one could introduce time as a third dimension in the discretization Eq. (10) and obtain a smooth transition between time slices of the reconstructed emission profile by an appropriately chosen objective functional. In fact, this has been applied by deciding on the reliability of Cormack expansion coefficients on the basis of a statistical analysis of their time dependence.[171,221]

Another method for taking into account temporal information is biorthogonal decomposition.[222–224] To apply this method to tomography,[23] the 2-D reconstructions on a regular grid for a given number of time slices are put in a matrix with each row being a time series. The SVD of this matrix results in three matrices, the columns of one of which contain orthogonal "spatial eigenvectors" (often referred to as "topos") and the columns of another of which contain orthogonal "temporal eigenvectors" (often referred to as "chronos"). The third matrix contains the singular values, the magnitude of which is a measure of the significance of each eigenvector pair. Large values correspond to pairs that contain the most significant spatial and temporal information, whereas the components with the smallest singular values merely contain noise. By considering components separately, certain spatial and temporal characteristics of data may be isolated. However, as this is a purely mathematical method, physical information may well be scattered over several components. By discarding components with the largest singular values (which are likely to contain the information about the average emissivity) and components with small singular values (noise and artifacts of the reconstruction), it is possible to effectively filter the data and isolate features of most interest.[23] This filtering has been highly successful for visualizing MHD fluctuations, in particular, rotating island structures, in the SXR emission profile; see for example Fig. 21 (Ref. 225). Without the SVD filtering, the island structures, which only give small perturbations on the line-integral SXR signals, may be much less evident as they can be drowned in the noise and artifacts of the reconstructions due to small inconsistencies in the data. In some applications, the signals have been "SVD filtered" before the reconstruction, rather than the 2-D reconstructions.[21,189,222–224] In general, this is less successful, as features of the signals, for example, characteristics due to their line-integral nature, often are scattered over several of the topos and chronos. SVD filtering of tomographic reconstructions of several time slices therefore seems the more successful approach, and more applications are discussed in Sec. V.A.
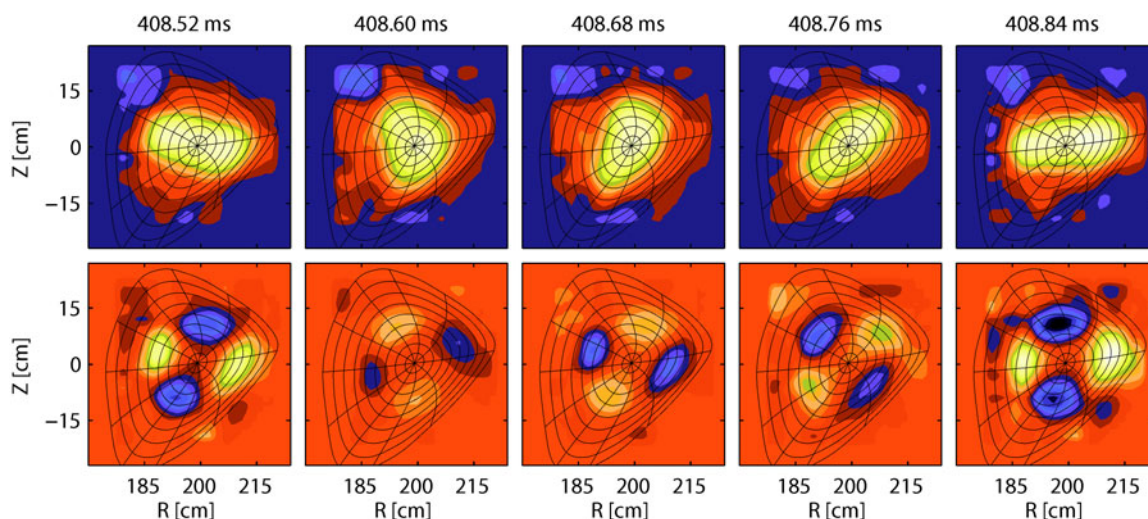
Fig. 21. Reconstructions of a number of time slices (upper row) show a variation in time of the SXR emissivity measured by the Wendelstein 7-AS stellarator ten-camera system.[225] A spatio-temporal filtering technique based on SVD (lower row) clearly resolves an *m* = 2 tearing-mode structure. (*Figure reprinted with permission from Ref. 225.*)

IV.I.4. Vector Tomography

The application of tomography discussed so far deals with the reconstruction of scalar quantities. An extension of the formalism to the reconstruction of vector fields with application in plasma diagnostics has been proposed, in particular, for the reconstruction of velocity fields from line-integral measurements.[226–229] Although spectrally resolved measurements are strictly speaking outside the scope of this chapter, it is worthwhile to briefly discuss this special application of tomography. For broadband measurements, the Doppler effects are usually negligible, and ordinary scalar tomography is possible, as long as the spectral response of all channels is the same.

Many spectroscopic measurements of MFE plasmas are local in nature because of spectral lines radiating in thin shells or local CX processes with a neutral beam. However, when the radiation is nonlocal, such as for heavy impurities, in a rotating plasma with a nonconstant ion temperature, the spectral line shape varies along the lines of sight due to the changing angle between the flow field and the line of sight (varying Doppler shift) and the variation in Doppler broadening.[230] Therefore, emission profiles cannot be reconstructed independently for each wavelength, and the special techniques from vector tomography are required[226,228] to reconstruct the scalar field (emissivity, and ion temperature) and vector field (velocity) independently from spectrally resolved measurements. It has been recognized[226,228,231] that linear equations, from which the required quantities can be solved, can be obtained by taking moments in wavelength of the (nonlinear) line integrals over the spectral line shape, after the background has been subtracted.

These moments can subsequently be reconstructed, yielding the emissivity profile, rotation velocity, and ion temperature from the zeroth, first, and second moments, respectively.

Derivation of rotation and ion-temperature profiles from broad emission profiles on present-day MFE devices, using both active and passive visible and near-ultraviolet spectroscopy, has been reported in the literature,[230–234] while a well-regularized reconstruction method has been presented and the performance assessed of derivation of poloidal and toroidal rotation from expected X-ray crystal spectroscopic signals in ITER (Ref. 235). Some of these applications are for multiple lines of sight from a single direction,[230,231,234,235] thus requiring assumptions about the quantities on flux surfaces (similar to Abel inversion). It has also been proposed to apply the technique to full tomography using data from multiple directions,[226,228] and 2-D reconstruction of the ion temperature has been demonstrated.[236] By recognizing that the local spectral emissivity in particular directions is described by the 3-D Radon transform of the velocity distribution function, i.e., integral over planes in velocity space perpendicular to the viewing directions, it should be possible to reconstruct aspects of the velocity distribution function without the assumptions usually made about flow velocities and the temperature (e.g., the latter being Maxwellian).[236]

IV.I.5. Issues Related to Bolometer Tomography

Three issues specific to bolometer tomography will be discussed here: the large difference in emission level from the bulk plasma and radiative peaks in the divertor plasmas in MFE devices with divertors, the relatively

high noise level, and the contribution of CX neutrals to the bolometer measurements.

The first issue is the large difference in emissivity level between the bulk plasma and divertor (e.g., Fig. 16). The total radiation emitted in the divertor may be similar to that of the bulk plasma, while the volume is much smaller. This leads to two problems (note that in general it is not possible to separate the reconstruction of different regions, as pointed out in Sec. IV.D). First, tomography algorithms typically have difficulties in dealing with large differences in emissivity. The absolute reconstruction accuracy in the high- and low-radiation regions is similar, which implies a low relative accuracy in the low-radiation region. Furthermore, the noisy and sparse measurements may result in a limited reconstruction accuracy of the peaks in the divertor radiation. This is amplified by the second problem, i.e., that relative noise on a line-integral measurement through the bulk plasma that also views a radiating peak in the divertor leads to a large uncertainty in the contribution from the bulk plasma. Even small inconsistencies between lines of sight viewing the peaks in the divertor will translate to very large uncertainties in the reconstruction of the bulk-plasma emission profile. It may be possible to limit the effects of these problems by specifically developed reconstruction algorithms, but these have not yet been developed. If the tomography system has been designed to have adequate coverage of the bulk plasma by lines of sight that do not see the divertor, it is possible to use these to make a tomographic reconstruction of the bulk emission profile. The contribution of this emission profile to lines of sight that do view the divertor can be subtracted from those signals, and a separate reconstruction can be made of the divertor emission profile. Phantom simulations demonstrate that this separation technique can produce accurate reconstructions of the bulk and divertor emission profiles, provided the coverage is adequate and special precautions are taken in the objective functional to ensure a smooth transition between the two reconstruction regions. Unfortunately, in many present-day bolometer systems, such as at JET, the coverage of the bulk plasma is insufficient for the separation method to work.

The relatively high noise levels and large uncertainties in bolometer measurements generally make it difficult to reconstruct very peaked emission profiles, even if the spatial resolution in principle is sufficient. This is especially the case when the discrepancy principle [Eq. (13)] is used as a constraint, which is a constraint on the discrepancy between measurements and backcalculated signals summed over the channels rather than a constraint on individual channels. Weighting the constraint by the estimated error, as described in Sec. IV.F.2, helps only partially. It is effective to artificially decrease the estimated errors of channels that see the radiative peaks, but this is not a correct procedure that furthermore risks introducing artifacts in the reconstructions if the estimated errors are too small. The use of linearized minimum Fisher information as described in Sec. IV.F.3 to avoid oversmoothing will also enhance the peaks in a mathematically robust way, however, without certainty whether the peaks in the solution are overestimated or underestimated (Sec. IV.H.3). The conclusion is that although constrained optimization with the discrepancy principle is adequate for bolometer tomography, refinements could be envisaged that deal with the above issues and could improve the capabilities. Despite this, improvements in the algorithms will have only a limited impact, and significant improvements beyond those achieved currently (e.g., Fig. 16) seem possible only if the coverage and bolometer sensitivity are improved significantly with respect to current systems.

As pointed out in Sec. IV.F.4, it is typical that negative peaks occur in reconstructions of very localized radiating peaks in the divertor when normal linear regularizarion as described in Sec. IV.F is used. Without nonnegativity constraint on the solution, phantom simulations like those in Fig. 16 (which did use the nonnegativity constraint) result in large negative peaks and the possibility that positive peaks occur even in incorrect positions. It is therefore important to impose nonnegativity on the solution (some methods are pointed out in Sec. IV.F.4).

The third issue is that of CX neutrals contributing to bolometer signals (as described in Sec. III.C.3). Charge-exchange neutrals are mainly generated in the divertor plasma. Although CX neutrals from the edge could contribute to bolometer signals, code modeling of, for example, the JET edge shows this is negligible. Experimental evidence of CX neutrals has been found from comparisons of bolometer lines of sight viewing the divertor plasma from the divertor and from the opposite direction through the bulk plasma (which shields those channels against the neutrals and the plasma is optically thick for low-energy neutrals)[237] and from comparison of AXUVDs and metal absorber bolometers.[70,71] Provided the coverage of the divertor from both bolometers mounted around the divertor and viewing the divertor through the bulk plasma constrains the measurement sufficiently, it is possible to derive the CX-neutral contribution to divertor channels from tomographic reconstructions. Instead of the CX neutrals being a liability to bolometer measurements, it is an opportunity to derive information on the power carried from the plasma by CX neutrals at the same time as the emission profile. Derivation can be achieved by adding the CX-neutral contribution to each signal as unknowns to Eq. (11) and penalizing a high level of neutrals in the objective functional.[238] By appropriate choice of the regularization parameter, from phantom simulations or by requiring a positive emission profile with least oversmoothing, an estimate of the CX neutrals to the divertor bolometer signals can be obtained. A result of the derivation of the CX-neutral level in this way for the experimental data shown in Fig. 16 is illustrated

in Fig. 22 with code modeling results for comparison.[202] The comparison with code modeling is reasonable.[202,220,238] It was also found experimentally and from modeling that for helium plasmas on JET, the CX-neutral contribution is negligible. Although these results show that the CX-neutral contribution can be derived from bolometer measurements if the viewing geometry is adequate, because of the discrete spacing of bolometer channels it is not possible to derive the total power lost from the plasma by neutrals as a full space/angle coverage of the plasma edge by bolometers would be required; however, the code modeling, compared with measurements of CX-neutral losses in a few

locations, can provide estimates of the total power loss by neutrals.

IV.J. Summary

Various algorithms that are well suited for application to MFE tomography diagnostics and considerations that need to be taken into account when applying them have been described. Methods we here refer to as constrained optimization with local basis functions now rank as the most widely applied in MFE tomography diagnostics.[5,23,38,42,56,143,144,147–151] The reasons are the generally good performance, the flexibility to cope with the peculiarities of MFE diagnostics, and the acceptable computation times on modern computers. These methods include the maximum entropy approach, and linear approaches that typically include some form of smoothness in the objective functional. However, the details of the choices made in the implementation—basis functions, objective functional (Sec. IV.F.3), and criterion for finding the regularization parameter (Sec. IV.F.2)—depend on personal preferences of the implementer (as described in Sec. IV.F.4). In our experience requiring smoothness on flux surfaces and the discrepancy principle provide very satisfactory results for both bolometer and SXR tomography. The detailed choices are probably not very important, and it may be of benefit to compare several tomography methods, as described below in relation to objective information.

Although the use of tomography is routine, the quality and the nature of the measurements, such as the limited coverage and unreliability of measurements due to drift, radiation damage, or changing calibration factors, usually make it necessary to manually assess signals and the reconstructions of each time slice or to vary reconstruction parameters to establish the reliability of the reconstructions. Automation is therefore only possible to a limited extent. It also means that for the actual development of tomography codes for MFE diagnostics, most effort does not go into the development of the tomography algorithm but in the required tools for preprocessing and postprocessing of signals and reconstruction results. In some cases, routine automatic tomographic reconstructions are made of many time slices. This usually provides less reliable data, which however can be useful to identify the most interesting events in plasma for subsequent detailed analysis.

A number of important general conclusions can be drawn from the description of tomography methods in this section. First, by well-established and easily implemented methods for mathematical regularization, it is possible to deal effectively with high spatial-frequency noise but is impossible to deal with low spatial frequency noise, which therefore has to be avoided by careful design of the system. Second, the number of basis functions, in particular, grid points if local basis functions are used, is a valuable parameter. As described in Sec. IV.E,
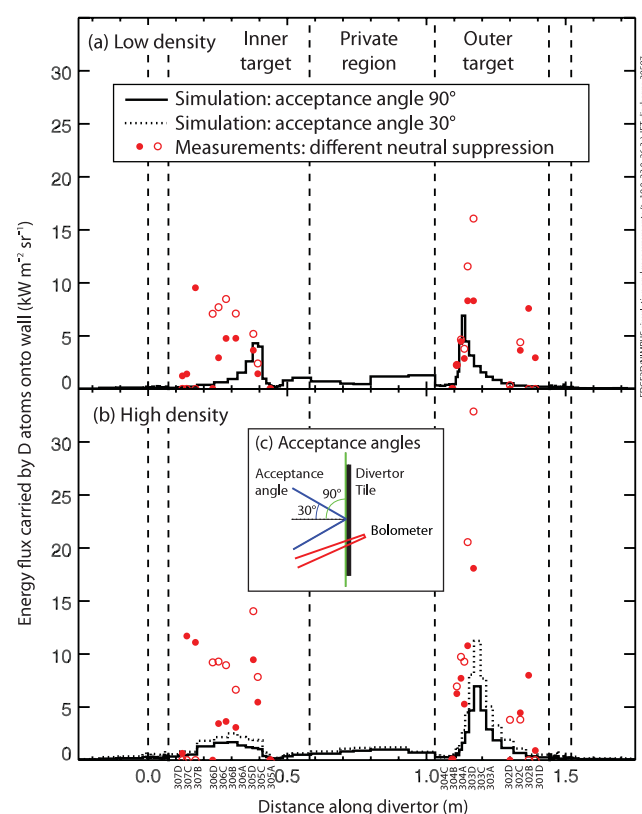

Fig. 22. Charge-exchange-neutral power load on the JET divertor targets derived from the bolometer tomography (points), compared with modeling with the EDGE2D-NIMBUS code (lines)[202] for the same (a) low-density plasma and (b) high-density plasma as assessed in Fig. 16 (JET discharge #39587). The modeling code could only provide data for neutrals impinging on the surface within a certain cone perpendicular to the surface, not the actual viewing cone of the bolometers [see insert (c)]. The variation of the acceptance cone illustrates that the neutrals are not uniformly distributed over the angle of incidence and that for the actual small acceptance angles of the bolometers, modeling results could well be more consistent with the experimentally derived values.

choosing the number such that Eq. (11) is underdetermined has many advantages if a priori information is used effectively. Third, for the physicist the reliability and the objectivity of the information in tomographic reconstructions are of paramount importance.

Reliability is assessed by phantom simulations, which give insight into the limitations in the quality of the reconstructions and help optimize reconstruction parameters. From the example of Fig. 16, it is clear that even with a comprehensive bolometer tomography system such as that on JET, the obtainable resolution of radiating features is often limited because of the small number of lines of sight and noise and uncertainties on the measurements. Improved information is possible through techniques for special cases, such as that applied for Fig. 17. Varying reconstruction parameters and comparing different tomography methods may be useful to gain insight into the reliability and objectivity of features appearing in the reconstructions. This is illustrated to some extent by how the error bars of Fig. 19a were obtained. Comparisons of tomography methods, as exemplified in Fig. 15, have often been made.[23,27,150,186,191] However, it could be of more concern to the physicist to determine objective information by considering ranges of reconstruction parameters and different tomography methods than the details of an actual optimized actual choice of a priori information and of a reconstruction method from the many good ones available. Methods to establish the objectivity of tomographic data need to be developed further; see Sec. IV.H.3.

It is not expected that major developments will be needed on new tomography algorithms nor that advances can be made that would dramatically improve the capability to deal with irregularly and sparsely sampled and noise data, as it occurs in MFE diagnostics. However, it is likely that advances can be made by adaptations of existing algorithms. Particular needs for further development are the following. As discussed in Sec. IV.I.5, bolometer tomography in MFE devices with divertors has to deal with very large differences in radiation level between bulk and divertor plasmas, which makes it very difficult to accurately reconstruct the bulk-plasma emissivity. In addition to adequately distributing lines of sight of the system to at least be able to separate the reconstructions partially, it may also be of benefit to explore new algorithms that could deal effectively with the large differences in emissivity levels. For potentially optically thick plasma regions in the BPX divertor, it may also be necessary to develop or adapt algorithms. Advances may also be made by more effectively making use of temporal information in the tomographic reconstructions (rather than postprocessing as used, for example, for Fig. 21) and by combining cross-correlation techniques of 2-D multichannel line-integral measurements with 2-D reconstruction and visualization. Further development of the techniques to derive objective information would be of benefit (see Sec. IV.H.3).

V. EXAMPLES OF THE USES OF THE DIAGNOSTICS

A number of representative examples of results that can be obtained with SXR and bolometer MFE diagnostics have been given in the previous sections, for example, to illustrate a particular aspect of a tomography method. In this section, the plasma physics aspects of some of the examples, in particular, those related to the quantities listed in Table I, will be given in more detail, and the results will be placed into context. In addition, a few other applications of SXR and bolometer diagnostics will be mentioned.

As pointed out earlier, similar mathematical reconstruction techniques are also applicable to other MFE diagnostics, such as interferometry and reflectometry, spectrally resolved spatial measurements (see Sec. IV.I.4), and deconvolution, for example, of instrument functions such as measurements with compact neutron spectrometers.[239] These are outside the scope of this chapter, however.

V.A. SXR

Figures 2 and 3 illustrate the use of line-integral (i.e., uninverted) SXR measurements in the characterization of events such as sawteeth and snakes. Analysis of MHD activity in the form of islands is also common. Comparison of uninverted SXR signals with modeling of MHD mode activity has yielded important confirmation about the plasma physics.[240–242] SVD filtering (biorthogonal decomposition) has both been applied to uninverted and tomographically reconstructed SXR data, as described in Sec. IV.I.3. Other techniques of analysis of, in particular, the temporal behavior of uninverted SXR data are Fourier[243] and wavelet analysis.

SVD filtering of tomographic reconstructions for the study of magnetic islands, as pioneered in Ref. 23 and illustrated for MHD islands by Fig. 21 (Ref. 225), has subsequently been applied to a range of MHD instabilities, such as global Alfvén eigenmodes, and the reconstructed spatial structure is typically compared with that predicted by modeling.[244,245] The spatial structure of MHD activity has also been studied with other, specifically developed tomography approaches,[154,155] including the use of temporal information as described in Sec. IV.I.3 (Refs. 11 and 188). The physics of sawteeth, using SXR tomography, has been studied in, for example, Refs. 187, 246, 247, and 248, while snakes were discovered and were described both from SXR tomography and uninverted SXR signals.[219,249,250] Other uses of SXR measurements and SXR tomography include plasma transport studies (see below), the study of pellet-enhanced performance modes[251] and disruptions,[252] and the determination of light impurity densities and Z_{eff} (Ref. 253), and T_e profiles.[49]

Figures 18 and 19 illustrate the use of SXR tomography for the study of particle transport in tokamak

plasmas using the injection of trace heavy impurities and the method that has often been used.[56,254–259] One-dimensional transport modeling is used to derive the diffusion coefficient and convection velocity (Fig. 19). When comparing SXR data with transport modeling, it is sensible to compare reconstructed emission profiles rather than simulated SXR line integrals, as the former is more sensitive to variations and all knowledge of the SXR system can be used to obtain reliable emission profiles. In a similar way to the study of particle transport, SXR diagnostics are used extensively for the study of heat transport (such as cold pulses and power modulation); see, for example, Ref. 260.

Figure 18 (Ref. 56) shows a very significant poloidal asymmetry. Such an asymmetry had been observed a number of times earlier[261–263] and can very well be explained by heavy impurities experiencing a redistribution of flux surfaces due to the centrifugal force of the toroidally rotating plasma.[262,264,265] Also, poloidal asymmetries with the peak on the inboard side have been observed during radio-frequency heating of the plasma.[174] In other conditions it has been established that the SXR emission contours do not completely coincide with the flux surfaces.[266] Despite these cases of the SXR emissivity not being constant on flux surfaces, in general the quantities are sufficiently linked that the SXR profile can be used for plasma position control as a backup for control on magnetics signals, for example, the vertical position control on the peak of the line-integral SXR profile (using two cameras separated toroidally by 180 deg to remove contributions from $n = 1$ mode oscillations)[267] or control on the center of gravity of the SXR profile from real-time tomography.[62]

V.B. Bolometry

Probably the most important parameter determined by bolometers is the total radiated power, which is needed to understand the power balance of the plasma, i.e., power input versus power losses, in particular, in highly radiative plasmas.[85,91,205,207] The radiated power in the divertor and the radiative power load on the wall are also relevant quantities for the power balance studies. Divertor-operation relevant phenomena that can be studied with bolometers are summarized in Ref. 37. Highly radiative plasmas ("radiative divertor" operation), to reduce the power flux to the strike points and reduce ELMs, may play an important role in BPX and are obtained routinely in existing tokamaks[91,205,268–270] with or without impurity seeding. Also, feedback on the radiation level in such discharges has been demonstrated in JET, DIII-D (Ref. 270), ASDEX-Upgrade (Ref. 271), and JT-60U (Ref. 272). In such cases the total radiated power needs to be derived in real time, for example, by simple formulas, statistical methods,[271] or neural networks.[273]

The examples of bolometer tomography given in Figs. 16 and 17 illustrate its role in the characterization of divertor radiation and detachment, which has been used extensively on many machines; see, for example, Refs. 268 and 274. Typically, the 2-D emission profiles derived are compared with code modeling to confirm the physics understanding obtained from the modeling.[204,269,275] Radiation magnitude and distribution were an important factor in characterizing divertor detachment in high power-density plasmas[276] and in illustrating the role of convective parallel energy transport in producing a distributed radiation pattern in a radiative divertor.[277,278] Additionally, derived quantities are used as input data for modeling codes.

Under favorable circumstances, it is possible to analyze accurately the energy received by bolometers integrated over events much faster than the time response of the bolometers. The radiation pattern of Type-I ELMs has been reconstructed in ASDEX-Upgrade,[279] contributing to the understanding of the dynamics and power balance of Type-I ELMs. The radiated energy has similarly been analyzed for disruptions in JET (Ref. 280) and DIII-D.

Information about the CX neutrals escaping from the divertor plasma can also be characterized with metal-absorber bolometers, as illustrated in Fig. 22 (Refs. 202, 220, and 238). The 2-D line-integral measurements from imaging bolometers also help in the localization of radiative features, as illustrated in Fig. 8 (Ref. 123), and tomographic reconstruction by techniques as described in Sec. IV.I.2 have been obtained[126] to quantify the emission profiles.

VI. CONCLUSIONS AND PROSPECTS FOR FUTURE DEVELOPMENT AND APPLICABILITY TO BPX

After initial application of single SXR detectors and bolometers to early MFE experiments, a development took place via one or two fans of detectors viewing the plasma through vacuum vessel ports to large numbers of fans of miniature detector arrays mounted in-vessel. The latter have greatly enhanced the value of the SXR and bolometer diagnostics. Such tomography systems have become a standard on most major and many smaller MFE devices. Although manual intervention is usually required and tomographic reconstructions are in most cases not made automatically of every time slice of every discharge because of the complexities in the analysis described in Sec. IV.J, careful manual analysis of the emissivity during interesting plasma events provides very valuable data on the plasma parameters listed in Table I. Despite the advances made over recent decades and the wide use of the tomography diagnostics on MFE devices, their application remains a challenge: Given that the plasma is generally not stationary, many fast detectors and electronics units are needed, which makes the diagnostics costly, and the detectors have to survive and function reliably in a hostile and often inaccessible environment with relatively high levels of noise and interference.

Several quantities that have proven use in physics analyses, derived from the reconstructed 2-D emission profiles, were introduced in Sec. IV.H.2, and it was argued that these are more adequate to describe objective information than the 2-D emission profile. It may seem a luxury that a comprehensive 2-D system is needed to obtain the most valuable quantitative information: 1-D and scalar quantities. However, experience shows that derivation of most of these quantities is most reliably done from accurate 2-D emission profiles rather than from Abel inversions from single fans or from single detectors. A possible exception is the total radiated power, which can reliably be obtained from a single view, and also Abel inversion of the emission profile at the edge. It can also be pointed out that despite the large number of channels, the spatial features that can be resolved are often limited. This is especially true for bolometer tomography (see Fig. 16) but also for SXR tomography: Special techniques are required to be able to reliably extract details of the emission profile such as MHD activity (see Fig. 21).

As discussed in Sec. IV, standard algorithms and techniques have been developed that are well adapted to tomographic reconstruction of data from multiple line-of-sight MFE diagnostics. It is therefore not expected that major developments will be needed on new tomography algorithms nor that advances can be made that would dramatically improve the capability to deal with irregularly and sparsely sampled noisy data, as occur in MFE diagnostics. However, it is likely that advances can be made by adaptations of existing algorithms; particular needs for further development were discussed in Sec. IV.J.

The most widely applied sensors today, semiconductor photodiodes for SXR and ultraviolet and metal-resistor bolometers on Kapton® or mica foils, are not likely to be sufficiently radiation hard for BPX, at least not for application inside the vacuum vessel. In the descriptions of individual sensor types in Sec. III, the prospects of the development of radiation-hard sensors have been discussed. For SXR detection, there is the prospect of the development of VP detectors, although questions remain over their sensitivity and spectral response. New, reasonably radiation hard SXR detector arrays may also offer prospects if they can be sufficiently shielded. For bolometers, advances have been made on resistive bolometers on ceramic substrates, which also are likely to offer a slightly higher sensitivity than existing resistive bolometers. Imaging bolometers and capacitive bolometers based on ferroelectric materials offer further prospects to improve the sensitivity. To improve the capability of bolometer tomography systems with respect to those commonly used on present-day MFE devices, more lines of sight will be needed, and the noise, interference, and other perturbing effects such as drift must be reduced. Because of the 2-D nature of the problem, a factor of ~4 more

lines of sight would be needed to achieve an improvement of the spatial resolution by a factor of 2. However, improvements of tomographic reconstructions are only found if the noise level is low. It is therefore necessary to increase sensitivity and to optimize cabling and earthing schemes. For ITER, a comprehensive bolometer system is planned, which has channels mounted in ports, on the vacuum vessel viewing through narrow gaps between blanket shielding modules, and in the divertor viewing through gaps between divertor tiles. Because of the uncertainties in sensor development, it is difficult to assess the likely performance of such a system and what level of redundancy will be needed. However, it is clear that the in-vessel conditions are extremely hostile, the prospects for replacing failed bolometers other than in the ports and divertor are poor, and the signal levels of channels viewing through gaps in the blanket and divertor are less than ideal. For ITER, no decision has been taken at this moment on the SXR system, for example, whether it will only consist of shielded detector fans mounted outside the vacuum vessel viewing through vacuum-vessel ports or whether there is a prospect to mount sensors in a similar way to bolometers.

For ITER, the prospects for comprehensive bolometer and SXR tomography diagnostics are therefore reasonable, despite the many technical difficulties that must be overcome. However, it is unclear whether even more radiation-hard sensors can be developed for in-vessel use in MFE reactors, given the environment and additional constraints (further shielding). Despite the likely requirements for plasma control, for example, on the radiation level, it may only be possible to place sensors in ports with an adequate level of cooling available, which leads to a significant reduction in spatial coverage (e.g., a vertical and horizontal fan of lines of sight). This is also likely to be true for other tomography diagnostics, such as neutron and gamma-ray cameras. Tomography-like techniques will still be required for one- or two-camera views, for example, Abel inversion (Sec. IV.I.1) or the determination of rotation and ion-temperature profiles from spatially and spectrally resolved X-ray crystal spectrometer measurements (as discussed in Sec. IV.I.4). Compact 2-D sensors viewing tangentially may have an advantage in a BPX environment. The justification for a comprehensive tomography system on an MFE reactor can also be questioned, as the role of the diagnostic is mainly to advance physics understanding of plasma processes from detailed measurements. Because of these difficulties of function, access, integration, and environment, it may be concluded that the prospects for tomography diagnostics on future MFE reactors are, unfortunately, likely to be reduced compared with present-day MFE experiments. On smaller MFE experiments, however, tomography diagnostics will probably continue to be developed further and play an important role in improving physics understanding of plasma processes.

ACKNOWLEDGMENTS

REFERENCES

1. S. SUCKEWER, E. HINNOV, and J. SCHIVELL, "Rapid Scanning of Spatial Distribution of Spectral Line Intensities in PLT Tokamak," PPPL-1430, Princeton Plasma Physics Laboratory (1978).

2. M. E. FOORD, E. S. MARMAR, and J. L. TERRY, "Multichannel Light Detector System for Visible Continuum Measurements on Alcator C," *Rev. Sci. Instrum.*, **53**, 1407 (1982).

3. K. KADOTA, M. OTSUKA, and J. FUJITA, "Space- and Time-Resolved Study of Impurities by Visible Spectroscopy in the High-Density Regime of JIPP T-II Tokamak Plasma," *Nucl. Fusion*, **20**, 209 (1980).

4. B. R. MYERS and M. A. LEVINE, "Two-Dimensional Spectral Line Emission Reconstruction as a Plasma Diagnostic," *Rev. Sci. Instrum.*, **49**, 610 (1978).

5. A. HOLLAND and G. A. NAVRATIL, "Tomographic Analysis of the Evolution of Plasma Cross Sections," *Rev. Sci. Instrum.*, **57**, 1557 (1986).

6. B. V. KUTEEV et al., "Two-Dimensional Optical Tomography of Impurities in the FT-2 Tokamak," *Europhysics Conference Abstracts: 15th Conf. Controlled Fusion and Plasma Heating*, Dubrovnik, May 16–20, 1988, Vol. 12B, part III, p. 1155, European Physical Society (1988).

7. S. SUGIMOTO and S. GOTO, "Spectroscopic Plasma Tomography with Multiple Photocollector Arrays," *Rev. Sci. Instrum.*, **62**, 2138 (1991).

8. M. A. DUBOIS, D. A. MARTY, and A. POCHELON, "Method of Cartography of $q = 1$ Islands During Sawtooth Activity in Tokamaks," *Nucl. Fusion*, **20**, 1355 (1980).

9. N. R. SAUTHOFF, K. M. McGUIRE, and S. VON GOELER, "Reconstruction of $m = 1$ MHD Modes from Projections," *Rev. Sci. Instrum.*, **57**, 2139 (1986).

10. P. SMEULDERS, "Evolution of the $m = 1$ Tearing Mode During Internal Sawtooth Disruption," *Nucl. Fusion*, **23**, 529 (1983).

11. Y. NAGAYAMA et al., "Soft X-Ray Tomography of the $m = 2$ Magnetic Island Structure in the JIPP T-II Tokamak," *Jpn. J. Appl. Phys.*, **20**, L779 (1981).

12. P. SMEULDERS, "A Fast Plasma Tomography Routine with Second-Order Accuracy and Compensation for Spatial Resolution," IPP 2/252, Max-Planck-Institut für Plasmaphysik (1983).

13. J. F. CAMACHO and R. S. GRANETZ, "Soft X-Ray Tomography Diagnostic for the Alcator C Tokamak," *Rev. Sci. Instrum.*, **57**, 417 (1986).

14. R. S. GRANETZ and P. SMEULDERS, "X-Ray Tomography on JET," *Nucl. Fusion*, **28**, 457 (1988).

15. R. DÉCOSTE, "X-Ray Tomography on Plasmas with Arbitrary Cross Sections and Limited Access," *Rev. Sci. Instrum.*, **56**, 806 (1985).

16. C. JANICKI, R. DÉCOSTE, and P. NOËL, "Soft X-Ray Imaging Diagnostic on the TdeV Tokamak," *Rev. Sci. Instrum.*, **63**, 4410 (1992).

17. R. S. GRANETZ and L. WANG, "Design of the X-Ray Tomography System on Alcator C-MOD," *Proc. Workshop Diagnostics for Contemporary Fusion Experiments*, Varenna, August 27–September 6, 1991, ISPP-9, p. 425, P. E. STOTT et al., Eds., Socièta Italiana di Fisica (1991).

18. D. F. DA CRUZ and A. J. H. DONNÉ, "The Soft X-Ray Diagnostic at the RTP Tokamak," *Rev. Sci. Instrum.*, **65**, 2295 (1994).

19. B. ALPER et al., "The JET Multi-Camera Soft X-Ray Diagnostic," *Europhysics Conference Abstracts: 21st Conf. Controlled Fusion and Plasma Physics*, Montpellier, June 27–July 1, 1994, Vol. 18B, part III, p. 1304, European Physical Society (1994).

20. B. ALPER et al., "The JET Soft X-Ray Diagnostics System," *Rev. Sci. Instrum.*, **68**, 778 (1997).

21. M. BESSENRODT-WEBERPALS et al., "Sawtooth Filtering by Singular Value Decomposition," *Europhysics Conference Abstracts: 21st Conf. Controlled Fusion and Plasma Physics*, Montpellier, June 27–July 1, 1994, Vol. 18B, part III, p. 1312, European Physical Society (1994).

22. M. ANTON, M. J. DUTCH, and H. WEISEN, "Relative Calibration of Photodiodes in the Soft-X-Ray Spectral Range," *Rev. Sci. Instrum.*, **66**, 3762 (1995).

23. M. ANTON et al., "X-Ray Tomography on the TCV Tokamak," *Plasma Phys. Control. Fusion*, **38**, 1849 (1996).

24. A. WELLER, C. GÖRNER, and D. GONDA, "X-Ray Diagnostics on Wendelstein 7-AS," *Rev. Sci. Instrum.*, **70**, 484 (1999).

25. A. WELLER, S. MOHR, and C. JUNGHANS, "Concepts of X-Ray Diagnostics for WENDELSTEIN 7-X," *Rev. Sci. Instrum.*, **75**, 3962 (2004).

26. J. KIM and W. CHOE, "Preliminary Design of the Soft X-Ray Array Tomographic Diagnostic System for Korea Superconducting Tokamak Advanced Research (KSTAR) Plasmas," *Rev. Sci. Insturm.*, **75**, 3974 (2004).

27. A. K. CHATTOPADHYAY, A. ANAND, and C. V. S. RAO, "Tomography for SST-1 Tokamak with Pixel method," *Rev. Sci. Instrum.*, **76**, 063502 (2005).

28. L. L. GORELIK, K. A. RAZUMOVA, and V. V. SINITSYN, "Plasma Energy Losses in the Toroidal Chamber Tokamak TM-2," *Proc. 2nd Int. Conf. Plasma Physics and Controlled Nuclear Fusion Research*, Culham, 1965, Vol. 2, p. 647, IAEA (1966) (in Russian).

29. E. R. MÜLLER, K. BEHRINGER, and H. NIEDERMEYER, "Radiation Losses and Global Energy Balance for Ohmically Heated Discharges in ASDEX," *Nucl. Fusion*, **22**, 1651 (1982).

30. K. F. MAST et al., "Bolometric Diagnostics in JET," *Rev. Sci. Instrum.*, **56**, 969 (1985).

31. J. SCHIVELL, "Performance of the Tokamak Fusion Test Reactor Bolometers," *Rev. Sci. Instrum.*, **56**, 972 (1985).

32. K. F. MAST et al., "Fast Bolometric Diagnostic in the RFX Reversed Field Pinch Experiment," *Rev. Sci. Instrum.*, **63**, 4714 (1992).

33. A. MURARI et al., "Multichord Calibrated Bolometer Array for the RFX Experiment," *Rev. Sci. Instrum.*, **66**, 665 (1995).

34. N. RICHARD et al., "Bolometric Diagnostics in Tokamak de Varennes," *Rev. Sci. Instrum.*, **67**, 2202 (1996).

35. J.-C. VALLET et al., "The New Bolometric Diagnostic on Tore Supra," *Europhysics Conference Abstracts: 24th Conf. Controlled Fu-

sion and Plasma Physics, Berchtesgaden, 9–13 June 1997, Vol. 21A, Part I, pp. 233, European Physical Society (1997).

36. M. A. OCHANDO et al., "Bolometry Systems for the TJ-II Flexible Heliac," *Rev. Sci. Instrum.*, **70**, 384 (1999).

37. A. W. LEONARD et al., "Bolometry for Divertor Characterization and Control," *Proc. Worksop Diagnostics for Experimental Thermonuclear Fusion Reactors*, Varenna, August 28–September 1, 1995, p. 549, P. E. STOTT, G. GORINI, and E. SINDONI, Eds, Plenum Press (1996).

38. J. C. FUCHS et al., "Two Dimensional Reconstruction of the Radiation Power Density in ASDEX Upgrade," *Europhysics Conference Abstracts: 21st Conf. Controlled Fusion and Plasma Physics*, Montpellier, June 27–July 1, 1994, Vol. 18B, part III, p. 1308, European Physical Society (1994).

39. R. REICHLE et al., "Bolometer for ITER," *Proc. Workshop Diagnostics for Experimental Thermonuclear Fusion Reactors*, Varenna, August 28–September 1, 1995, p. 559, P. E. STOTT, G. GORINI, and E. SINDONI, Eds, Plenum Press (1996).

40. J. GOETZ et al., "Power Balance and Scaling of the Radiated Power in the Divertor and Main Plasma of Alcator C-Mod," *J. Nucl. Mater.*, **220–222**, 971 (1995).

41. A. W. LEONARD et al., "2D Tomography with Bolometry in DIII-D," *Rev. Sci. Instrum.*, **66**, 1201 (1995).

42. S. KONOSHIMA et al., "Tomographic Reconstruction of Bolometry for JT-60U Diverted Tokamak Characterization," *Plasma Phys. Control. Fusion*, **43**, 959 (2001).

43. R. A. PITTS et al., "Experimental Investigation of the Effects of Neon Injection in TCV," *J. Nucl. Mater.*, **266–269**, 648 (1999).

44. J. WESSON, *Tokamaks*, 2nd ed., p. 208, Oxford University Press, Oxford (1997).

45. C. F. MAGGI et al., "Modelling of Deuterium Emission in High Density Divertor Plasmas in JET," *J. Nucl. Mater.*, **266–269**, 867 (1999).

46. D. REITER, S. WIESEN, and M. BORN, "Radiation Transfer in Dense Edge Plasmas and Divertors: Experimental and Recent Computational Results," *J. Nucl. Mater.*, **313–316**, 845 (2003).

47. I. H. HUTCHINSON, *Principles of Plasma Diagnostics*, Cambridge University Press, Cambridge, Massachusetts (1987).

48. D. P. SCHISSEL et al., "Measurements and Implications of Zeff Profiles on the DIII-D Tokamak," *Phys. Fluids*, **31**, 3738 (1988).

49. P. FRANZ et al., "Two-Dimensional Time Resolved Measurements of the Electron Temperature in MST," *Rev. Sci. Instrum.*, **77**, 10F318 (2006).

50. F. SCHOLZE, H. RABUS, and G. ULM, "Mean Energy Required to Produce an Electron-Hole Pair in Silicon for Photons of Energies Between 50 and 1500 eV," *J. Appl. Phys.*, **84**, 2926 (1998)

51. K. W. WENZEL and R. R. PETRASSO, "X-Ray Response of Silicon Surface-Barrier Diodes at 8 and 17.5 keV: Evidence that the X-Ray Sensitive Depth is Not Generally the Depletion Depth (Abstract)," *Rev. Sci. Instrum.*, **59**, 1849 (1988).

52. T. CHO et al., "Evidence Against Existing X-Ray-Energy Response Theories for Silicon-Surface-Barrier Semiconductor Detectors," *Phys. Rev. A*, **46**, R3024 (1992).

53. B. ALPER et al., "The JET Soft X-Ray Diagnostic Systems," *Rev. Sci. Instrum.*, **68**, 778 (1997).

54. T. CHO et al., "Effects of Neutrons on Semiconductor X-Ray Detectors Including *n*-Type Joint European Torus and *p*-Type GAMMA 10 Tomography Detectors," *Rev. Sci. Instrum.*, **70**, 577 (1999).

55. P. C. DE VRIES et al., "Analysis of Shaping Effects on Sawteeth in JET," *Europhysics Conference Abstracts: 28th Conf. Controlled Fusion and Plasma Physics*, Madeira, June 18–22, 2001, Vol. 25A, p. 1777, European Physical Society (2001).

56. L. C. INGESSON et al., "Soft X-Ray Tomography During ELMs and Impurity Injection in JET," *Nucl. Fusion*, **38**, 1675 (1998).

57. F. H. SEGUIN, R. D. PETRASSO, and C. K. LI, "Radiation-Hardened X-Ray Imaging for Burning-Plasma Tokamaks," *Rev. Sci. Instrum.*, **68**, 753 (1997).

58. Yu. V. GOTT and M. M. STEPANENKO, "Vacuum Photodiode Detectors for Soft X-Ray ITER Plasma Tomography," *Rev. Sci. Instrum.*, **76**, 073506 (2005).

59. A. MURARI et al., "Signal Processing and General Purpose Data Acquisition System for On-Line Tomographic Measurements," *Rev. Sci. Instrum.*, **68**, 951 (1997).

60. K. BLACKLER and A. W. EDWARDS, "The JET Fast Central Acquisition and Trigger System," *IEEE Trans. Nucl. Sci.*, **41**, 111 (1994).

61. E. VAN DER GOOT, A. W. EDWARDS, and J. HOLM, "Real Time Application of Transputers for Soft X-Ray Tomography in Nuclear Fusion Research," *Proc. 1st Int. Conf. Applications of Transputers*, Liverpool, August 23–25, 1989, p. 306, IOS (1990).

62. J. MLYNAR et al., "Investigation of the Consistency of Magnetic and Soft X-Ray Plasma Position Measurements on TCV by Means of a Rapid Tomographic Inversion Algorithm," *Plasma Phys. Control. Fusion*, **45**, 169 (2003).

63. M. J. MANTSINEN et al., "Localized Bulk Electron Heating with ICRF Mode Conversion in the JET Tokamak," *Nucl. Fusion*, **44**, 33 (2004).

64. B. ALPER et al., "Spontaneous Appearance of $q = 2$ Snakes in JET Optimised Shear Discharges," *Europhysics Conference Abstracts: 26th Conf. Controlled Fusion and Plasma Physics*, Maastricht, June 14–18, 1999, Vol. 23J, p. 173, European Physical Society (1999).

65. M. F. F. NAVE et al., "On the Use of MHD Mode Analysis as a Technique for Determination of *q*-Profiles in JET Plasmas," *Rev. Sci. Instrum.*, **75**, 4274 (2004).

66. International Radiation Detectors, Torrance, California.

67. R. KORDE and L. R. CANFIELD, "Silicon Photodiodes with Stable, Near-Theoretical Quantum Efficiency in the Soft X-Ray Region," *Proc. SPIE*, **1140**, 126 (1989).

68. R. J. MAQUEDA, G.A. WURDEN, and E. A. CRAWFORD, "Wideband 'Silicon Bolometers' on the LSX Field Reversed Configuration Experiment," *Rev. Sci. Instrum.*, **63**, 4717 (1992).

69. Y. WEN and R. V. BRAVENEC, "High-Sensitivity, High-Resolution Measurements of Radiated Power on TEXT-U," *Rev. Sci. Instrum.*, **66**, 549 (1995).

70. R. L. BOIVIN et al., "High Resolution Bolometry on the Alcator C-Mod Tokamak," *Rev. Sci. Instrum.*, **70**, 260 (1999).

71. I. FURNO et al., "Fast Bolometric Measurements on the TCV Tokamak," *Rev. Sci. Instrum.*, **70**, 4552 (1999).

72. V. A. SOUKHANOVSKII et al., "Multilayer Mirror and Foil Filter AXUV Diode Arrays on CDX-U Spherical Torus," *Rev. Sci. Instrum.*, **72**, 737 (2001).

73. A. S. PROKHOROV et al., "Measurements of the Plasma Radiative Loss Profile in the M-11M Tokamak with the Help of a Tangential-View AXUV Photodiode Array," *Plasma Phys. Rep.*, **30**, 136 (2004).

74. D. S. GRAY et al., "Time Resolved Radiated Power During Tokamak Disruptions and Spectral Averaging of AXUV Photodiode Response in DIII-D," *Rev. Sci. Instrum.*, **75**, 376 (2004).

75. D. S. GRAY et al., "Plasma Radiometry with 30 Chord Resolution for Fast Transients in the DIII-D Tokamak," *Rev. Sci. Instrum.*, **75**, 4133 (2004).

76. C. SUZUKI, B. J. PETERSON, and K. IDA, "Measurement of Impurity Emission Profiles in CHS Plasma Using AXUV Photodiode Arrays and VUV Bandpass Filters," *Rev. Sci. Instrum.*, **75**, 4142 (2004).

77. B. J. PETERSON et al., "Bolometer Diagnostics for One- and Two-Dimensional Measurements of Radiated Power on the Large Helical Device," *Plasma Phys. Control. Fusion*, **45**, 1167 (2003).

78. Y. LIU et al., "Plasma Emission Tomographic Reconstruction in the Large Helical Device," *Rev. Sci. Instrum.*, **74**, 2312 (2003).

79. A. W. DEGELING et al., "AXUV Bolometer and Lyman-Alpha Camera Systems on the TCV Tokamak," *Rev. Sci. Instrum.*, **75**, 4139 (2004).

80. Y. LIU et al., "Application of Tomographic Imaging to Photodiode Arrays in LHD," *Rev. Sci. Instrum.*, **77**, 10F501 (2006).

81. R. L. BOIVIN et al., "High Resolution Measurements of Neutral Density and Ionization Rate in the Alcator C-Mod Tokamak," *Rev. Sci. Instrum.*, **72**, 961 (2001).

82. D. STUTMAN et al., "Integrated Impurity Diagnostic Package for Magnetic Fusion Experiments," *Rev. Sci. Instrum.*, **74**, 1982 (2003).

83. P. FRANZ et al., "Compact Soft X-Ray Multichord Camera: Design and Initial Operation," *Rev. Sci. Instrum.*, **74**, 2152 (2003).

84. P. FRANZ et al., "High Resolution Soft X-Ray Tomography in the Madison Symmetric Torus," *Rev. Sci. Instrum.*, **75**, 4013 (2004).

85. G. F. MATTHEWS et al., "Studies in JET Divertors of Varied Geometry. II: Impurity Seeded Plasmas," *Nucl. Fusion*, **39**, 19 (1999).

86. R. KORDE et al., "The Effect of Neutron Irradiation on Silicon Photodiodes," *IEEE Trans. Nucl. Sci.*, **36**, 2169 (1989).

87. R. WUNSTROF et al., "Results on Radiation Hardness of Silicon Detectors up to Neutron Fluences of 10^{15} n/cm^2," *Nucl. Instrum. Methods Phys. Res. A*, **315**, 149 (1992).

88. A. G. ALEKSEYEV et al., "Fast XUV 16 × 16 Array Hybrid Module Plasma Imaging Applications," *Plasma Fusion Res.*, **2**, S1061 (2007).

89. H. HSUAN et al., "Measurement of the Energy Balance in ATC Tokamak," *Nucl. Fusion*, **15**, 657 (1975).

90. TFR GROUP, *Proc. 6th Int. Conf. Plasma Physics and Controlled Nuclear Fusion Research*, Berchtesgaden, 1976, Vol. 1, p. 35, IAEA (1977).

91. L. C. INGESSON et al., "Radiation in Impurity-Seeded Discharges in the JET MkI, MkIIA and MkIIGB Divertors," *J. Nucl. Mater.*, **313–316C**, 1173 (2003).

92. A. HUBER et al., "Upgraded Bolometer System on JET for Improved Radiation Measurements," *Fusion Eng. Des.*, **82**, 1327 (2007).

93. B. J. PETERSON et al., "Imaging Bolometer for a Burning Plasma Experiment," *Europhysics Conference Abstracts: 30th Conf. Controlled Fusion and Plasma Physics*, St. Petersburg, July 7–11, 2003, Vol. 27A, p. P-4.067, European Physical Society (2003).

94. J. SCHIVELL et al., "Bolometer for Measurements on High-Temperature Plasmas," *Rev. Sci. Instrum.*, **53**, 1527 (1982).

95. R. BEHRISCH and W. ECKSTEIN, *Physics of Plasma-Wall Interactions in Controlled Fusion*, pp. 413–438, D.E. PORT and R. BEHRISCH, Eds., Plenum Press, New York (1986).

96. W. ECKSTEIN and J. P. BIERSACK, "Reflection of Low-Energy Hydrogen from Solids," *Appl. Phys. A*, **38**, 123 (1985).

97. E. R. MÜLLER and F. MAST, "A New Metal Resistor Bolometer for Measuring Vacuum Ultraviolet and Soft X Radiation," *J. Appl. Phys.*, **55**, 2635 (1984).

98. K. F. MAST et al., "A Low Noise Highly Integrated Bolometer Array for Absolute Measurement of VUV and Soft X Radiation," *Rev. Sci. Instrum.*, **62**, 744 (1991).

99. G. MILLER, J. C. INGRAHAM, and L. S. SCHRANK, "Improved Bolometry System for Reversed Field Pinch Research," *Rev. Sci. Instrum.*, **59**, 700 (1988).

100. R. REICHLE, M. DI MAIO, and L. C. INGESSON, "Progress of the Reference Design for ITER Bolometers and Development of a High Performance Alternative," *Proc. Workshop Diagnostics for Experimental Thermonuclear Fusion Reactors 2*, Varenna, September 4–12, 1997, p. 389, P.E. STOTT et al., Eds., Plenum Press (1998).

101. R. REICHLE et al., "Radiation Hardness Test of Mica Bolometers for ITER in JMTR," *Europhysics Conference Abstracts: 28th Conf. Controlled Fusion and Plasma Physics*, Madeira, June 18–22, 2001, Vol. 25A, p. 1293, European Physical Society (2001).

102. T. NISHITANI et al., "In-Situ Irradiation Test of Mica Substrate Bolometer at the JMTR Reactor for the ITER Diagnostics," *Fusion Eng. Des.*, **63–64**, 437 (2002).

103. L. GIANNONE et al., "Prototype of a Radiation Hard Resistive Bolometer for ITER," *Plasma Phys. Control. Fusion*, **47**, 2123 (2005).

104. L. GIANNONE, K. MAST, and M. SCHUBERT, "Derivation of Bolometer Equations Relevant to Operation in Fusion Experiments," *Rev. Sci. Instrum.*, **73**, 3205 (2002).

105. M. CECCONELLO et al., "Error Analysis for Thermonuclear Plasma Bolometric Measurements Performed with Widely Used Miniaturized Metal Resistor Detectors," *Meas. Sci. Technol.*, **9**, 579 (1998).

106. A. MURARI et al., "Analysis of the Calibration Methods and Error Propagation for the Sensitivity S and the Cooling Time Constant τ_c of the Gold Metal Foil Bolometers," *Rev. Sci. Instrum.*, **75**, 2692 (2004).

107. K. F. MAST, Personal Communication.

108. A. G. ALEKSEYEV, "Thermal Feedback Bolometer with Infrared Thermal Sensing," *Europhysics Conference Abstracts: 30th Conf. Controlled Fusion and Plasma Physics*, St. Petersburg, July 7–11, 2003, Vol. 27A, p. P-1.70, European Physical Society (2003).

109. M. DI MAIO, R. REICHLE, and R. GIANNELLA, "Design of a Ferroelectric Bolometer," *Proc. 17th IEEE/NPSS Symp. Fusion Engineering*, San Diego, October 6–10, 1997, Vol. 2, p. 775, IEEE (1998).

110. M. DI MAIO, "Design of a Ferroelectric Bolometer," PhD Thesis, Shaker Verlag, Aachen, Germany (2000).

111. R. BITTNER et al., "Radiation-Induced Defects in Antiferroelectric Thin Films," *Fusion Eng. Des.*, **66–68C**, 833 (2003).

112. A. STERNBERG et al., "Antiferroelectric $PbZrO_3$ Thin Films: Structure, Properties and Irradiation Effects," *J. Eur. Ceramic Soc.*, **24**, 1653 (2004).

113. G. A. WURDEN, B. J. PETERSON, and S. SUDO, "Design of an Imaging Bolometer System for the Large Helical Device," *Rev. Sci. Instrum.*, **68**, 766 (1997).

114. B. J. PETERSON, "Infrared Imaging Video Bolometer," *Rev. Sci. Instrum.*, **71**, 3696 (2000).

115. B. J. PETERSON et al., "Calibration and Sensitivity of the Infrared Imaging Video Bolometer," *Rev. Sci. Instrum.*, **74**, 2040 (2003).

116. T. F. R. GROUP, "Impurity Behaviour, Radiation Losses and Wall Effects in the T.F.R. Machine," *J. Nucl. Mater.*, **63**, 47 (1976).

117. H. PARCHAMY et al., "Detailed In-Situ Laser Calibration of the Infrared Imaging Video Bolometer for the JT-60U Tokamak," *Rev. Sci. Instrum.*, **77**, 10E515 (2006).

118. B. J. PETERSON et al., "Analysis of Images of Radiation due to Plasma-Limiter Interaction," *IEEE Trans. Plasma Sci.*, **PS-30**, 52 (2002).

119. G. A. WURDEN and B. J. PETERSON, "Development of Imaging Bolometers for Long-Pulse MFE Experiments," *Rev. Sci. Instrum.*, **70**, 255 (1999).

120. N. ASHIKAWA et al., "Infrared Imaging Bolometry for Long Pulse Discharges on LHD," *J. Plasma Fusion Res. Ser.*, **3**, 436 (2000).

121. B. J. PETERSON et al., "Bolometer Diagnostics for One- and Two-Dimensional Measurements of Radiated Power on the Large Helical Device," *Plasma Phys. Control. Fusion*, **45**, 1167 (2003).

122. B. J. PETERSON et al., "Observation of Divertor and Core Radiation in JT-60U by Means of Bolometric Imaging," *J. Nucl. Mater.*, **363–365**, 412 (2007).

123. B. J. PETERSON et al., "Characteristics of Radiating Collapse at the Density Limit in the Large Helical Device," *Plasma Fusion Res.*, **1**, 45 (2006).

124. N. ASHIKAWA et al., "Measurement of the 2-Dimensional Plasma Radiation Structure During Asymmetric Radiative Collapse by a Tangentially Viewing Infrared Imaging Video Bolometer on LHD," *J. Plasma Fusion Res. Ser.*, **4**, 437 (2001).

125. N. ASHIKAWA et al., "Bolometric Images of the Three Dimensional Structure of Asymmetric Radiative Collapse in LHD," *J. Nucl. Mater.*, **313–316**, 1103 (2003).

126. Y. LIU et al., "Application of Tomographic Imaging to Multi-Pixel Bolometric Measurements," *Plasma Fusion Res.*, **2**, S1124 (2007).

127. A. N. TIKHONOV and V. Y. ARSENIN, *Solutions of Ill-Posed Problems*, Winston, Washington (1977).

128. V. F. TURCHIN, V. P. KOZLOV, and M. S. MALKEVICH, "The Use of Mathematical-Statistics Method in the Solution of Incorrectly Posed Problems," *Sov. Phys. Usp.*, **13**, 681 (1971) [*Usp. Fiz. Nauk.*, **102**, 345 (1970)].

129. O. TRETIAK and C. METZ, "The Exponential Radon Transform," *SIAM J. Appl. Math.*, **39**, 341 (1980).

130. F. NATTERER, *The Mathematics of Computerized Tomography*, Wiley and Teubner, Stuttgart, Germany (1986).

131. S. HELGASON, *The Radon Transform*, Birkhäuser, Boston, Massachusetts (1980).

132. S. R. DEANS, *The Radon Transform and Some of Its Applications*, Wiley, New York (1983).

133. G. T. HERMAN, *Image Reconstruction from Projections*, Academic Press, New York (1980).

134. A. C. KAK and M. SLANEY, *Principles of Computerized Tomographic Imaging*, IEEE Press, New York (1988).

135. M. BERTERO, C. DE MOL, and E.R. PIKE, "Linear Inverse Problems with Discrete Data. I: General Formulation and Singular System Analysis," *Inverse Problems*, **1**, 301 (1985).

136. M. BERTERO, C. DE MOL, and E.R. PIKE, "Linear Inverse Problems with Discrete Data. II: Stability and Regularisation," *Inverse Problems*, **4**, 573 (1988).

137. R. M. LEWITT, "Reconstruction Algorithms: Transform Methods," *Proc. IEEE*, **71**, 390 (1983).

138. P. C. HANSEN, "Numerical Tools for Analysis and Solution of Fredholm Integral Equations of the First Kind," *Inverse Problems*, **8**, 849 (1992).

139. H. H. BARRETT and W. SWINDELL, *Radiological Imaging*, Vol. 2, Academic Press, New York (1981).

140. N. R. SAUTHOFF and S. VON GOELER, "Techniques for the Reconstruction of Two-Dimensional Images from Projections," *IEEE Trans. Plasma Sci.*, **PS-7**, 141 (1979).

141. Y. NAGAYAMA, "Tomography of $m = 1$ Mode Structure in Tokamak Plasma Using Least-Square-Fitting Method and Fourier-Bessel Expansions," *J. Appl. Phys.*, **62**, 2702 (1987).

142. A. P. NAVARRO, M. A. OCHANDO, and A. WELLER, "Equilibrium-Based Iterative Tomography Technique for Soft X-Ray in Stellarators," *IEEE Trans. Plasma Sci.*, **PS-19**, 569 (1991).

143. G. A. COTTRELL, "Maximum Entropy and Plasma Physics," JET-P(90)04, JET Joint Undertaking (1990).

144. K. ERTL et al., "Maximum Entropy Based Reconstruction of Soft X-Ray Emissivity Profiles in W7-AS," *Nucl. Fusion*, **36**, 1477 (1996).

145. T. TAKAMURA, T. TODD, and T. EDLINGTON, "X-Ray Imaging of Electron Cyclotron Heated CLEO Plasma by Tangential Projection," *Plasma Phys. Control. Fusion*, **28**, 1717 (1986).

146. R. DÉCOSTE and P. NOËL, "Image Reconstruction Techniques for Computed Tomography from Sparse Data: X-Ray Imaging on the Varennes Tokamak and Other Applications," *Proc. SPIE*, **661**, 50 (1986).

147. N. IWAMA et al., "An Approach with the Akaike Information Criterion to the Radiation Distribution Reconstruction of Toroidal Plasma," *IEEE Trans. Plasma Sci.*, **PS-15**, 609 (1987).

148. N. IWAMA et al., "Phillips-Tikhomov Regularization of Plasma Image Reconstruction with the Generalized Cross Validation," *Appl. Phys. Lett.*, **54**, 502 (1989).

149. S. ZOLETNIK and S. KÁLVIN, "A Method for Tomography in Arbitrary Expansions," *Rev. Sci. Instrum.*, **64**, 1208 (1993).

150. L. C. INGESSON et al., "Poloidally Asymmetric Emission of Visible Light in RTP," *Europhysics Conference Abstracts: 22nd Conf. Controlled Fusion and Plasma Physics*, Bournemouth, July 3–7, 1995, Vol. 19C, part VI, p. 337, European Physical Society (1995).

151. J. MLYNÁŘ, "Pixels Method Computer Tomography in Polar Coordinates," *Czech. J. Phys.*, **45**, 799 (1995).

152. J. H. WILLIAMSON and D. E. EVANS, "Computerized Tomography for Sparse-Data Plasma Physics Experiments," *IEEE Trans. Plasma Sci.*, **PS-10**, 82 (1982).

153. L. C. INGESSON and V. V. PICKALOV, "An Iterative Projection-Space Reconstruction Algorithm for Tomography Systems with Irregular Coverage," *J. Phys. D: Appl. Phys.*, **29**, 3009 (1996).

154. G. T. A. HUYSMANS et al., "MHD Stability of Optimized Shear Discharges in JET," *Nucl. Fusion*, **39**, 1489 (1999).

155. M. SOKOLL, M. BESSENRODT-WEBERPALS, and ASDEX-UPGRADE TEAM, "Differential Rotational Soft X-Ray Tomography of Coupled MHD Modes," *Europhysics Conference Abstracts: 24th Conf. Controlled Fusion and Plasma Physics*, Berchtesgaden, June 9–13, 1997, Vol. 21A, part IV, p. 1517, European Physical Society (1997).

156. G. MINERBO, "MENT: A Maximum Entropy Algorithm for Reconstructing a Source from Projection Data," *Comput. Graphics Image Proc.*, **10**, 48 (1979).

157. G. N. MINERBO et al., "Three-Dimensional Reconstruction of the X-Ray Emission in Laser Imploded Targets," *Appl. Opt.*, **19**, 1723 (1980).

158. N. G. PREOBRAZHENSKY and V. V. PIKALOV, *Ill-Posed Problems of Plasma Diagnostics*, Nauka, Novosibirsk, Soviet Union (1982) (in Russian).

159. V. V. PIKALOV and N. G. PREOBRAZHENSKY, *Reconstructive Tomography in Gas Dynamics and Plasma Physics*, Nauka, Novosibirsk, Soviet Union (1987) (in Russian).

160. T. S. MELNIKOVA and V. V. PIKALOV, *Plasma Tomography*, Nauka, Novosibirsk, Russia (1995) (in Russian).

161. G. DEMETER, "Tomography Using Neural Networks," *Rev. Sci. Instrum.*, **68**, 1438 (1997).

162. X. F. MA, M. FUKUHARA, and T. TAKEDA, "Neural Network CT Image Reconstruction Method for Small Amount of Projection Data," *Nucl. Instrum. Methods Phys. Res. A*, **449**, 366 (2000).

163. J. RADON, "Über die Bestimmung von Funktionen durch ihre Integralwerte längs gewisser Mannigfaltigkeiten," *Ber. Verh. Saechs. Akad. Wiss. Leipzig, Math.-Phys.*, **69**, 262 (1917).

164. L. C. INGESSON et al., "Projection-Space Methods to Take into Account Finite Beam-Width Effects in Two-Dimensional Tomography Algorithms," *J. Opt. Soc. Am. A.*, **16**, 17 (1999).

165. J. L. PRINCE and A. S. WILLSKY, "Constrained Sinogram Restoration for Limited-Angle Tomography," *Opt. Eng.*, **29**, 535 (1990).

166. L. C. INGESSON and R. REICHLE, "Lines of Sight for ITER Bolometers," JET-R(98)03, JET Joint Undertaking (1998); available on the Internet at http://www.iop.org/Jet/fulltext/JETR98003.pdf.

167. J. HOWARD, "Tomography and Reliable Information," *J. Opt. Soc. Am. A*, **5**, 999 (1988).

168. R. A. NILAND, "Maximum Reliable Information Obtainable by Tomography," *J. Opt. Soc. Am.*, **72**, 1677 (1982).

169. D. G. McCAUGHEY and H. C. ANDREWS, "Degrees of Freedom for Projection Imaging," *IEEE Trans. Acoustics, Speech, and Signal Processing*, **ASSP-25**, 63 (1977).

170. V. PICKALOV et al., "Region-of-Interest Tomography of Fine Structures in Plasmas," *Europhysics Conference Abstracts: Int. Congress on Plasma Physics* and *25th Conf. Controlled Fusion and Plasma Physics*, Praha, June 28–July 3, 1998, Vol. 22C, p. 1570, European Physical Society (1998).

171. E. S. LYADINA et al., "A Space-Time Tomography Algorithm for the Five-Camera Soft X-Ray Diagnostic at RTP," *Europhysics Conference Abstracts: 20th Conf. Controlled Fusion and Plasma Physics*, Lisboa, July 26–30, 1993, Vol. 17C, part III, p. 1151, European Physical Society (1993).

172. A. G. LINDGREN and P. A. RATTEY, "The Inverse Discrete Radon Transform with Applications to Tomographic Imaging Using Projection Data," *Adv. Electronics Electron Phys.*, **56**, 359 (1981).

173. L. C. INGESSON and D. J. WILSON, "Optimization of Apertures and Collimators for Multi-Channel Plasma Diagnostics," *Rev. Sci. Instrum.*, **73**, 2890 (2002).

174. L. C. INGESSON, C. F. MAGGI, and R. REICHLE, "Characterization of Geometrical Detection-System Properties for Two-Dimensional Tomography," *Rev. Sci. Instrum.*, **71**, 1370 (2000).

175. L. C. INGESSON et al., "First Results with the Visible-Light Tomography System on RTP," *Europhysics Conference Abstracts: 20th Conf. Controlled Fusion and Plasma Physics*, Lisboa, July 26–30, 1993, Vol. 17C, part III, p. 1147, European Physical Society (1993).

176. L. C. INGESSON et al., "Projection-Space Methods to Take into Account Finite Beam-Width Effects in Two-Dimensional Tomography Algorithms," JET-R(98)02, JET Joint Undertaking (1998); available on the Internet at http://www.iop.org/Jet/fulltext/JETR98002.pdf.

177. G. L. ZENG et al., "Three-Dimensional Iterative Reconstruction Algorithms with Attenuation and Geometric Point Response Correction," *IEEE Trans. Nucl. Sci.*, **NS-38**, 693 (1991).

178. A. R. FORMICONI, A. PUPI, and A. PASSERI, "Compensation of Spatial System Response in SPECT with Conjugate Gradient Reconstruction Technique," *Phys. Med. Biol.*, **34**, 69 (1989).

179. K. M. HANSON and G. W. WECKSUNG, "Local Basis-Function Approach to Computed Tomography," *Appl. Opt.*, **24**, 4028 (1985).

180. L. C. INGESSON, "The Mathematics of Some Tomography Algorithms Used at JET," JET-R(99)08, JET Joint Undertaking (1999); available on the Internet at http://www.iop.org/Jet/fulltext/JETR99008.pdf.

181. A. M. CORMACK, "Representation of a Function by Its Line Integrals, with Some Radiological Applications," *J. Appl. Phys.*, **34**, 2722 (1963).

182. A. M. CORMACK, "Representation of a Function by Its Line Integrals, with Some Radiological Applications. II," *J. Appl. Phys.*, **35**, 2908 (1964).

183. Y. NAGAYAMA et al., "Image Reconstructions of ECE and X-Ray Signals for High Beta Plasmas on TFTR," *Rev. Sci. Instrum.*, **61**, 3265 (1990).

184. L. WANG and R. S. GRANETZ, "A Simplified Expression for the Radon Transform of Bessel Basis Functions in Tomography," *Rev. Sci. Instrum.*, **62**, 842 (1991).

185. W. G. HAWKINS and H. H. BARRETT, "A Numerically Stable Circular Harmonic Reconstruction Algorithm," *SIAM J. Numer. Anal.*, **23**, 873 (1986).

186. P. FRANZ et al., "Soft X-Ray Tomographic Imaging in the RFX Reversed Field Pinch," *Nucl. Fusion*, **41**, 695 (2001).

187. C. P. TANZI and H. J. DE BLANK, "New Method to Analyze Internal Disruptions with Tomographic Reconstruction," *Phys. Plasmas*, **4**, 696 (1997).

188. Y. NAGAYAMA and A. W. EDWARDS, "Rotational Soft X-Ray Tomography of Noncircular Tokamak Plasmas," *Rev. Sci. Instrum.*, **63**, 4757 (1992).

189. G. FUCHS, Y. MIURA, and M. MORI, "Soft X-Ray Tomography on Tokamaks Using Flux Coordinates," *Plasma Phys. Control. Fusion*, **36**, 307 (1994).

190. M. H. BUONOCORE, W. R. BRODY, and A. MACOVSKI, "A Natural Pixel Decomposition for Two-Dimensional Image Reconstruction," *IEEE Trans. Biomed. Eng.*, **BME-28**, 69 (1981).

191. L. C. INGESSON et al., "Comparison of Basis Functions in Soft X-Ray Tomography and Observation of Poloidal Asymmetries in Impurity Density," *Plasma Phys. Control. Fusion*, **42**, 161 (2000).

192. G. T. GULLBERG and G. L. ZENG, "A Reconstruction Algorithm Using Singular Value Decomposition of a Discrete Representation of the Exponential Radon Transform Using Natural Pixels," *IEEE Trans. Nucl. Sci.*, **NS-41**, 2812 (1994).

193. J. R. BAKER, T. F. BUDINGER, and R. H. HUESMAN, "Generalized Approach to Inverse Problems in Tomography: Image Reconstruction for Spatially Variant Systems Using Natural Pixels," *Crit. Rev. Biomed. Eng.*, **20**, 47 (1992).

194. G. C. FEHMERS, L. P. J. KAMP, and F. W. SLUIJTER, "An Algorithm for Quadratic Optimization with One Quadratic Constraint and Bounds on the Variables," *Inverse Problems*, **14**, 893 (1998).

195. G. H. GOLUB and C. F. VAN LOAN, *Matrix Computations*, 3rd ed., p. 256, Johns Hopkins University Press, Baltimore, Maryland (1996).

196. N. TERASAKI et al., "Linear Algebraic Algorithms for High Speed and Stable Reconstruction of Plasma Image," *Fusion Eng. Des.*, **34–35**, 801 (1997).

197. B. R. FRIEDEN, "Restoring with Maximum Likelihood and Maximum Entropy," *J. Opt. Soc. Am.*, **62**, 511 (1972).

198. S. F. GULL and T. J. NEWTON, "Maximum Entropy Tomography," *Appl. Opt.*, **25**, 156 (1986).

199. J. E. SHORE and R. W. JOHNSON, "Axiomatic Derivation of the Principle of Maximum Entropy and the Principle of Minimum Cross-Entropy," *IEEE Trans. Inf. Theory*, **IT-26**, 26 (1980).

200. A. H. DELENEY and Y. BRESLER, "Globally Convergent Edge-Preserving Regularized Reconstruction: An Application to Limited-Angle Tomography," *IEEE Trans. Im. Proc.*, **IP-7**, 204 (1998).

201. S. TWOMEY, *Introduction to the Mathematics of Inversion in Remote Sensing and Indirect Measurement*, Elsevier, Amsterdam and New York (1977).

202. L. C. INGESSON et al., "Radiation Distribution and Neutral-Particle Loss During Detachment in JET," *Europhysics Conference Abstracts: 26th Conf. Controlled Fusion and Plasma Physics*, Maastricht, June 14–18, 1999, Vol. 23J, p. 257, European Physical Society (1999).

203. J. C. FUCHS et al., "Radiation Distribution and Power Balance in the Asdex Upgrade Lyra Divertor," *Europhysics Conference Abstracts: Int. Congress Plasma Physics* and *25th Conf. Controlled Fusion and Plasma Physics*, Praha, June 28–July 3, 1998, Vol. 22C, p. 1510, European Physical Society (1998).

204. A. KALLENBACH et al., "Scrape-Off Layer Radiation and Heat Load to the ASDEX Upgrade LYRA Divertor," *Nucl. Fusion*, **39**, 901 (1999).

205. J. C. FUCHS et al., "Radiation Distribution and Power Balance in the ASDEX Upgrade LYRA Divertor," *J. Nucl. Mater.*, **290–293**, 525 (2001).

206. L. C. INGESSON et al., "Progress on Common Aspects of the EU-Supplied ITER Diagnostics and Prediction of Diagnostic Performance," *Rev. Sci. Instrum.*, **77**, 10F502-1 (2006).

207. G. F. MATTHEWS et al., "Divertor Energy Distribution in JET H-Modes," *J. Nucl. Mater.*, **290–293**, 668 (2001).

208. G. FUCHS, V. PICKALOV, and N. PREOBRAZHENSKI, "Single Projection Tomography in Plasma Physics," Berichte des Forschungszentrums Jülich Jül-3014, Forschungszentrum Jülich (1995).

209. R. N. BRACEWELL, "Strip Integration in Radio Astronomy," *Aust. J. Phys.*, **9**, 198 (1956).

210. M. E. FENSTERMACHER et al., "A Tangentially Viewing Visible TV System for the DIII-D Divertor," *Rev. Sci. Instrum.*, **68**, 974 (1997).

211. J. GAFERT et al., "Reconstruction of Two-Dimensional Emissivity Distributions in the ASDEX Upgrade LYRA-Divertor from TV-CCD-Data," *Europhysics Conference Abstracts: 26th Conf. on Controlled Fusion and Plasma Physics*, Maastricht, June 14–18, 1999, Vol. 23J, p. 1577, European Physical Society (1999).

212. R. A. PITTS et al., "Divertor Geometry Effects on Detachment in TCV," *J. Nucl. Mater.*, **290–293**, 940 (2001).

213. K. ITAMI et al., "Observation of Detachment in the JET MkIIGB Divertor Using CCD Camera Tomography," *J. Nucl. Mater.*, **290–293**, 633 (2001).

214. D. G. NILSON et al., "A Tangentially Viewing Vacuum Ultraviolet TV System for the DIII-D Divertor," *Rev. Sci. Instrum.*, **70**, 738 (1999).

215. M. E. FENSTERMACHER et al., "The Two-Dimensional Structure of Radiative Divertor Plasmas in the DIII-D Tokamak," *Phys. Plasmas*, **4**, 1761 (1997).

216. G. FUCHS et al., "Tomographic Inversion in Toroidal Geometry Using Flux Coordinates," *Europhysics Conference Abstracts: 26th Conf. Controlled Fusion and Plasma Physics*, Maastricht, June 14–18 1999, Vol. 23J, p. 757, European Physical Society (1999).

217. S. OHDACHI et al., "Magnetic Islands Observed by a Fast-Framing Tangentially Viewing Soft X-Ray Camera on LHD and TEXTOR," *Plasma Sci. Tech.*, **8**, 45 (2006).

218. M. GROTH et al., "Diagnosis of Edge Localized Mode Evolution in DIII-D Using Fast Gated CID and Infrared Cameras," *Rev. Sci. Instrum.*, **74**, 2064 (2003).

219. R. BÜCHSE et al., "The Sawtooth Collapse in Rotating JET Plasmas," *Europhysics Conference Abstracts: 1992 Int. Conf. Plasma Physics*, Innsbruck, June 29–July 3, 1992, Vol. 16C, part I, p. 375, European Physical Society (1992).

220. L. C. INGESSON et al., "Radiation Distribution and Neutral-Particle Loss in High-Density Plasmas in the JET MKIIGB Divertor," *Europhysics Conference Abstracts: 28th Conf. Controlled Fusion and Plasma Physics*, Madeira, June 18–22, 2001, Vol. 25A, p. 1633, European Physical Society (2001).

221. Yu. N. DNESTROVSKIJ, E. S. LYADINA, and P. V. SAVRUKHIN, "Space-Time Tomography Problem for Plasma Diagnostic," IAE-5201/15, Kurchatov Institute (1990).

222. C. NARDONE, "Multichannel Fluctuation Data Analysis by the Singular Value Decomposition Method. Application to MHD Modes in JET," *Plasma Phys. Control. Fusion*, **34**, 1447 (1992).

223. T. DUDOK DE WIT, A.-L. PECQUET, and J.-C. VALLET, "The Biorthogonal Decomposition as a Tool for Studying Fluctuations in Plasmas," *Phys. Plasmas*, **1**, 3288 (1994).

224. T. DUDOK DE WIT, "Enhancement of Multichannel Data in Plasma Physics by Biorthogonal Decomposition," *Plasma Phys. Control. Fusion*, **37**, 117 (1995).

225. E. SALLANDER et al., "Effects of Non-Vanishing Toroidal Current Densities on Stability in the Wendelstein 7-AS Stellarator," *Nucl. Fusion*, **40**, 1499 (2000).

226. J. HOWARD, "Vector Tomography Applications in Plasma Diagnostics," *Plasma Phys. Control. Fusion*, **38**, 489 (1996).

227. G. FUCHS and V. PICKALOV, "Vector and Scalar Tomography on Fusion Plasmas Using Hamiltonian and Variational Methods," *Plasma Phys. Control. Fusion*, **40**, 91 (1998).

228. A. L. BALANDIN and Y. ONO, "Tomographic Determination of Plasma Velocity with the Use of Ion Doppler Spectroscopy," *Eur. Phys. J. D*, **17**, 337 (2001).

229. N. P. EFREMOV, N. P. POLUEKTOV, and V. N. KHARCHENKO, "Tomography of Ion and Atom Velocities in Plasmas," *J. Quant. Spectrosc. Radiat. Transfer*, **53**, 723 (1995).

230. R. S. SHAW, "Plasma-Rotation Determination from Spectral Intensity Measurements," *J. Opt. Soc. Am. A*, **4**, 2254 (1987).

231. R. E. BELL, "An Inversion Technique to Obtain Full Poloidal Velocity Profiles in a Tokamak Plasma," *Rev. Sci. Instrum.*, **68**, 1273 (1997).

232. I. CONDREA et al., "Local Poloidal and Toroidal Plasma Rotation Velocities and Ion Temperature in a Tokamak Plasma Obtained by a Matrix Inversion Method Considering Asymmetries," *Phys. Plasmas*, **7**, 3641 (2000).

233. R. P GOLINGO and U. SHUMLAK, "Spatial Deconvolution Technique to Obtain Velocity Profiles from Chord Integrated Spectra," *Rev. Sci. Instrum.*, **74**, 2332 (2003).

234. A. L. BALANDIN and Y. ONO, "Radial Velocity Profile Reconstruction by Doppler Spectroscopy Measurements," *Eur. Phys. J. D*, **27**, 125 (2003).

235. L. C. INGESSON et al., "Optimization of the Lines of Sight of the ITER X-Ray Crystal Spectrometer Diagnostic," *Rev. Sci. Instrum.*, **75**, 3696 (2004).

236. J. HOWARD, F. GLASS, and C. MICHAEL, "Doppler Spectroscopy and Tomography of Plasmas," *Plasma Fusion Res.*, **2**, S1014 (2007).

237. R. REICHLE et al., "Low Energy Neutral Particle Fluxes in the JET Divertor," *J. Nucl. Mater.*, **241–243**, 456 (1997).

238. L. C. INGESSON et al., "Radiation Distribution and Neutral-Particle Loss in the JET MkI and MkIIA Divertors," *Europhysics Conference Abstracts: 24th Conf. Controlled Fusion and Plasma Physics*, Berchtesgaden, June 9–13, 1997, Vol. 21A, part I, p. 113, European Physical Society (1997).

239. J. MLYNAR et al., "First Results of Minimum Fisher Regularisation as Unfolding Method for JET NE213 Liquid Scintillator Neutron Spectrometry," *Fusion Eng. Des.*, **74**, 781 (2005).

240. G. T. A. HUYSMANS, T. HENDER, and B. ALPER, "Identification of External Kink Modes in JET," *Nucl. Fusion*, **38**, 179 (1998).

241. V. IGOCHINE et al., "Investigation of Complex MHD Activity by a Combined Use of Various Diagnostics," *Nucl. Fusion*, **43**, 1801 (2003).

242. P. FRANZ et al., "Observations of Multiple Magnetic Islands in the Core of a Reversed Field Pinch," *Phys. Rev. Lett.*, **92**, 125001 (2004).

243. W. SUTTROP et al., "ELM-Free Stationary H-Mode Plasmas in the ASDEX Upgrade Tokamak," *Plasma Phys. Control. Fusion*, **45**, 1399 (2003).

244. A. WELLER et al., "Survey of Magnetohydrodynamic Instabilities in the Advanced Stellarator Wendelstein 7-AS," *Phys. Plasmas*, **8**, 931 (2001).

245. A. WELLER et al., "Experiments Close to the Beta-Limit in W7-AS," *Plasma Phys. Control. Fusion*, **45**, A285 (2003).

246. A.W. EDWARDS et al., "Rapid Collapse of a Plasma Sawtooth Oscillation in the JET Tokamak," *Phys. Rev. Lett.*, **57**, 210 (1986).

247. Y. NAGAYAMA et al., "Analysis of Sawtooth Oscillations Using Simultaneous Measurement of Electron Cyclotron Emission Imaging and X-Ray Tomography on TFTR," *Phys. Rev. Lett.*, **67**, 3527 (1991).

248. J. A. WESSON et al., "Transport in the Sawtooth Collapse," *Phys. Rev. Lett.*, **79**, 5018 (1997).

249. A. WELLER et al., "Persistent Density Perturbations at Rational-q Surfaces Following Pellet Injection in the Joint European Torus," *Phys. Rev. Lett.*, **59**, 2303 (1987).

250. R. D. GILL et al., "Snake-Like Density Perturbations in JET," *Nucl. Fusion*, **32**, 723 (1992).

251. H. HUGON et al., "Shear Reversal and MHD Activity During Pellet Enhanced Performance Shots in JET," *Nucl. Fusion*, **32**, 33 (1992).

252. R. D. GILL et al., "Direct Observations of Runaway Electrons During Disruptions in the JET Tokamak," *Nucl. Fusion*, **40**, 163 (2000).

253. H. WEISEN et al., "Measurement of Light Impurity Densities and Z_{eff} in JET Using X-Ray Tomography," *Rev. Sci. Instrum.*, **62**, 1531 (1991).

254. D. PASINI et al., "Impurity Transport in JET Using Laser Injected Impurities in Ohmic and Radiofrequency Heated Plasmas," *Nucl. Fusion*, **30**, 2049 (1990).

255. R. GIANNELLA et al., "Role of Current Profile in Impurity Transport in JET L Mode Discharges," *Nucl. Fusion*, **34**, 1185 (1994).

256. D. PASINI et al., "Measurements of Impurity Transport in JET," *Plasma Phys. Control. Fusion*, **34**, 677 (1992).

257. R. GIANNELLA et al., "Impurity Transport Studies for JET Hot-Ion H Mode and Optimised Shear Discharges," *Europhysics Conference Abstracts: 24th Conf. Controlled Fusion and Plasma Physics*, Berchtesgaden, June 9–13, 1997, Vol. 21A, part I, p. 53, European Physical Society (1997).

258. H. CHEN et al., "Impurity Transport with Strong and Weak Internal Thermal Barriers in JET Optimised Shear Plasmas," *Nucl. Fusion*, **41**, 31 (2001).

259. R. DUX et al., "Impurity Transport in Internal Transport Barrier Discharges on JET," *Nucl. Fusion*, **44**, 260 (2004).

260. P. GALLI et al., "Transient Heat Transport Studies Using Laser Ablated Impurity Injection in JET," *Nucl. Fusion*, **38**, 1355 (1998).

261. P. SMEULDERS, "Tomography of Quasi-Static Deformations of Constant-Emission Surfaces of High-Beta Plasmas in ASDEX," *Nucl. Fusion*, **26**, 267 (1986).

262. R. GIANNELLA et al., "Poloidal Asymmetry of Impurity in Co- and Counter-Injection Experiment at JET," *Europhysics Conference Abstracts: Int. Conf. Plasma Physics*, Innsbruck, June 29–July 3, 1992, Vol. 16C, part I, p. 279, European Physical Society (1992).

263. B. ALPER et al., "Strong Asymmetries in Impurity Distributions of JET Plasmas," *Europhysics Conference Abstracts: 23rd Conf. Controlled Fusion and Plasma Physics*, Kiev, June 24–28, 1996, Vol. 20C, part I, p. 163, European Physical Society (1996).

264. J. A. WESSON, "Poloidal Distribution of Impurities in a Rotating Tokamak Plasma," *Nucl. Fusion*, **37**, 577 (1997).

265. M. ROMANELLI et al., "Investigation of Impurity Equilibrium at JET," *Europhysics Conference Abstracts: 24th Conf. Controlled Fusion and Plasma Physics*, Berchtesgaden, June 9–13, 1997, Vol. 21A, part I, p. 5, European Physical Society (1997).

266. M. C. BORRÁS and R. S. GRANETZ, "Discrepancies Between Soft X-Ray Emissivity Contours and Magnetic Flux Surfaces in Alcator C-Mod," *Plasma Phys. Control. Fusion*, **38**, 289 (1996).

267. D. J. CAMPBELL et al., "Report on the 5th European Fusion Physics Workshop, Sesimbra, Portugal, 10–12 December 1997," *Plasma Phys. Control. Fusion*, **41**, 133 (1999).

268. S. KONOSHIMA et al., "Two-Dimensional Distribution of Divertor Radiation in JT-60U," *J. Nucl. Mater.*, **313–316**, 888 (2003).

269. J. RAPP et al., "ELM Mitigation by Nitrogen Seeding in the JET Gas Box Divertor," *Plasma Phys. Control. Fusion*, **44**, 639 (2002).

270. G. L. JACKSON et al., "Impurity Feedback Control for Enhanced Divertor and Edge Radiation in DIII-D Discharges," *J. Nucl. Mater.*, **241–243**, 618 (1997).

271. M. MARASCHEK et al., "Real-Time Determination of Total Radiated Power by Bolometric Cameras with Statistical Methods," *Rev. Sci. Instrum.*, **69**, 109 (1998).

272. S. SAKURAI et al., "Impurity Behavior in High Performance Radiative Discharges of JT-60U," *J. Nucl. Mater.*, **290–291**, 1002 (2001).

273. O. BARANA et al., "Neural Networks for Real Time Determination of Radiated Power in JET," *Rev. Sci. Instrum.*, **73**, 2038 (2002).

274. A. LOARTE et al., "Plasma Detachment in JET Mark I Divertor Experiments," *Nucl. Fusion*, **38**, 331 (1998).

275. C. F. MAGGI et al., "The Isotope Effect on the L-Mode Density Limit in JET Hydrogen, Deuterium and Tritium Divertor Plasmas," *Nucl. Fusion*, **39**, 979 (1999).

276. J. A. GOETZ et al., "Comparison of Detached and Radiative Divertor Operation in Alcator C-Mod," *Phys. Plasmas*, **3**, 1908 (1996).

277. A. W. LEONARD et al., "Distributed Divertor Radiation Through Convection in DIII-D," *Phys. Rev. Lett.*, **78**, 4769 (1997).

278. A. W. LEONARD et al., "Radiative Divertor Plasmas with Convection in DIII-D," *Phys. Plasmas*, **5**, 1736 (1998).

279. J. C. FUCHS et al., "Radiation Distribution and Energy Balance During Type-I ELMs in ASDEX Upgrade," *J. Nucl. Mater.*, **337–339**, 756 (2005).

280. V. RICCARDO et al., "Disruption Heat Loads on the JET MkI-IGB Divertor," *Plasma Phys. Control. Fusion*, **44**, 905 (2002).